TECHNISCHE UNIVERSITÄT MÜNCHEN

Fakultät für Luftfahrt, Raumfahrt und Geodäsie

Optimal Trajectory Generation and Robust Flight Control for Helicopters

Omkar Halbe

Vollständiger Abdruck der von der Fakultät für Luftfahrt, Raumfahrt und Geodäsie der Technischen Universität München zur Erlangung des akademischen Grades eines

Doktor-Ingenieurs (Dr.-Ing.)

genehmigten Dissertation.

Vorsitzender:

Prof. Dr.-Ing. Volker Gümmer

Prüfende der Dissertation:

1. Prof. Dr.-Ing. Manfred Hajek
2. Prof. Dr.-Ing. Florian Holzapfel

Die Dissertation wurde am 10.12.2020 bei der Technischen Universität München eingereicht und durch die Fakultät für Luftfahrt, Raumfahrt und Geodäsie am 11.06.2021 angenommen.

This page intentionally left blank.

I dedicate this work to my mother, whose unconditional love and teachings have given me strength and shaped my character.

This page intentionally left blank.

Abstract

Helicopters operating in terrestrial and maritime missions are required to execute complex tactical maneuvers. To enhance performance and mission success, the helicopter must be made agile, robust to uncertainties caused by exogenous factors such as turbulence and endogenous factors such as imperfect modeling information, and must possess automatic trajectory generation and tracking capabilities. However, the complex dynamic responses and the inherent instability in helicopters pose a formidable challenge for control augmentation and autonomous flight guidance.

To fulfil these objectives and overcome the inherent challenges, this thesis first proposes a novel, robust helicopter flight control design suitable for agile and aggressive maneuvers. The control problem is posed as one of robust translational and attitude command tracking with the required closed-loop responses specified to conform to the predicted Level 1 handling qualities (HQ). The required closed-loop axial responses are enforced by an output tracking sliding mode control (SMC) technique by treating axes cross-coupling and exogenous turbulence as matched, bounded uncertainties. To mitigate the chattering effect of SMC, a continuous approximation of the discontinuous control is applied using the boundary layer concept. Any potential actuator saturations, particularly in aggressive maneuvers, are mitigated by reference command adaptation laws using the Pseudo-control Hedging (PCH) technique. The overall closed-loop stability and tracking performance in the presence of the given uncertainties are analyzed.

Next, the thesis proposes a novel online trajectory generation method for tracking waypoints with velocity vector constraints. The translational equations of motion and tracking objectives are decoupled to reduce the dimensions of the numerical problem in terms of the number of simultaneous algebraic equations to be solved. The trajectory generation problem in each axis is formulated as an independent, nonlinear quadratic regulator and solved analytically using the state-dependent Riccati equation technique. The waypoint guidance scheme is then extended to a rendezvous guidance scheme for tracking a constant velocity planar target. For this purpose, the lateral axis engagement kinematics and tracking objectives are formulated as a nonlinear quadratic regulator and solved analytically using the SDRE technique.

The new guidance and control schemes are integrated in a high-fidelity, real-time-capable, representative rotorcraft simulation environment for closed-loop performance evaluation. Several simulation results are presented for autonomous, unpiloted helicopter mission tasks. The first set of simulation results demonstrate that the SMC flight controller is capable of satisfying predicted Level 1 HQ. The results also validate the desired performance in two mission task elements flown autonomously that require moderate to aggressive agility. The SMC technique is then compared with an explicit model-following controller with regard to HQ criteria and the results that ensue are discussed. Thereafter, several autonomous waypoint and rendezvous guidance scenarios illustrate the application of the SDRE-based guidance laws. Furthermore, rendezvous scenarios with a slow maneuvering target show the robustness of the SDRE-based guidance laws. This set of results demonstrates precise waypoint and velocity vector tracking, with smooth and continuous trajectories for the state and control variables. Finally, an autonomous shipboard approach in high-intensity turbulence demonstrates the optimal and online guidance coupled with the robust trajectory tracking for a realistic application within a representative simulation environment.

Acknowledgments

This dissertation marks the fulfillment of the aspirations of a young, curious aerospace engineer. As I look back on the journey of the past five years with a sense of immense satisfaction, I realize that none of it would have seen the light of day without the unflinching support and unrelenting encouragement of family, friends, peers, and seniors.

Prof. Manfred Hajek, not only did you repose confidence in me, but you also offered me numerous opportunities to grow as a researcher and a professional. As my supervisor, you gave me the freedom to explore my interests; yet, your timely advice kept me on track. Your words of wisdom and kindness have always lifted my spirits. I shall remain indebted to you for this opportunity of a lifetime.

Late Prof. Matthias Heller, I shall always cherish your mentorship and guidance. Your affection and kindness have left an indelible imprint on me. I shall truly miss your presence. Prof. Florian Holzapfel, thank you for taking an active interest in my research. Your experience and wisdom gave me new perspectives on how to improve my work and grow as a researcher. Prof. Milan Vrdoljak, you have been a source of great inspiration to me. You initiated me into pilot vehicle system modeling and opened many fascinating vistas that would never have occurred to me. Thank you for being an empathetic mentor.

Martina, your wit and jovial manner always brought me cheer. I cannot thank you enough for your prompt assistance in all matters. Tim Mehling, you have been a dear friend and a tremendous collaborator. Thank you for your teamwork on the flight sim-

ulator; it helped me expand my horizons to handling qualities and human factors. All the Institute colleagues, and especially those that I shared workspace with – Sumeet, Amine, Dominik, Tobi, Willem, Roland, Markus, Stefan, Basti – you schooled me in many fundamental concepts whilst ensuring a warm, conducive, and friendly work environment. To the Institute's alumni, I gratefully acknowledge your efforts in setting up the rotorcraft dynamics and simulation environment; on your shoulders stands the present dissertation.

My supervisors at Airbus Helicopters – Dr. Christian Seidel, Dr. Isabel Del Pozo, Nunzio Sciammetta, Tobias Rumpf, Fabrice Trentin, Tim Waanders – thank you for your support all along this endeavor. I tried my best to honor my professional commitments, yet you have been generous and accommodative on numerous occasions. My good friend Prof. Arnab Maity of IIT Bombay, if it were not for your inspiration during your stint at TUM, I would never have gathered the courage to fulfil my aspiration.

My parents Aai (mom) and Baba (dad), your love and teachings have brought me this far in life. You have made numerous sacrifices and your continuous encouragement has given me the strength to persevere. I owe you my deepest gratitude for all that you have bestowed upon me. Bhagya, my dear sister, you have been my partner in crime through thick and thin. Despite being the elder sibling, I have learnt many life lessons from you that I continue to benefit from to this day. Thank you for your love and care. My wife Ketaki, you have been my pillar of strength. You believed in me and supported me during my long working hours. My love and appreciation for you have only grown stronger with each passing day. Thank you for your immense patience and understanding through this endeavor. Anant and Aadya, you are the best children in the world. You give us great joy and make life worth living.

I owe a great deal of gratitude to my grandparents for instilling moral values and discipline in me, and all my teachers for nurturing my curiosity. To my friends for always bringing cheer and to the forgotten who deserve special mention, I thank you all.

Prior Publications

The following peer-reviewed journal articles are based, in part or in whole, on this dissertation.

[J1] O. Halbe and M. Hajek, “Online Waypoint Trajectory Generation Using State-Dependent Riccati Equation,” *Journal of Guidance, Control, and Dynamics*, vol. 42, no. 12, pp. 2687–2693, 2019. doi: 10.2514/1.G003774

[J2] O. Halbe and M. Hajek, “Robust Helicopter Sliding Mode Control for Enhanced Handling and Trajectory Following,” *Journal of Guidance, Control, and Dynamics*, vol. 43, no. 10, pp. 1805–1821, 2020. doi: 10.2514/1.G005183

[J3] O. Halbe, T. Mehling, M. Hajek, and M. Vrdoljak, “Synthesis and Piloted Evaluation of Advanced Rotorcraft Response-Types Using Robust Sliding Mode Control,” *Journal of the American Helicopter Society*, vol. 66, no. 3, pp. 1-20, 2021. doi: 10.4050/JAHS.66.032008

The following papers in international conference proceedings are based, in part or in whole, on this dissertation.

[C1] T. Mehling, O. Halbe, M. Hajek, and M. Vrdoljak, “Piloted Simulation of Helicopter Shipboard Recovery with Visual and Control Augmentation,” in *AIAA Scitech 2021 Forum (MST Session)*, Virtual Event, January 2021, AIAA Paper 2021-1136. doi: 10.2514/6.2021-1136

[C2] T. Mehling, O. Halbe, M. Vrdoljak, M. Heller, and M. Hajek, "Visual Augmentation for Personal Air Vehicles During Flight Control System," in *Vertical Flight Society 76th Annual Forum*, Virginia Beach, VA, USA, October 2020.

[C3] M. Vrdoljak, T. Mehling, O. Halbe, M. Hajek, and M. Heller, "Analysis of Manual Control for Personal Aerial Vehicle with Flight Control System Degradation," in *5th International Conference on Smart and Sustainable Technologies (SpliTech)*, Split, Croatia, September 2020. doi: 10.23919/SpliTech49282.2020.9243762

[C4] O. Halbe and M. Hajek, "Robust Helicopter Sliding Mode Control for Enhanced Handling and Trajectory Following," in *AIAA Scitech 2020 Forum (GNC Session)*, Orlando, FL, USA, January 2020, AIAA Paper 2020–1828. doi: 10.2514/6.2020-1828

[C5] O. Halbe and M. Hajek, "Online Rendezvous Guidance for Helicopter Using State Dependent Riccati Equation," in *AIAA Scitech 2020 Forum (GNC Session)*, Orlando, FL, USA, January 2020, AIAA Paper 2020–1827. doi: 10.2514/6.2020-1827

[C6] O. Halbe and M. Hajek, "Robust Multivariable Sliding Mode Attitude Control for Enhanced Helicopter Handling Qualities," in *IEEE 58th Conference on Decision and Control*, Nice, France, December 2019, pp. 5868–5872. doi: 10.1109/CDC40024.2019.9030184

[C7] O. Halbe, C. Spieß, and M. Hajek, "Rotorcraft Guidance Laws and Flight Control Design for Automatic Tracking of Constrained Trajectories," in *AIAA Scitech 2018 Forum (GNC Session)*, Kissimmee, Florida, USA, 2018, AIAA Paper 2018–1343. doi: 10.2514/6.2018-1343

[C8] O. Halbe and M. Hajek, "A Methodology towards Rotorcraft Piloting Autonomy for Approach on Moving Offshore Platforms," in *American Helicopter Society 74th Annual Forum*, Phoenix, AZ, USA, 2018.

Contents

List of Figures

This page intentionally left blank.

List of Tables

This page intentionally left blank.

Acronyms

ACAH	Attitude Command, Attitude Hold.
ADS	Aeronautical Design Standard.
CETI	Control Equivalent Turbulence Model.
DOF	Degree of Freedom.
EMF	Explicit Model Following.
GPS	Global Positioning System.
HQ	Handling Qualities.
INDI	Incremental Nonlinear Dynamic Inversion.
INS	Inertial Navigation System.
LQR	Linear Quadratic Regulator.
MPC	Model Predictive Control.
MTE	Mission Task Element.

NDI	Nonlinear Dynamic Inversion.
NED	North-East-Down.
NN	Neural Networks.
PCH	Pseudo-control Hedging.
PID	Proportional-Integral-Derivative.
RCDH	Rate Command, Direction Hold.
RCHH	Rate Command, Height Hold.
RQ	Ride Qualities.
SDC	State Dependent Coefficient.
SDRE	State-Dependent Riccati Equation.
SMC	Sliding Mode Control.
TRC	Translational Rate Command.
UAV	Unmanned Aerial Vehicle.

Nomenclature

Symbols

β	sideslip angle [rad]
$\beta_0, \beta_{1c}, \beta_{1s}$	blade collective, longitudinal and lateral flapping angles [rad]
$\boldsymbol{\nu}, \hat{\boldsymbol{\nu}}$	commanded and estimated pseudo control [−]
$\boldsymbol{\rho}$	sliding mode control gain matrix [−]
$\boldsymbol{\sigma}, \boldsymbol{\mu}$	sliding variables in the inner loop and outer loop, respectively [−]
$\boldsymbol{\theta} \equiv [\phi\ \theta\ \psi]^{\mathrm{T}}$	helicopter Euler angle vector (roll, pitch, and yaw, respectively, with respect to North-East-Down frame) [rad]
$\boldsymbol{\Omega}$	transformation matrix from angular velocities to Euler rates [−]
$\boldsymbol{\omega} = [p\ q\ r]^{\mathrm{T}}$	angular velocity vector (roll, pitch, yaw) in the body-frame [rad/s]
χ	helicopter ground track angle with respect to North [rad]
χ_t	target ground track angle with respect to North [rad]
$\delta\mathbf{D}$	actuator displacements due to turbulence input [%]
Δ	change from trim [−]
ϵ	size of sliding mode boundary layer [−]

η	angle of horizontal line of sight to next waypoint with respect to North [rad]
λ	inverse time period of required first-order dynamic response [/s]
$\mathbf{\Phi}, \mathbf{P}$	sliding mode control design matrices [−]
$\tilde{\mathbf{A}}, \tilde{\mathbf{B}}$	system, control, and output matrices in the augmented state-space model representation of a linear system [−]
$\mathbf{A}, \mathbf{B}, \mathbf{C}$	system, control, and output matrices in the state-space model representation of a linear system [−]
$\mathbf{a} \equiv [a_x\ a_y\ a_z]^{\mathrm{T}}$	helicopter forward, lateral, and vertical accelerations, respectively, in local frame $[\mathrm{m/s^2}]$
$\mathbf{D} = [D_\theta\ D_\alpha\ D_\beta\ D_\delta]^{\mathrm{T}}$	displacement from trim of collective lever, lateral, and longitudinal cyclic stick, and pedals, respectively [%]
$\mathbf{f}, \mathbf{d}$	uncertainties in the linear state space models in the inner loop and outer loop, respectively [−]
$\mathbf{F}$	force vector (excluding gravity) [N]
$\mathbf{J}$	helicopter inertia matrix $[\mathrm{kg\,m^2}]$
$\mathbf{K}_{\mathrm{h}}$	gain for reference command hedging [−]
$\mathbf{M}$	moment vector [N m]
$\mathbf{p} \equiv [x\ y\ z]^{\mathrm{T}}$	helicopter present position in NED frame [m]
$\mathbf{p}_t \equiv [x_t\ y_t\ z_t]^{\mathrm{T}}$	target present position in NED frame [m]
$\mathbf{Q}, \mathbf{R}$	state and control weighting matrices, respectively, in the state-dependent Riccati equation technique [−]

$\mathbf{r}, \mathbf{q}$	command vector in the inner loop and outer loop, respectively [−]
$\mathbf{T}_{\mathrm{be}}$	transformation matrix relating velocity vector from body-fixed frame to North-East-Down frame [−]
$\mathbf{u}, \mathbf{r}$	control vectors in the inner loop and outer loop, respectively [−]
$\mathbf{V} = [V_h \; V_l \; V_z]^T$	forward, lateral, and vertical velocity components, respectively, in local frame [m/s]
$\mathbf{v}_b = [u \; v \; w]^{\mathrm{T}}$	velocity vector in body-frame [m/s]
$\mathbf{x}, \mathbf{z}$	state vectors in the inner loop and outer loop, respectively [−]
$\mathbf{y}, \mathbf{w}$	output vector in the inner loop and outer loop, respectively [−]
ω	natural frequency of required second-order dynamic response [/s]
ζ	damping ratio of required second-order dynamic response [−]
$\zeta_0, \zeta_{1c}, \zeta_{1s}$	blade collective, longitudinal and lateral lead-lagging angles [rad]
d	length of horizontal line of sight to next waypoint [m]
d_z	maximum achievable vertical distance [m]
d_{V_h}, d_{χ}	minimum horizontal distances corresponding to horizontal velocity and ground track constraints, respectively [m]
F_{mr}	main rotor thrust [N]
G	feedback gain in explicit model following controller [−]
g	acceleration due to gravity [m/s^2]
N	static gains in the state weighting matrices [−]
R	turn radius [m]

t	time [s]
t_{go}	time to go to next waypoint [s]
$V_{h,t}$	target ground speed in NED frame [m/s]
W_n	white noise input of zero mean and unity covariance [−]

Subscripts

bw	bandwidth
c	command
e	error
fb	feedback
ff	feedforward
h	hedged
m	model
o	outer loop
t	target

1 Introduction

> "The helicopter is probably the most versatile instrument ever invented by man."
>
> *(Igor Sikorsky, 1889–1972, aviation pioneer and inventor)*

A HELICOPTER represents a complex dynamic system. Unlike fixed-wing aircraft, the motion of helicopters (and rotary-wing aircraft, in general) is characterized and strongly influenced by higher order rotor dynamics. A helicopter's rotor system forms the primary means of generating thrust, propulsive forces, and moments. The dynamics of helicopters are also highly coupled; a single control input produces responses in the rotor dynamics, in the inflow dynamics, and subsequently in all the fuselage degrees of motion. Furthermore, dynamic interactions also exist between the engine, the drive train, and the rotor system. Although the moments and the forces are induced in the rotor system, the fuselage motion is of principal interest for piloting purposes. Indeed, the states of the fuselage are the quantities monitored and controlled by a pilot (or an autopilot) in order to execute the intended flight maneuver. However, the presence of higher-order dynamics, a high number of degrees of freedom, and complex aerodynamic interactions pose a formidable challenge for piloting and controlling the helicopter.

The term “flying qualities” is often used to characterize the dynamic responses of helicopters, nay all aircraft in general. According to Padfield, flying qualities can be categorized into handling qualities, “those that reflect the aircraft’s behavior in response to pilot controls”, and ride qualities, “those that reflect the aircraft’s response to external disturbances” [1]. Cooper and Harper, in their seminal work on the use of pilot ratings, define handling qualities as “those qualities or characteristics of an aircraft that govern the ease and precision with which a pilot is able to perform the tasks required in support of an aircraft role.” [2]. Evidently, an aircraft’s flying qualities are strongly influenced by the type of mission, the phase of flight, and the prevalent environmental conditions. Evidence suggests that external factors such as visibility conditions and turbulence have a detrimental effect on pilot workload [3]. Since helicopters are more often than not flown in low altitudes and in unfavorable environmental conditions, the spare capacity available with the flight crew to perform mission duties depends on the workload that the primary piloting tasks induce. The major design challenges in helicopters are thus, to minimize pilot workload, to automate piloting and guidance tasks, and thereby to maximize both flight safety and mission success.

For quantifying and characterizing flying qualities, the concept of mission task elements (MTE) has been employed in the literature, particularly in the US Army’s handling qualities requirements - Aeronautical Design Standard Performance Specification Handling Qualities Requirements For Military Rotorcraft, ADS-33E-PRF [4]. ADS-33 provides a rational and systematic basis for helicopter handling qualities assessment. Since helicopter operations consist of multiple missions, each mission can be essentially broken down into multiple, contiguous mission task elements (MTEs). Each MTE can then be described by a set of maneuvers that must satisfy temporal and spatial performance requirements [1]. Furthermore, ADS-33 also identifies different kinds of on-axis response characteristics to on-axis step input commands, also known as response-types. The response-types can be in the form of rate command, attitude command, or translational command. The choice of the response-types is guided by the applicable MTE, airspeed regime, external visual conditions and the presence of any visual augmentation systems, as well as pilot preferences [4, 5].

Helicopter flying qualities can be measured and evaluated by both subjective and objective criteria. Objective criteria quantify an aircraft's dynamic responses in the time and frequency domains, and then compare these responses to established numerical references. Subjective criteria enable test pilots to rate the aircraft's dynamic responses using standardized subjective rating techniques. Ratings are assigned in regard to the pilot's ability to fly the given MTEs within the required performance and workload constraints. Accordingly, ADS-33 helps characterize the helicopter's handling qualities at three levels (1,2,3), where Level 1 represents the most desired response characteristics for ease of piloting and Level 3 represents major deficiencies [4]. Whereas the HQ ratings resulting from objective criteria are termed as *predicted HQ levels*, those resulting from subjective criteria are termed as *assigned HQ levels*. In this sense, ADS-33 serves as a useful reference in benchmarking the bare-airframe responses as well as the augmented responses of full-scale helicopters.

In practice, many conventional, bare-airframe, unaugmented helicopters (single main rotor and tail rotor type) do not respond in a manner specified by the HQ requirements, and therefore tend to possess poor HQs. Indeed, most helicopters are not even designed to comply with such handling quality requirements. Some of these helicopters, such as the bearingless BO-105, are inherently unstable in their pitch axis, since they exhibit an unstable phugoid mode. As mentioned earlier, helicopters also exhibit strong interaxis coupling and a melange of primary responses (angular rate, attitude, and translation) in all axes of motion. Moreover, the nature of the responses and the level of coupling are found to vary substantially between hover, low speed, and forward flight regimes. Furthermore, their main and tail rotors possess additional degrees of freedom (DOF), which reduces the bandwidth for controlling the fuselage translational and rotational states. According to Padfield, the overall effective time delay between pilot control input and rotor control demand can be greater than 100 ms and such a delay can halve the response bandwidth capability of an ‘instantaneous’ rotor [1, p.81]. Despite these limitations, helicopters remain the only piloted aerial vehicles in operation that can maneuver equally well in hover, low-speed and forward flight. It is thus natural that helicopters are deployed in demanding tactical and maritime missions including emergency evacuation, aerial reconnaissance, search and rescue, attack, shipboard launch and recovery, among others. For successful mission execution, helicopters must possess excellent maneuvering capabilities, agility, piloting precision, stability in turbulent winds, and the capability to automate piloting tasks. In most cases, these objectives can only be achieved when the helicopter’s natural responses are augmented and its trajectory generation and tracking tasks are automated. The control designer, however, faces several design challenges along this direction; some of these challenges are summarized in the following points:

First, the identification of helicopter system models suitable for the purpose of control design remains a major challenge. The presence of higher-order dynamics leads to a large number of unknown parameters to be idenfitied. High vibrations levels in the vehicle tend to contaminate measurement data that are recorded for the purpose of parameter and system identification. Moreover, the inherent instability of most single main rotor helicopters types itself is a factor that limits the amount of flight test data that can be gathered [6, 7]. These challenges mean that helicopter system and parameter identification is a lengthy and expensive process that requires specialized skills, tools and personnel. Flight control designs must, therefore, aim to reduce their dependence on accurate models.

Second, the flight mechanical parameters that are extracted from flight data by system identification methods are often found to correlate poorly to true flight behavior. Evidence suggests that the correlation of cross-coupling elements is particularly poor [6]. Flight control designs must, therefore, account for the uncertainties in the identified models, as well as any unmodeled dynamics and nonlinearities that the nominal models fail to capture fully and effectively.

Third, the synthesized closed-loop control laws must satisfy the required closed-loop response characteristics and flight stability over the full flight envelope that helicopters operate in, and adequately compensate for all unintended off-axis responses to control and disturbance inputs. Furthermore, any stability and control augmentation system and/or autopilot has to demonstrate compliance with applicable certification specifications. [8] Since the helicopter's natural responses vary with the airspeed regime, this objective is clearly non-trivial.

Fourth, the closed-loop control laws must produce dynamic responses representative of a lower-order system that are more intuitive for pilots to fly than its natural responses of a higher-order [4, 9]. This approach should also ease the integration of advanced navigation and guidance systems. The fulfilment of the specified handling qualities requirements so as to produce deterministic closed-loop dynamic responses satisfying temporal and spatial performances is a key objective along this direction.

Fifth, closed-loop control laws designed to produce dynamic responses directly in the form of the helicopter's inertial motion are more likely to improve success in mission tasks. Such responses types that allow direct control of the helicopter's translational rates are referred to as advanced response-types. Advanced response-types have already shown to markedly alleviate the workload of skilled pilots in demanding maritime missions [10], and even shown a potential to allow low-skilled, amateur pilots to fly conventional full-scale helicopters as personal aerial vehicles [11].

Sixth, aggressive maneuvers may drive the actuators into saturation or undesirable behavior. To mitigate any adverse effects, flight controllers must incorporate the physical characteristics of actuators into the design.

Seventh, to facilitate higher levels of piloting autonomy, it is essential that trajectory generation and tracking in mission tasks be automated and operated in a real-time sense, and coupled directly to the flight controller. Such an architecture will allow flight crew to merely specify waypoints or target location, and then let the system compute and execute an optimized trajectory "on the fly", in what is expected to increase the level of autonomy of rotorcraft [12].

Helicopters have been in operation for well over six decades, and the problems and the requirements described herein are naturally well known. Many published works by subject matter experts have adopted different strategies, and the major approaches will be reviewed in the next chapter. The present thesis aims to address these very problems in helicopter guidance and control, albeit using newer, effective, and previously unexplored control theoretical techniques.

1.1 Thesis Organization

The remainder of the thesis is organized as follows. Chapter 2 reviews the major published works relevant to the current problem and discusses their main benefits and shortcomings. Chapter 3 outlines the key control theoretical concepts - sliding mode control (SMC), state-dependent Riccati equation (SDRE), and pseudo-control hedging (PCH) - that will be used to solve the flight control and guidance problem. Chapter 4 describes the framework for high-fidelity, real-time-capable, and representative rotorcraft simulation environment that will be used to validate the proposed concepts in closed-loop. Chapter 5 applies the SMC and PCH concepts to design robust helicopter attitude and translational command control laws in a two-loop architecture. Chapter 6 applies the SDRE technique to synthesize translational acceleration guidance laws for tracking static waypoints with velocity vector constraints. Chapter 7 extends the SDRE technique for rendezvousing with mobile, planar targets. Chapter 8 presents closed-loop simulation results and discusses the effectiveness of the proposed control and guidance designs. Chapter 9 concludes by summarizing the main ideas of this thesis, along with their benefits and shortcomings. Finally, Chapter 10 envisions some future directions of research.

This page intentionally left blank.

2 State of the Art

To gain a foothold in the area of flight guidance and control in full-scale helicopters, this chapter reviews the existing scientific literature and the state-of-the-art technologies. First, the different control theoretical methods for handling qualities enhancements in conventional helicopters are surveyed. Thereafter, methods for automatic trajectory generation and tracking static waypoints as well as rendezvous with moving waypoints are surveyed.

2.1 Helicopter Control Augmentation

Conventional approaches to full-scale helicopter control design have relied upon classical control techniques such as PID feedback control [13, 14] and explicit model-following control [15, 16]. PID-based schemes require gain scheduling and design iterations to comply with handling quality requirements, and are limited in their performance due to a highly nonlinear, multivariable plant. While model-following approaches showed promise for Level 1 HQs in flight tests, they require accurate knowledge of the system for inverting the commanded states to the blade inputs. Another approach, eigenstructure assignment, affords the advantage of a direct design of feedback gains that satisfy required handling characteristics [5, 17, 18]. However, since it relies on a nominal linear model, robustness in the face of uncertainties and explicit axis decoupling are not guaranteed. An interesting approach for decoupling of the lateral and longitudinal helicopter dynamics was presented using the individual channel design approach, which is a global structural analysis framework [19]. The authors of that study proposed a robust feed-forward controller to overcome cross-couplings and a feedback control to demonstrate Level 1 HQ in the forward flight regime. Some of the limitations of classical methods can be remedied by modern control techniques for helicopter control, such as neural networks (NN) [20], nonlinear dynamic inversion (NDI) [10] and incremental nonlinear dynamic inversion (INDI) [21, 22], model predictive control (MPC) [23, 24], and H_∞ control [25, 26, 27, 28, 29, 30]. While the NN-based approach in Ref. [20] was robust to disturbances, its training requirements and a rather complex control architecture may limit its practical use. NDI is a model-based approach in that it involves feedback linearization of an approximate model. Yet, it was shown to be suitable for higher levels of augmentation in the ship airwakes [10]. INDI partially resolves some drawbacks of NDI by using filtered acceleration measurements in place of the state-dependent terms. As a result, INDI was shown to be more robust to model uncertainties than conventional NDI [21]. Recently, an INDI-based limited authority controller was developed for the Apache AH-64D Longbow helicopter with the aim of overcoming limitations of its existing EMF controller. Piloted simulation testing in hover and low-speed showed improved handling qualities using the INDI technique [22]. The MPC-based approach also showed good performance especially for helicopter in the ship airwakes. However, one needs to account for additional computational costs at implementation stages in MPC-based designs [23, 24]. Other works that addressed flight control in the context of helicopter-shipboard operations include Ref. [31] that examined pilot workload on the basis of pilot models under the influence of turbulent ship airwake. The authors later developed a flight control design [32] to augment gust rejection properties in turbulent ship airwake. Further, several approaches based on modern robust H_∞ design and loop shaping were evaluated in ground-based simulations [30] and in flight [25, 26, 27]. While guaranteed closed-loop stability makes H_∞ an attractive option, the authors of Ref. [26] noted that their H_∞ controller did not adequately compensate for cross-coupling dynamics during piloted evaluations. More recently, Ref. [28] proposed helicopter control design based on H_∞ and μ control for transforming conventional helicopters into personal aerial vehicles that can be operated by untrained pilots. It may be noted that some control design approaches surveyed herein may not be certifiable in accordance with existing certification rules and the associated guidance material [8].

The issue of actuator saturation in helicopter flight control is particularly evident in the design of partial authority flight controllers and during aggressive maneuvers, even though actuators saturation does not appear to show any substantial impact on piloted handling quality assessment [33]. To mitigate any undesirable behavior when actuator operate at their limits, previous approaches have sought to incorporate the actuator limits directly into the control design. In Ref. [34], a limited authority attitude command flight controller was developed and the actuator authority was specified by the value of the attitude at which the series actuator would saturate. Refs. [29, 30] demonstrated application of the H_∞ design technique without driving the actuators into saturation, and the latter was designed as a limited authority system.

At this juncture, it is also worthwhile to visit two extensive, yet non-exhaustive survey papers on full-scale helicopter flight control systems [35, 36]. These surveys evaluated several contemporary and classical helicopter flight control schemes that are based on time domain methods, frequency domain methods, model reference techniques, and output feedback techniques. Ref. [36] also summarized the key features of modern control techniques applied to helicopter flight control. The key theme that is reflected in these surveys is this: ensuring robustness to the exogenous and endogenous uncertainties by classical control techniques requires one to determine appropriately spaced operating points and then to optimize the controller parameters at each such operating point. The number of necessary operating points is often a function of the robustness of the given technique.

Control laws synthesized using robust control techniques offer several design benefits. First, robust control laws can be designed to actively reject/compensate known or unknown uncertainties in the nominal models, which can be particularly advantageous in highly nonlinear, coupled, and poorly identified system models. This benefit assumes significance given the many challenges and pitfalls that may be encountered during helicopter system identification [6]. Second, robust control laws can assure the required closed-loop characteristics over a wider flight envelope without gain scheduling and additional system identification effort. This benefit assumes significance given that pilots assign higher handling quality ratings when the responses are precise, predictable, stable, and representative of an ideal lower-order system [37]. Third, some of the established robust control techniques (especially H_∞ control, INDI control, and sliding mode control) have a wealth of theoretical analyses that can be leveraged for design assurance purposes in the qualification and certification processes.

A promising technique for formulating robust control laws is the sliding mode control (SMC) technique. The underlying idea of SMC is the design of a surface in the system's state space that satisfies the required closed-loop dynamics, and the synthesis of a control law that steers the system's trajectory towards this surface. SMC is particularly well-known for its guaranteed finite-time convergence, accuracy, and insensitivity to a class of uncertainties [38]. For this reason, SMC has found applications in a variety of aerospace control problems, such as missile guidance and control [39], reusable launch vehicle control [40], fighter aircraft control [41], fault-tolerant flight control [42, 43], among others. For helicopter control augmentation, it is conceivable to design a sliding surface conforming to the required closed-loop behavior and then synthesize SMC laws to enforce this behavior. Not only will the closed-loop system satisfy HQ requirements, but it will also ensure performance despite exogenous disturbances, modeling uncertainties and parametric variations. The available literature on full-scale helicopter SMC is, however, limited. In Ref. [44], a model-reference SMC was designed and its robustness to parametric variations and external disturbances were demonstrated on a linear plant model. Refs. [45, 46] both applied model-reference SMC for attitude command control, albeit using higher fidelity nonlinear plants. Both works demonstrated Level 1 HQs in attitude tracking tasks.

To the best knowledge of the author, the literature on full-envelope helicopter translational control using nonlinear control techniques is rather limited [28, 10], and none is available that employs the SMC technique.

2.2 Trajectory Generation and Tracking Control

Currently, the preferred procedure to fly large rotorcraft safely at low altitude is by following a flight path consisting of a sequence of waypoints connected by flight legs. In course-to-fix waypoint navigation, the aircraft's ground track is guided along the straight line joining two waypoints. This method induces an overshoot of the desired flight path at waypoint transitions [47]. Moreover the aircraft is restricted to the vicinity of the geometric path giving little flexibility during path tracking. However, many advanced rotorcraft missions, including new vertical takeoff and landing platforms slated for the future such as unpiloted air taxis and personal aerial vehicles, will require the ability to generate and track feasible trajectories online and in a real-time sense.

Motion planning for aerial vehicles involves multiple objectives, including obstacle avoidance, feasible trajectory generation, and trajectory following. The voluminous literature in this field has been the subject of multiple survey papers [12, 48]. Geometric paths that avoid obstacles are typically generated in the higher rungs of the motion planning hierarchy. In the lower rungs, the paths are parameterized and trajectories are executed while keeping the vehicle within its flight envelope [49, 50]. Most trajectory generation methods attempt to solve a constrained optimal control problem. To achieve real-time capability within acceptable computational costs, configuration space transformations and fast numerical techniques are applied, which render the control solution suboptimal. In [51], the optimization problem is solved on a lower dimensional space with reduced constraints before projecting the solution to a higher dimensional space, yielding a suboptimal solution. In [52], an analytical, suboptimal control solution is obtained from a parameterized optimal trajectory and a linearized vehicle model. In [53, 54], the differential flatness property of quadrotors is exploited for generating polynomial-based smooth, efficient and optimized trajectories. Feasibility of the rotational motion and hard constraints on states and controls can be achieved with explicit 6DOF dynamics in a model predictive control (MPC)-based framework [55, 56]. However, the resulting numerical optimization problem has to be solved iteratively which increases the computational cost. More recent MPC schemes, such as waysets with a variable horizon formulation [57], or sequential linear quadratic solvers [58], have also shown real-time feasibility. Yet, the need for iterative numerical methods still persists. To alleviate computational load in real-time, a library of parameterized paths can be computed and stored offline and used to construct feasible paths online. One such application was demonstrated using motion primitives [59]. Other applications based on geometrical curves, such as clothoids [60], B-splines [61], Bézier curves [62], and four-parameter logistic curves [63], are found to generate smooth, contiguous and feasible flight paths. Depending on the type of curvature, these methods may require extensive pre-computations, iterative solutions, vehicle-specific parametric values, and supplementary translational commands to execute the flight paths. The Dubin's path, which is a relatively fast computation, was used to track waypoints with heading constraints in minimum time [64]. The flight paths were however based on geometric considerations (turn radius) and only valid for constant speed aerial vehicles. It may again be noted that the inherent complexity and computational aspects may hinder formal certification and serial deployment of some of the surveyed techniques [8].

2.3 Rendezvous Guidance

A key feature contributing to enhancing the on-board autonomy is the online generation and tracking of trajectories for rendezvousing with moving targets. In rendezvous guidance, a follower, starting from an arbitrary initial position and velocity vector, is required to intercept a mobile target and attain zero relative velocity with respect to the target at the time of interception. In this sense, rendezvous guidance can be posed as a problem of feasible trajectory generation with terminal constraints on the vehicle's position, velocity, and, if necessary, time.

Rendezvous guidance is an essential component in many aerospace applications and different approaches have been explored to meet this objective. In [65], model predictive control was used to execute a spacecraft docking maneuver, whereas in [66] autonomous spacecraft rendezvous with collision avoidance was demonstrated. A comprehensive review of spacecraft rendezvous and intercept applications was presented in [67]. Many aerial applications, too, necessitate some form of rendezvous guidance. In missile guidance, terminal impact angle constraints were imposed on the missile, and guidance laws using optimal control [68] and sliding mode control [39] were synthesized. In UAV applications, missions involving surveillance, tracking, and loitering by UAVs around ground-based targets were investigated using geometric [69] and Lyapunov-based approaches [70]. Other UAV missions were aimed at rendezvous with cooperative aerial vehicles using sliding mode control [71] and pursuit guidance [72]. Air-to-air refueling is another mission requiring precise rendezvous that was demonstrated using proportional navigation guidance [73] and linear optimal guidance [74].

The approach and landing of helicopters on maritime vessels can also be thought of as a rendezvous guidance problem. An interesting application in Ref. [75] demonstrates automatic deck landing using optical flow theory, which relies on a fundamental parameter used by humans and animals to guide bodily movements. The authors demonstrated automatic shipdeck landing in a manner similar to that achieved by an actual pilot.

Ref. [76] developed a guidance system using relative INS/GPS and flight path control autopilot and reported flight test results of large helicopters operating from small ships. More recently, Ref. [77] presented control laws for autonomous shipdeck recovery for the final approach and landing phases. The inner loop controller was based on dynamic inversion and the outer loop was designed for a constant glideslope approach path and constant relative azimuth to the landing deck. However, this work assumed that the helicopter's airspeed and heading are close to the desired approach conditions.

To simplify mission planning and execution, guidance commands are expected to be generated in a real-time sense. The resulting trajectories must be feasible for the helicopters's physical characteristics and its controller/actuator performances. Additionally, it may be desirable to achieve optimality with respect to certain performance criteria, and to satisfy additional terminal constraints (e.g. final time). An important factor that determines real-time suitability of any guidance scheme is its computational ease. Despite advances in numerical schemes and computing capacities, closed-form analytical solutions for guidance laws remain the natural choice for online execution. Closed-form solutions are readily obtained using classical guidance schemes such as proportional navigation [78, 73] and pursuit guidance [78, 72]. These schemes, however, provide only the lateral acceleration and are not suitable for more complex maneuvers in 3D space. Recent work using a linear optimal control approach also yielded a closed-form solution for an air-to-air refueling scenario [74]. However, since it was based on linearized kinematics, and the follower and the target were closely aligned, its suitability for rendezvous from arbitrary initial positions is not granted.

2.4 Thesis Objectives and Scope

On this background, the main scientific contributions of this thesis can be summarized as follows:

1. The thesis first proposes axial sliding mode control-based attitude and translational control laws that not only enforce the required closed-loop performance corresponding to predicted Level 1 HQ, but also offer stability and robustness to the given uncertainties. Mathematical proofs for the overall closed-loop stability and robustness also form a key contribution of this thesis. It is noted that piloted evaluations using subjective rating techniques of the SMC controller is beyond the scope of this thesis. This thesis also does not address the use of rotor state feedback (flap, lead-lag, torsion) in the closed-loop control design.

2. Next, the thesis proposes an adaptation law for the reference command based on the pseudo-control hedging concept to mitigate actuator saturation in aggressive maneuvers.

3. Thereafter, the thesis proposes a novel state-dependent Riccati equation-based waypoint trajectory generation. The optimality in the SDRE solution lies in the minimization of the state and control deviations over the entire horizon of the trajectory. The SDRE solution yields deterministic, closed-form (and hence real-time capable), and suboptimal guidance laws for the lateral, vertical, and forward accelerations. These accelerations are then directly coupled and tracked by the SMC robust flight controller.

4. Finally, the SDRE-based approach for waypoint guidance is extended to a rendezvous guidance scenario, and 3D helicopter rendezvous with a slower maneuvering target is demonstrated.

This page intentionally left blank.

3 Theoretical Framework

In this chapter, the control theoretical concepts underpinning the helicopter guidance and control laws developed in this thesis are studied. Robustness to modeling and exogenous uncertainties is an important consideration in the development of control laws for enhanced handling qualities. The choice of the sliding mode control technique in the present work is motivated firstly by its desirable robustness properties, and secondly, the fact that sliding mode-based control laws are yet to be synthesized and evaluated for full-scale helicopter translational rate command control.

Likewise, the state-dependent Riccati equation technique offers desirable asymptotic stability and asymptotic optimality properties for multivariable, nonlinear systems. These properties are ideally suited to the nonlinear kinematics that govern the evolution of the helicopter's flight path in 3D space. Moreover, state-dependent Riccati equation-based guidance laws are yet to be synthesized and evaluated for a full-scale helicopter guidance problem.

Following a brief outline of each technique, simple, illustrative examples are presented to enable the reader to develop an intuitive understanding of each technique.

3.1 Sliding Mode Control Technique

3.1.1 Overview

A system's behavior and its operational envelope are often affected by endogenous and exogenous disturbances. Although it may be possible to quantify some of the uncertainties, it is unrealistic to expect a complete and accurate characterization of these uncertainties (else they would no longer be called 'uncertainties'). Despite the presence such uncertainties, the controlled system is required to satisfy its closed-loop performance specifications. To fulfil this objective, the closed-loop control laws must be sufficiently robust to the uncertainties acting upon and affecting the performance the system.

A promising technique that can achieve accurate command (or output) tracking of a class of nonlinear, time-varying systems in the presence of a class of uncertainties is the sliding mode control (SMC) technique [38, 79, 80, 81]. SMC allows the designer to specify a desired, stable *sliding surface* in the form of desired reduced-order dynamics in the system's state space. An appropriate control law is chosen that, firstly, attracts the system states towards this sliding surface, and thereafter, ensures that the system states remain on the sliding surface in the presence of the given disturbances and/or modeling uncertainties. In many instances, such a control law involves a discontinuous function of the specified sliding surface in order to *force* the system states to reach and subsequently remain on the sliding surface. The discontinuous action makes the SMC law nonlinear; indeed, as it will be seen, it is also what makes SMC insensitive to a class of uncertainties. These are uncertainties occurring in the input channels that cannot be characterized, but whose bounds are well known. The essence and properties of SMC will become clearer in the derivations and the illustrative example that follow.

The effect of a discontinuous feedback control law applied to a nonideal system (i.e. system with unmodeled or internal dynamics, actuator dynamics, imperfections due to discrete states, etc.) is that the resulting control signal oscillates at a high, but finite frequency. This is referred to as the *chattering effect.* Needless to say, chattering is undesirable and particularly so in mechanically actuated systems such as the helicopter, as this can lead to serious component fatigue. Fortunately, the literature proposes several means to mitigate the effect of chattering. One such approach is to approximate the discontinuous control law by a continuous control law. The consequence of this approximation is a pseudo-sliding mode control, in which some of the robustness properties of the original sliding mode control are degraded [38, 80]. However, for the helicopter flight control problem considered in this work, it will be shown that it is possible to achieve an acceptable compromise between robustness to uncertainties and practical suitability of the control laws.

3.1.2 Robust Multivariable Sliding Mode Control Synthesis

The flight control design in this work follows the approach of Edwards and Spurgeon [38] for robust output tracking using integral action. Although the helicopter is inherently highly nonlinear, a piecewise linear representation of its true dynamics will be used for the controller synthesis, which is in accordance with both classical and modern control design philosophies discussed in the preceding Sec. 2.1. Nevertheless, the nonlinearities and unmodeled dynamics that are not captured by the linear state-space representation will be regarded as unknown but bounded uncertainties. Consider a linear, multivariable, uncertain system of the form:

$$\dot{\mathbf{x}}(t) = \mathbf{A}\mathbf{x}(t) + \mathbf{B}\mathbf{u}(t) + \mathbf{f}(\mathbf{x}, \mathbf{u}, t) \tag{3.1}$$

$$\mathbf{y}(t) = \mathbf{C}\mathbf{x}(t) \tag{3.2}$$

where $\mathbf{x} \in \mathbb{R}^n$ is the state vector, $\mathbf{u} \in \mathbb{R}^m$ is the control vector, $\mathbf{y} \in \mathbb{R}^p$ is the output vector, $\mathbf{A} \in \mathbb{R}^{n\times n}$ is the system matrix, $\mathbf{B} \in \mathbb{R}^{n\times m}$ is the control matrix, $n \geq m$, and $\mathbf{C} \in \mathbb{R}^{p\times m}$ is the output matrix. The control matrix $\mathbf{B}$ is assumed to have full rank.

$\mathbf{f} : \mathbb{R}^n \times \mathbb{R}^m \times \mathbb{R}^+ \to \mathbb{R}^n$ are unknown but bounded uncertainties (nonlinearities and unmodeled dynamics) appearing in the input channels only. The control objective is for $\mathbf{y}$ to asymptotically track a reference signal $\mathbf{r}(t) \in \mathbb{R}^p$ using the concept of integral action. The output tracking error is defined as $\dot{\mathbf{x}}_e = \mathbf{y} - \mathbf{r}$. For notational simplicity, time dependency of will be dropped in the remaining analysis. The matrices $(\mathbf{A}, \mathbf{B}, \mathbf{C})$ are obtained in a special canonical form, called the regular form, as follows:

$$\mathbf{A} = \begin{bmatrix} \mathbf{A}_{11} & \mathbf{A}_{12} \\ \mathbf{A}_{21} & \mathbf{A}_{22} \end{bmatrix}, \quad \mathbf{B} = \begin{bmatrix} \mathbf{0} \\ \mathbf{B}_2 \end{bmatrix}, \quad \mathbf{C} = \begin{bmatrix} \mathbf{C}_1 & \mathbf{C}_2 \end{bmatrix}, \tag{3.3}$$

This regular form can be readily obtained via QR decomposition, as discussed in Ref. [38, Chapter 4].

In the first step, the state vector is augmented by the error states to the new state vector $\tilde{\mathbf{x}} = [\mathbf{x}_e \; \mathbf{x}]^T$. The system and control matrices of the augmented system are:

$$\tilde{\mathbf{A}} = \begin{bmatrix} \mathbf{0} & \mathbf{C} \\ \mathbf{0} & \mathbf{A} \end{bmatrix} \qquad \tilde{\mathbf{B}} = \begin{bmatrix} \mathbf{0} \\ \mathbf{B} \end{bmatrix}$$

Since $(\mathbf{A}, \mathbf{B})$ are in regular form, $(\tilde{\mathbf{A}}, \tilde{\mathbf{B}})$ are also in regular form.

In the second step, a hyperplane is chosen in the state-space of the augmented system, as shown below:

$$\mathcal{S} = \{\tilde{\mathbf{x}} \in \mathbb{R}^{p+n} : \mathbf{S}\tilde{\mathbf{x}} = \mathbf{0}\} \tag{3.4}$$

where $\boldsymbol{\sigma}(\tilde{\mathbf{x}}) = \mathbf{S}\tilde{\mathbf{x}}$ is the switching function and $\mathbf{S} \in \mathbb{R}^{m\times(p+n)}$ is a design matrix that determines the closed-loop system dynamics when sliding motion is induced. Note that the nominal system is underactuated if $n > m$, and fully actuated if $n = m$, but the augmented system is necessarily underactuated since $(p + n) > m$. Now, the augmented system dynamics can be expressed as:

$$\dot{\tilde{\mathbf{x}}} = \tilde{\mathbf{A}}\tilde{\mathbf{x}} + \tilde{\mathbf{B}}\mathbf{u} - \tilde{\mathbf{T}}\mathbf{r} + \tilde{\mathbf{f}} \tag{3.5}$$

where, $\tilde{\mathbf{T}} = [\mathbf{I}_{p \times p} \; \mathbf{0}_{n \times p}]^{\mathrm{T}}$.

In the third step, a control law is proposed that drives the augmented system in Eqn. (3.5) to the sliding manifold of Eqn. (3.4) in finite time, and sustains sliding motion thereafter. Consider the following control law, which is comprised of a linear component and a discontinuous, nonlinear component:

$$\begin{aligned}
\mathbf{u} &= \mathbf{u}_l + \mathbf{u}_n && (3.6)\\
\text{where} \qquad \mathbf{u}_l &= -(\mathbf{S}\tilde{\mathbf{B}})^{-1}(\mathbf{S}\tilde{\mathbf{A}} - \mathbf{\Phi}\mathbf{S})\tilde{\mathbf{x}} + (\mathbf{S}\tilde{\mathbf{B}})^{-1}\mathbf{S}\tilde{\mathbf{T}}\mathbf{r} && (3.7)\\
\mathbf{u}_n &= -\rho\,(\mathbf{S}\tilde{\mathbf{B}})^{-1}\frac{\mathbf{P}\boldsymbol{\sigma}}{\|\mathbf{P}\boldsymbol{\sigma}\|} && (3.8)
\end{aligned}$$

where, $\mathbf{\Phi} \in \mathbb{R}^{m \times m}$ is a stable design matrix, and $\mathbf{P} \in \mathbb{R}^{m \times m}$, $\mathbf{P} = \mathbf{P}^{\mathrm{T}} > 0$ satisfy the Lyapunov equation $\mathbf{P}\mathbf{\Phi} + \mathbf{\Phi}^{\mathrm{T}}\mathbf{P} = -\mathbf{I}_m$. The linear component in Eqn. (3.7) stabilizes the nominal system and the nonlinear component in Eqn. (3.8) is designed to overcome the uncertainty.

At this point, the scalar $\rho > 0$, which bounds the uncertainty terms, remains to be determined. The existence of sliding motion in finite time also remains to be shown. Suppose sliding motion occurs at $t = t_r$ and is sustained thereafter. Then, $\forall t > t_r$, $\boldsymbol{\sigma} = \dot{\boldsymbol{\sigma}} = 0$. Substituting from Eqn. (3.5)– (3.8) followed by algebraic manipulations yields:

$$\dot{\boldsymbol{\sigma}} = \mathbf{\Phi}\boldsymbol{\sigma} - \rho\,\frac{\mathbf{P}\boldsymbol{\sigma}}{\|\mathbf{P}\boldsymbol{\sigma}\|} + \mathbf{S}\tilde{\mathbf{f}} \tag{3.9}$$

A candidate Lyapunov function is chosen as $V = \boldsymbol{\sigma}^{\mathrm{T}}\mathbf{P}\boldsymbol{\sigma} > 0$, and its time derivative is given by:

$$\dot{V} = \boldsymbol{\sigma}^{\mathrm{T}}(\boldsymbol{\Phi}^{\mathrm{T}}\mathbf{P} + \mathbf{P}\boldsymbol{\Phi})\boldsymbol{\sigma} - 2\rho\|\mathbf{P}\boldsymbol{\sigma}\| + 2\boldsymbol{\sigma}^{\mathrm{T}}\mathbf{PS}\tilde{\mathbf{f}} \tag{3.10}$$

Since $\boldsymbol{\sigma}^{\mathrm{T}}\mathbf{PS}\tilde{\mathbf{f}} \leqslant \|\mathbf{P}\boldsymbol{\sigma}\|\ \|\mathbf{S}\tilde{\mathbf{f}}\|$, Eqn. (3.10) can be expressed as an inequality as follows:

$$\dot{V} \quad \leqslant \quad -\|\boldsymbol{\sigma}\|^2 - 2\|\mathbf{P}\boldsymbol{\sigma}\|(\rho - \|\mathbf{S}\tilde{\mathbf{f}}\|) \leqslant -\|\boldsymbol{\sigma}\|^2 - 2\gamma\|\mathbf{P}\boldsymbol{\sigma}\| \tag{3.11}$$

The last inequality is obtained by setting $\rho \geq \|\mathbf{S}\tilde{\mathbf{f}}\| + \gamma$ for $\gamma > 0$ to guarantee quadratic stability in the presence of bounded uncertainties in the input channels. Finally, the reaching time is given by [38]:

$$t_r \leqslant \frac{1}{\gamma}\sqrt{\frac{V(t=0)}{\min(\mathrm{eig}(\mathbf{P}))}} \tag{3.12}$$

The foregoing discussion reveals two salient features of SMC, namely its insensitivity to bounded uncertainties, and its guaranteed finite reaching time of the specified closed-loop dynamics. Both reasons make the SMC a potent technique for the design of robust control laws in a wide spectrum of physical systems and processes [81]. For the same reasons, the output tracking SMC approach becomes a natural choice for the robust helicopter flight control problem posed in Chapter 5.

Before proceeding to the flight control design, two issues need to be addressed. First, as evident from Eqn. (3.6), the control law includes a high-frequency switching action, which is detrimental to the integrity of the helicopter's mechanical actuators, control links and swashplates. This drawback can be mitigated by the boundary layer concept [38, 42, 40], where the unit vector in Eqn. (3.6) is replaced by a continuous approximation as follows:

$$\mathbf{u} = -(\mathbf{S}\tilde{\mathbf{B}})^{-1}(\mathbf{S}\tilde{\mathbf{A}} - \boldsymbol{\Phi}\mathbf{S})\tilde{\mathbf{x}} + (\mathbf{S}\tilde{\mathbf{B}})^{-1}\mathbf{S}\tilde{\mathbf{T}}\mathbf{r} - \boldsymbol{\rho}(\mathbf{S}\tilde{\mathbf{B}})^{-1}\mathrm{SAT}(\boldsymbol{\xi}/\epsilon) \tag{3.13}$$

where $\boldsymbol{\xi} = \mathbf{P}\boldsymbol{\sigma}$, $\mathrm{SAT}(\boldsymbol{\xi}/\epsilon) = [\mathrm{sat}(\xi_1/\epsilon)\ \ \mathrm{sat}(\xi_2/\epsilon)\ldots\mathrm{sat}(\xi_m/\epsilon)]^{\mathrm{T}}$ and the saturation function is defined as:

$$\mathrm{sat}(\xi_i/\epsilon) = \begin{cases} \mathrm{sgn}(\xi_i/\epsilon) & \text{if } |\xi_i/\epsilon| > 1 \\ \xi_i/\epsilon & \text{if } |\xi_i/\epsilon| \leqslant 1 \end{cases} \tag{3.14}$$

and $\epsilon > 0$ defines the size of the boundary layer, within which the nonlinear component operates as a high gain linear term. Within the boundary layer, ideal sliding motion does not occur and the system is not completely insensitive to the matched uncertainties. The stability of this continuous SMC can be evaluated using the derivative of the Lyapunov function in Eqn. (3.11), which is modified to:

$$\dot{V} \leqslant \begin{cases} -2\|\boldsymbol{\xi}\|(\boldsymbol{\rho} - \|\mathbf{S}\tilde{\mathbf{f}}\|) & \text{if } \|\boldsymbol{\xi}\| > \epsilon \\ -2\|\boldsymbol{\xi}\|(\boldsymbol{\rho}\|\boldsymbol{\xi}\|/\epsilon - \|\mathbf{S}\tilde{\mathbf{f}}\|) & \text{if } \|\boldsymbol{\xi}\| \leqslant \epsilon \end{cases} \tag{3.15}$$

Defining $\boldsymbol{\rho} \geq \|\mathbf{S}\tilde{\mathbf{f}}\| + \gamma$ gives $\dot{V} < 0, \forall \|\boldsymbol{\xi}\| > \epsilon$, and the boundary layer is reached in finite time. The switching function is attracted and thereafter remains uniformly bounded to $\|\boldsymbol{\xi}\| \leqslant \epsilon$. This implies that $\mathbf{x}_e$ also remains bounded to a neighborhood about the origin that depends on ϵ [38]. The actual value of ϵ is often a compromise between robustness to uncertainties and chattering avoidance.

The second issue stems from the fact that insensitivity to uncertainties is only guaranteed after sliding motion has been induced. To reduce the the likelihood of instability during the reaching phase, t_r must be made small, which, however, requires a high value for γ. Consequently, the risk of actuator saturation is high, particularly when the tracking error is large. To remedy this issue, an adaptation law for the reference signal $\mathbf{r}(t)$ is proposed using pseudo-control hedging (PCH), which will be described in the following Sec. 3.3.

3.1.3 Illustrative Example

To fully appreciate the philosophy of sliding mode control, consider an illustrative example of a second-order system from [79]. The motion of many dynamic systems can be approximated to a second order system which is expressed as:

$$\ddot{x} - \Psi \dot{x} = u \tag{3.16}$$

Suppose $\Psi > 0$, then the system defined by Eqn. (3.16) is clearly unstable for any linear control law that uses state feedback of the form $u = kx$ and $u = -kx$, $k > 0$. For the purpose of illustration, let $\Psi = 0.5$ and $k = 2.25$. For these values, the closed-loop eigenvalues are obtained as $\{1.7707, -1.2707\}$ for $k = 2.25$, and $\{0.2500 \pm 1.4790i\}$ for $k = -2.25$. Due to the presence of closed-loop eigenvalues with positive real parts, the system in Eqn. (3.16) is not stabilized by state feedback only. This behavior can be visualized from the phase plots of the system's closed-loop response, as illustrated in Fig. 3.1. It can be noticed that the system trajectories $(x, \dot{x})$ are both not driven to zero if they start from any arbitrary initial values.

Although the second-order system in Eqn. (3.16) can be stabilized using various nonlinear control schemes, the application of the sliding mode control scheme will be illustrated here. It can be noticed that one of the two state-feedback control laws yields one stable closed-loop eigenvalue, namely -1.2707. The system's trajectory moves towards the origin along the eigenvector corresponding to this negative eigenvalue before departing away from the origin along the eigenvector corresponding to the positive eigenvalue. This system behavior can be exploited to develop a switching control scheme that drives the system trajectory toward the stable eigenvalue and subsequently toward the origin.

Let the closed-loop behavior of the system be required to exhibit a stable, first-order behavior as $\dot{x} = -cx$ for some $c > 0$. This is typical of real world systems, whose open-loop behavior may be unstable but whose closed-loop behavior must be stabilized. Moreover,

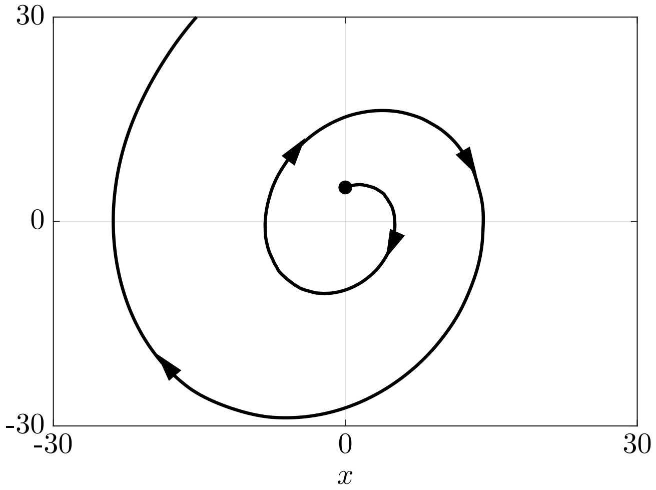

(a) $u = -kx$

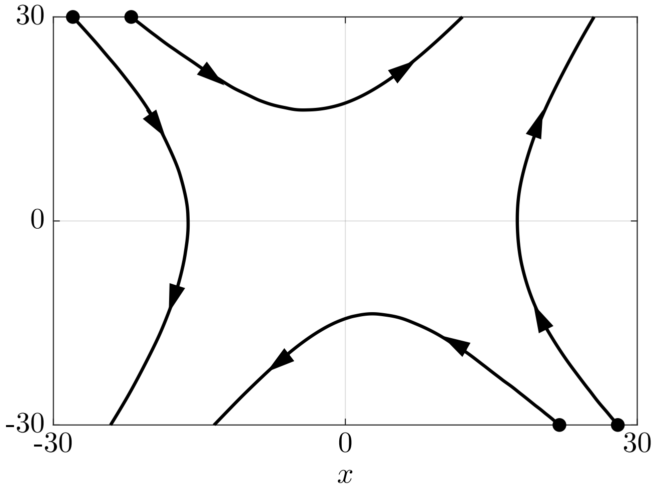

(b) $u = kx$

Figure 3.1: Phase portraits of the second order system, $\ddot{x} - \Psi\dot{x} = u$, using linear feedback control

this example is analogous to the higher-order helicopter system that is required to respond as an ideal lower-order system. For the present example, without loss of generality, let $c = 0.5$. To satisfy this closed-loop behavior, one may synthesize a control law that drives the system trajectory towards $\dot{x} + cx = 0$ and thereafter keeps the system on it.

This behavior can be achieved using a variable structure controller of the form:

$$u = \begin{cases} kx & \ldots \text{if} \quad x(\dot{x} + cx) > 0 \\ -kx & \ldots \text{if} \quad x(\dot{x} + cx) < 0 \end{cases} \tag{3.17}$$

If the control law in Eqn. (3.17) is applied to the system in Eqn. (3.16), then the resulting phase portrait is as shown in Fig. 3.2.

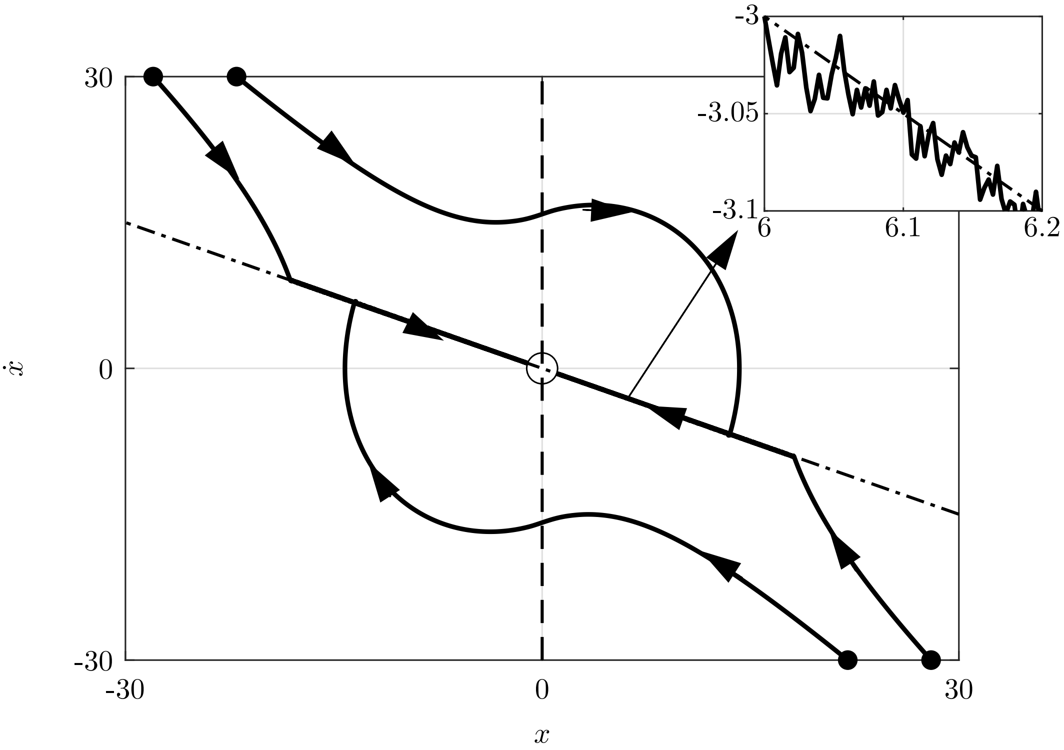

Figure 3.2: Phase portraits of the second order system, $\ddot{x} - \Psi\dot{x} = u$, using sliding mode control, -·-· $\dot{x} + cx = 0$ and - - - $x = 0$

In this illustration, $\sigma = \dot{x} + cx$ is a straight line in the state space of the system in Eqn. (3.16). It represents the desired closed-loop behavior of the system under consideration and is defined as the *sliding variable*. It can be noticed in Fig. 3.2 that the system states, despite starting from any arbitrary initial values (represented by black solid dots), are first driven to the sliding surface $\sigma = \dot{x} + cx = 0$ and then kept in it thereafter. Once $\sigma = 0$ is reached, the states are asymptotically driven to $x \to 0$ and $\dot{x} \to 0$. The control law in Eqn. (3.17) that drives the system states to the sliding surface in finite time and sustains the sliding motion thereafter is referred to as the *sliding mode control law*. Finally, it can be observed that the system trajectory oscillates at high frequency about the sliding surface, or in other words, slides along the surface $\sigma = 0$.

3.2 State-Dependent Riccati Equation Technique

3.2.1 Overview

In many control applications, the system's states must be regulated so that they return to the prescribed value (or zero) from an arbitrary initial value. In contrast to linear quadratic regulators (LQR) for linear systems, state-dependent Riccati equation (SDRE) is a technique that can be used to design nonlinear regulators. In fact, SDRE involves a direct parameterization to transform the nonlinear system into a linear-like structure [82, 83, 84].

The SDRE approach can be applied to nonlinear, multivariable, control-affine systems that have the general form $\dot{\mathbf{x}} = \mathbf{f}(\mathbf{x}) + \mathbf{g}(\mathbf{x})\mathbf{u}$. For such a system, a linear-like structure with state dependent coefficients (SDC) is first obtained by direct parameterization as $\dot{\mathbf{x}} = \mathbf{A}(\mathbf{x})\mathbf{x} + \mathbf{B}(\mathbf{x})\mathbf{u}$. SDRE seeks to find the nonlinear feedback control solution $\mathbf{u}$ that minimizes the linear quadratic sum of the states and controls, as it will be described in the following derivation. To obtain the control solution, an algebraic Riccati equation must be solved analytically (if possible) or numerically [82]. The advantage of an analytical solution of the algebraic Riccati equation is that a closed-form control law is directly obtained. Such a control law can be readily applied in a real-time sense for flight guidance or control purposes and without incurring significant computational cost. However, in a higher order multivariable system, finding an analytical solution to the algebraic Riccati equation is not possible, and a numerical solution must be sought.

Numerical techniques require finite computational time and resources to arrive at a solution, which reduces the attractiveness for online implementation.

It must be noted that the SDRE control solution of a general multivariable system is suboptimal because, while the Pontryagin's necessary condition for optimality is always satisfied, the costate condition is only satisfied asymptotically at a quadratic rate as the states are driven to the origin [84]. In other words, the SDRE control solution of a general multivariable system becomes optimal when all the states are regulated to zero. The performance of the SDRE controller can be tuned using the control and state weighting matrices to ensure adequate performance cover a large flight envelope. This approach can potentially eliminate the need for gain scheduling or approximations.

The state-dependent Riccati equation (SDRE) technique has been previously applied to several problems in aerospace guidance and control. Bogdanov et al.[85] tested an SDRE-based flight control design for small autonomous helicopters with compensation for model mismatch. Cloutier et al. [86] applied SDRE for accurate control of the position and attitude of a spacecraft to perform constrained maneuvers. Ratnoo et al. [87] solved a missile guidance problem with constraints on the final heading using SDRE. The missile lateral acceleration was commanded to achieve a desired impact angle. The reader is referred to [84], which surveys a wide spectrum of aerospace control applications using SDRE. For the present work, the choice of SDRE is motivated by the nonlinearities in the guidance kinematics and the need to achieve an online, real-time capable, optimal guidance law.

3.2.2 Nonlinear Regulation Using State–dependent Riccati Equation

This section outlines the essential steps in the design of SDRE nonlinear regulators. For the associated mathematical proofs, the interested reader is referred to [82]. Consider the following control–affine nonlinear system:

$$\dot{\mathbf{x}} = \mathbf{f}(\mathbf{x}) + \mathbf{g}(\mathbf{x})\mathbf{u} \tag{3.18}$$

The nonlinear structure of $\mathbf{f}(\mathbf{x})$ can be parameterized to obtain a linear-like structure as follows:

$$\dot{\mathbf{x}} = \mathbf{A}(\mathbf{x})\mathbf{x} + \mathbf{B}(\mathbf{x})\mathbf{u} \tag{3.19}$$

where, $\mathbf{x} \in \mathbb{R}^n$, $\mathbf{u} \in \mathbb{R}^m$. Both $\mathbf{f}(\mathbf{x}) = \mathbf{A}(\mathbf{x})\mathbf{x}$ and $\mathbf{B}(\mathbf{x}) = \mathbf{g}(\mathbf{x})$ are differentiable, and moreover $\mathbf{f}(\mathbf{0}) = \mathbf{0}$ and $\mathbf{g}(\mathbf{x}) \neq \mathbf{0}$. $\mathbf{A}(\mathbf{x})$ and $\mathbf{B}(\mathbf{x})$ are the state–dependent coefficients for the state vector $\mathbf{x}$ and control vector $\mathbf{u}$ respectively. In the multivariable case, an infinite number of parameterizations exist for $\mathbf{f}(\mathbf{x}) = \mathbf{A}(\mathbf{x})\mathbf{x}$ [82]. Now, consider an infinite–horizon nonlinear regulation problem given by:

$$\text{Minimize } J = \frac{1}{2}\int_{t_0}^{\infty} [\mathbf{x}^{\mathbf{T}}\mathbf{Q}(\mathbf{x})\mathbf{x} + \mathbf{u}^{\mathbf{T}}\mathbf{R}(\mathbf{x})\mathbf{u}]\, dt \tag{3.20}$$

where, $\mathbf{Q}(\mathbf{x}) \geq \mathbf{0}$ and $\mathbf{R}(\mathbf{x}) > \mathbf{0}$ for all $\mathbf{x}$. Eqn. (3.20) seeks to minimize the states and control efforts over an infinite time horizon. The parameterization of the nonlinear system in Eqn. (3.19) is controllable if the state–dependent controllability matrix given by:

$$\mathbf{M}(\mathbf{x}) = [\mathbf{B}(\mathbf{x}),\ \mathbf{A}(\mathbf{x})\mathbf{B}(\mathbf{x}),\ \ldots,\ \mathbf{A}^{(n-1)}(\mathbf{x})\mathbf{B}(\mathbf{x})] \tag{3.21}$$

has full rank over the domain of interest. For the optimal control problem in Eqns. (3.19) and (3.20), a state-feedback controller is sought with the following form:

$$\mathbf{u}^* = \mathbf{K}(\mathbf{x})\mathbf{x} \tag{3.22}$$

where the feedback gain that minimizes Eqn.(3.20) is given by [82]:

$$\mathbf{K}(\mathbf{x}) = -\mathbf{R}^{-1}(\mathbf{x})\mathbf{B}^{\mathbf{T}}(\mathbf{x})\mathbf{P}(\mathbf{x})\mathbf{x} \tag{3.23}$$

and where $\mathbf{P}(\mathbf{x})$ is the unique, symmetric, and positive-definite matrix obtained from the solution of the algebraic Riccati equation:

$$\mathbf{A}^{\mathbf{T}}(\mathbf{x})\mathbf{P}(\mathbf{x}) + \mathbf{P}(\mathbf{x})\mathbf{A}(\mathbf{x}) - \mathbf{P}(\mathbf{x})\mathbf{B}(\mathbf{x})\mathbf{R}^{-1}(\mathbf{x})\mathbf{B}^{\mathbf{T}}(\mathbf{x})\mathbf{P}(\mathbf{x}) + \mathbf{Q}(\mathbf{x}) \quad = \quad \mathbf{0} \tag{3.24}$$

Thus, the nonlinear state-feedback control law is obtained as:

$$\mathbf{u}^* \quad = \quad -\mathbf{R}^{-1}(\mathbf{x})\mathbf{B}^{\mathbf{T}}(\mathbf{x})\mathbf{P}(\mathbf{x})\mathbf{x} \tag{3.25}$$

The weighting matrices $\mathbf{Q}(\mathbf{x})$ and $\mathbf{R}(\mathbf{x})$ are design parameters which shape the trajectories of the state vector $\mathbf{x}$ and the control vector $\mathbf{u}$ respectively. A relatively higher value of $\mathbf{Q}$ acts upon the states $\mathbf{x}$ for tighter state regulation, whereas a relatively higher value of $\mathbf{R}$ acts upon the control vector $\mathbf{u}$ for lower control effort. For the scalar case, it can be shown that the control law in Eqn. (3.25) is globally optimal. However, for the multivariable case, the control law in Eqn. (3.25) is suboptimal because the SDRE optimality criterion is asymptotically satisfied as $\mathbf{x} \to \mathbf{0}$ [82].

3.2.3 Illustrative Example

The SDRE technique is best illustrated by a simple example. Consider a scalar system taken from [88] written as:

$$\dot{x} = x - x^3 + u \tag{3.26}$$

where $x \in \mathbb{R}$, $u \in \mathbb{R}$ are the scalar state variable and control variable, respectively. It is required to find the optimal value of $u = u^*$ and the system trajectory $(x(t), u(t))$ that minimizes the following cost function with respect to x and u:

$$J = \int_{t_0}^{\infty} (x^2 + u^2)dt \tag{3.27}$$

subject to the dynamic constraint of Eqn. (3.26). An analytical optimal control solution can be obtained using the necessary conditions for optimality [89], as follows:

$$\frac{\partial H}{\partial u} = 0 \tag{3.28}$$

$$\dot{\lambda} = -\frac{\partial H}{\partial x} \tag{3.29}$$

$$\dot{x} = x - x^3 + u \tag{3.30}$$

where the Hamiltonian H is given by:

$$H = (x^2 + u^2) + \lambda(x - x^3 + u) \tag{3.31}$$

According to [88], the analytical solution of Eqns. (3.28)–(3.30) is obtained as:

$$u^* = -(x - x^3) - x\sqrt{x^4 - 2x^2 + 2} \tag{3.32}$$

Now, the problem in Eqns. (3.26)–(3.27) can be solved by the SDRE technique using the steps described previously [90]. Comparing Eqns. (3.18) and (3.26), $\mathbf{f}(\mathbf{x}) = f(x) = (x - x^3)$ and $\mathbf{g}(\mathbf{x}) = g(x) = 1$. The system can be parameterized to obtain the state-dependent coefficient form as follows:

$$\dot{x} = (1 - x^2)x + u \tag{3.33}$$

so that $\mathbf{A}(\mathbf{x}) = (1 - x^2)$ and $\mathbf{B}(\mathbf{x}) = 1$. Comparing Eqns. (3.20) and (3.27), $Q = 1$, $R = 1$. $\mathbf{P}(\mathbf{x}) = p(x)$ is used since the system is scalar. The Algebraic Riccati Equation (3.24) is obtained as:

$$2(1-x^2)p-p^2+1=0 \tag{3.34}$$

which gives:

$$p=1-x^2\pm\sqrt{x^4-2x^2+2} \tag{3.35}$$

Using the positive-definite solution of Eqn. (3.35), the optimal control solution u^* is obtained according to Eqn.(3.25) as:

$$u^*=-x+x^3-x\sqrt{x^4-2x^2+2} \tag{3.36}$$

which is *identical* to Eqn. (3.32). This shows that SDRE yields the optimal control solution for the scalar case.

Further, in [88, 90], another approach using feedback linearization is considered to compare the optimal solutions. Suppose the control applied to the system in Eqn. (3.26) is $u=x^3-2x$ then the closed loop system becomes:

$$\dot{x}=-x \tag{3.37}$$

which is a globally exponentially stable system. However, it can be noticed that the required control effort for large initial value of $x(t=t_0)$ is the third power of x.

The system trajectory x and control input u is plotted in Figs. 3.3a and 3.3b, respectively. Starting from the same initial condition $x(0)=3$, both SDRE and feedback linearization controllers are successful in stabilizing the system. However, it can be seen that the SDRE solution, which is identical to the analytical optimal solution, requires significantly less control effort as compared to feedback linearization. It is also evident that cost x^2+u^2 is minimized by the SDRE controller.

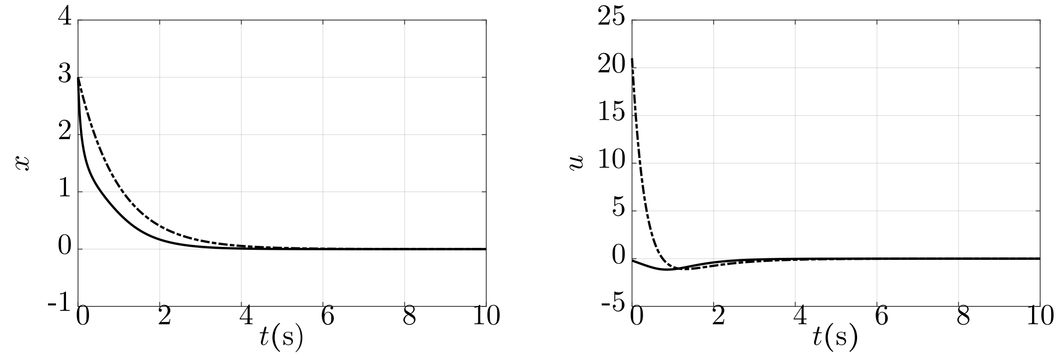

(a) System states

(b) Control effort

Figure 3.3: System trajectories of Eqn. (3.26) for initial condition $x(0) = 3$, ——SDRE optimal control and -·-·Feedback Linearization

3.3 Pseudo-control Hedging

3.3.1 Overview

Pseudo-control Hedging (PCH) aims to protect actuators from being commanded values that they physically cannot achieve, either due to their saturation limits, rate limits or other physical characteristics. Conceptually, PCH moves (hedges) the reference command signal in the opposite direction and in proportion of the amount that the plant did not close the tracking error. PCH was originally proposed by Johnson and Calise in a model-reference adaptive control framework [91], where the adaptive element is prevented from “seeing” the plant or actuator characteristics. Owing to its simplicity and effectiveness, PCH has been applied in several aerospace control applications, including adaptive control for a small-scale autonomous helicopter [92], and incremental NDI control for a full-scale helicopter [21].

3.3.2 Reference Command Adaptation Law

In the present work, an optional PCH layer in each SMC loop adapts the reference signal according to the tracking performance of the dynamics in its lower hierarchy.

This adaptation ensures that when PCH is active, the SMC law is prevented from seeing a very high tracking error $\mathbf{x}_e$, which is typically encountered in aggressive maneuvers, and which may otherwise generate an intractable control signal. To obtain the adaptation law, let the SMC signal $\mathbf{u}$ in Eqn. (3.6) be applied to the original uncertain system in Eqn. (3.1). Substituting Eqn. (3.6) in Eqn. (3.1) yields the commanded pseudo control $\boldsymbol{\nu} = \dot{\mathbf{x}}$, as follows:

$$\boldsymbol{\nu} = \mathbf{A}\mathbf{x} - \mathbf{B}(\mathbf{S}\tilde{\mathbf{B}})^{-1}\Big((\mathbf{S}\tilde{\mathbf{A}} - \boldsymbol{\Phi}\mathbf{S})\tilde{\mathbf{x}} - \mathbf{S}\tilde{\mathbf{T}}\mathbf{r} + \boldsymbol{\rho}\mathrm{SAT}(\mathbf{P}\boldsymbol{\sigma}/\epsilon)\Big) + \mathbf{f} \tag{3.38}$$

Now, suppose $\hat{\mathbf{u}}$ is the actual control achieved by the actuator, which may not be identical to $\mathbf{u}$ due to actuator and plant characteristics. $\hat{\mathbf{u}}$ is either measured from the actual control applied, or it can be estimated by an appropriate actuator model. The estimated pseudo control, $\hat{\boldsymbol{\nu}} = \dot{\hat{\mathbf{x}}}$, corresponding to the actual control is obtained as:

$$\hat{\boldsymbol{\nu}} = \mathbf{A}\mathbf{x} + \mathbf{B}\hat{\mathbf{u}} + \mathbf{f} \tag{3.39}$$

The difference between the commanded and estimated pseudo control, $\boldsymbol{\nu}_h = \boldsymbol{\nu} - \hat{\boldsymbol{\nu}}$ is obtained as:

$$\boldsymbol{\nu}_h = -\mathbf{B}(\mathbf{S}\tilde{\mathbf{B}})^{-1}\Big((\mathbf{S}\tilde{\mathbf{A}} - \boldsymbol{\Phi}\mathbf{S})\tilde{\mathbf{x}} + \mathbf{S}\tilde{\mathbf{T}}\mathbf{r} - \boldsymbol{\rho}\mathrm{SAT}(\mathbf{P}\boldsymbol{\sigma}/\epsilon)\Big) - \mathbf{B}\hat{\mathbf{u}} \tag{3.40}$$

$\boldsymbol{\nu}_h$ is then inserted in the reference model which adapts the reference signal $\mathbf{r}$ as follows:

$$\dot{\mathbf{r}}_h = \mathbf{K}_\mathrm{h}(\mathbf{r} - \mathbf{r}_h) - \boldsymbol{\nu}_h \tag{3.41}$$

The gain matrix $\mathbf{K}_\mathrm{h}$ can be tuned for the required adaptation performance. In accordance with Eqn. (3.41), the actual reference signal applied to the SMC is $\mathbf{r}_h$, which moderates the tracking error $\mathbf{x}_e = \mathbf{y} - \mathbf{r}_h$ when it becomes large and intractable. However, when the commanded control becomes identical to the achieved control, then Eqn. (3.41) simply acts as a first order filter model to the SMC. Nevertheless, it is evident that PCH introduces additional closed-loop dynamics that affect the helicopter's agility in reference command following tasks, as it will be shown in the simulation results.

3.3.3 Illustrative Example

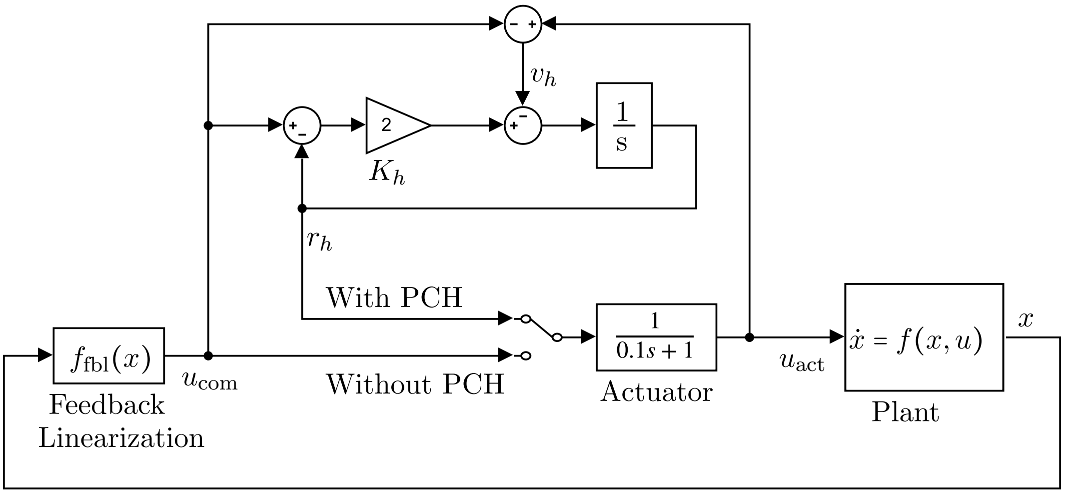

Figure 3.4: Closed-loop control with and without PCH

To illustrate how reference command adaptation is applied to practical systems, consider the same scalar example as Eqn. (3.26) in the previous section [88]. The difference in this example is that a first-order actuator model is considered. The system dynamics are written as follows:

$$\dot{x} = x - x^3 + u_{\text{com}} \tag{3.42}$$

where u_{com} is the commanded control to the actuator. The actuator dynamics are represented by a simple first-order transfer function as:

$$\frac{u_{\text{act}}}{u_{\text{com}}} = \frac{1}{\tau s + 1} \tag{3.43}$$

where τ is the actuator time constant and u_{act} is the actuator output that is applied to the plant. Let a feedback linearization control command of the form $u = x^3 - 2x$ be applied to the actuator[88, 90]. Now, due to the presence of actuator dynamics, the commanded control signal is not identical to the actual control signal. This is illustrated in Fig. 3.4.

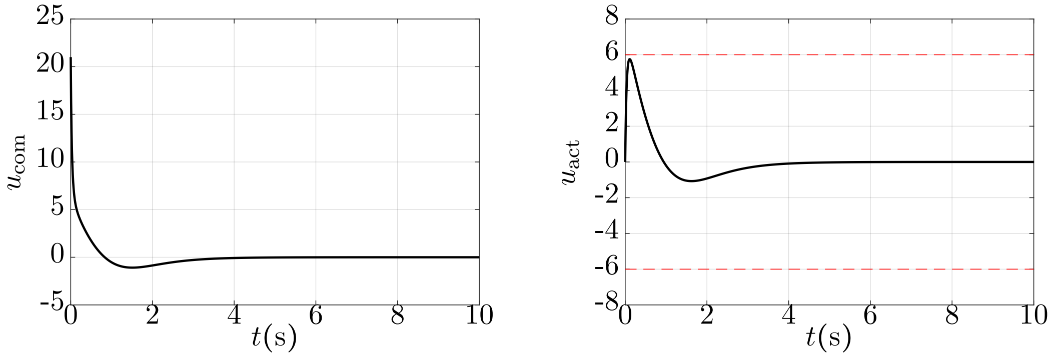

(a) Commanded control

(b) Actuator output

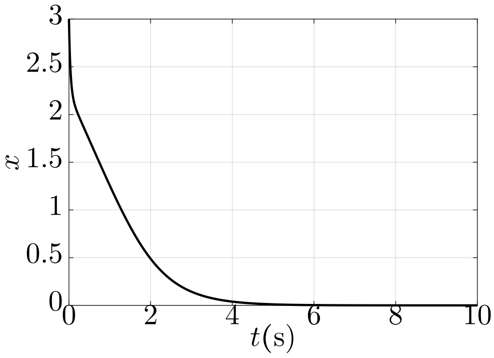

(c) State variable

Figure 3.5: Illustration of actuator saturation without PCH

The control and state variables with the feedback linearized control and without the PCH reference command are depicted in Fig. 3.5. The commanded control as seen in Fig. 3.5a is high. The actuator attempts to track this commanded control as seen in Fig. 3.5b, but fails to match the commanded values. Moreover, the output of the actuator reaches very close to its upper bound (defined arbitrarily for illustration purposes). The system state in Fig. 3.5c is, however, found to be regulated to zero, as expected.

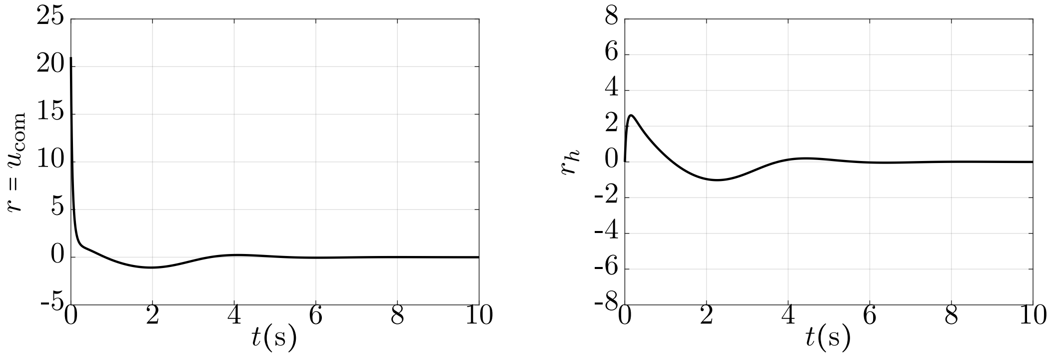

(a) Commanded control

(b) Hedged control command

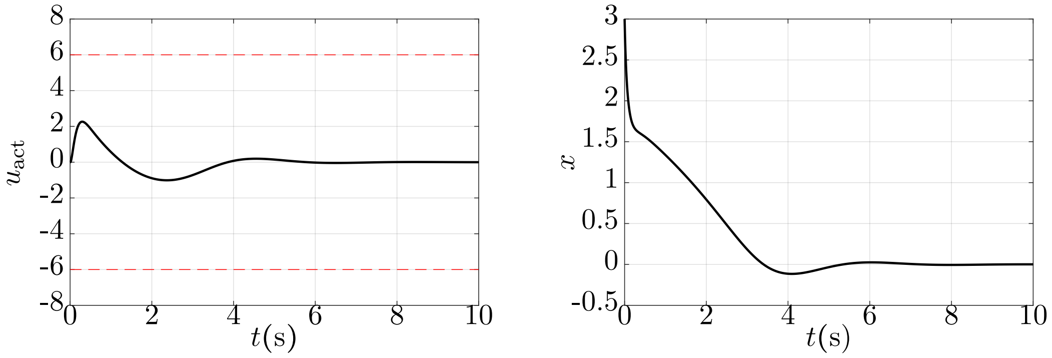

(c) Actuator output

(d) State variable

Figure 3.6: Illustration of the mitigation of actuator saturation with PCH

Next, the PCH reference command adaptation adaptation is activated and the responses are plotted in Fig. 3.6. In this case, the command applied to the actuator is the hedged command r_h, which considers the commanded and actual control and hedges (or adapts) the reference command u_{com} by an amount proportional to the difference between the actual and commanded control. The result of this adaptation can be observed in Figs. 3.6b–3.6c. The actuator output matches the reference command r_h more closely than before. Furthermore, the actuator outputs are far from the saturation limits. The state variable in Fig. 3.6d is regulated to zero, albeit with delays due to the additional closed-loop dynamics introduced by the PCH layer.

4 Modeling and Simulation Framework

This chapter describes the modeling and simulation environment that will be used for validating the new guidance and control formulations. The simulation environment includes a comprehensive, full-scale, nonlinear flight mechanics code representing the helicopter plant and an empirically derived turbulence model. The eigenspace of the helicopter plant is analyzed with regard to its open loop stability characteristics. The simulation models are hosted in a real-time Matlab/Simulink environment and integrated in the rotorcraft simulation environment located in the premises of the Institute of Helicopter Technology.

4.1 Helicopter Simulation Model

A conventional helicopter model of constant mass m and inertia $\mathbf{J}$ is considered. Throughout the thesis, the term conventional helicopter refers to the single main rotor and tail rotor helicopter configuration. The 6-DOF nonlinear rigid body equations of motion of the fuselage are expressed in a vehicle-carried reference frame as:

$$\begin{aligned}
\dot{\mathbf{v}}_{\mathbf{b}} &= \frac{1}{m}\mathbf{F} + g\begin{bmatrix} -\sin\theta \\ \cos\theta\sin\phi \\ \cos\theta\cos\phi \end{bmatrix} - \boldsymbol{\omega}\times\mathbf{v}_{\mathbf{b}} && (4.1) \\
\dot{\boldsymbol{\omega}} &= \mathbf{J}^{-1}(\mathbf{M} - \boldsymbol{\omega}\times\mathbf{J}\boldsymbol{\omega}) && (4.2)
\end{aligned}$$

The forces and moments are contributed by the principal structural components - main rotor, tail rotor, fuselage, vertical fin and horizontal stabilizer. The main and tail rotor blades are assumed to be rigid. Rotor DOF up to the first harmonics of the flap $(\beta_0, \beta_{1c}, \beta_{1s})$, lag $(\zeta_0, \zeta_{1c}, \zeta_{1s})$, and torsion modes are modeled by the blade element theory and analytical downwash models. The Euler attitudes and velocity vector are expressed using an inertial North-East-Down (NED) reference frame as:

$$\dot{\boldsymbol{\theta}} = \boldsymbol{\Omega}\boldsymbol{\omega} \tag{4.3}$$

$$\dot{\mathbf{V}} = \frac{1}{m}\mathbf{T}_{\text{be}}\mathbf{F} + \begin{bmatrix} 0 \\ 0 \\ g \end{bmatrix} \tag{4.4}$$

where $\boldsymbol{\Omega} = \begin{bmatrix} 1 & \mathrm{s}_\phi \mathrm{t}_\theta & \mathrm{c}_\phi \mathrm{t}_\theta \\ 0 & \mathrm{c}_\phi & -\mathrm{s}_\phi \\ 0 & \mathrm{s}_\phi/\mathrm{c}_\theta & \mathrm{c}_\phi/\mathrm{c}_\theta \end{bmatrix}$ $\quad\mathbf{T}_{\text{be}} = \begin{bmatrix} \mathrm{c}_\psi \mathrm{c}_\theta & \mathrm{c}_\psi \mathrm{s}_\theta \mathrm{s}_\phi - \mathrm{s}_\psi \mathrm{c}_\phi & \mathrm{c}_\psi \mathrm{s}_\theta \mathrm{c}_\phi + \mathrm{s}_\psi \mathrm{s}_\phi \\ \mathrm{s}_\psi \mathrm{c}_\theta & \mathrm{s}_\psi \mathrm{s}_\theta \mathrm{s}_\phi + \mathrm{c}_\psi \mathrm{c}_\phi & \mathrm{s}_\psi \mathrm{s}_\theta \mathrm{c}_\phi - \mathrm{c}_\psi \mathrm{s}_\phi \\ -\mathrm{s}_\theta & \mathrm{c}_\theta \mathrm{s}_\phi & \mathrm{c}_\theta \mathrm{c}_\phi \end{bmatrix}$

and $\mathrm{s}_{(\cdot)}, \mathrm{c}_{(\cdot)}, \mathrm{t}_{(\cdot)}$ denote $\sin(\cdot), \cos(\cdot), \tan(\cdot)$, respectively. For translational rate command tracking tasks, it is necessary to obtain the relation between the local inertial translations (forward, lateral and vertical accelerations) and the main rotor thrust vector. For this purpose, Eqn. (4.4) is expressed in a new, vehicle-carried local reference frame by rotating the NED frame about its vertical axis by an angle ψ and translating it to the vehicle center of gravity. The local reference frame obtained thus has its Z-axis (local vertical) pointed vertically down, its X-axis (local horizontal) aligned with the helicopter's heading, and its Y-axis (local lateral) pointed port side. The translational equations of motion in the local frame can be approximated as follows:

$$\begin{bmatrix} a_x \\ a_y \\ a_z \end{bmatrix} = \frac{F_{\mathrm{mr}}}{m} \begin{bmatrix} -\sin\theta\cos\phi \\ \sin\phi \\ -\cos\theta\cos\phi \end{bmatrix} + \begin{bmatrix} 0 \\ 0 \\ g \end{bmatrix} + \begin{bmatrix} F'_h \\ F'_l \\ F'_z \end{bmatrix} \tag{4.5}$$

where $[F'_h \ F'_l \ F'_z]^{\mathrm{T}}$ represent force components excluding the main rotor thrust and gravity in the local frame. The translational motion of conventional helicopters from handling qualities perspective can be characterized by three distinct speed regimes: hover, low speed flight, and forward flight. Hover and low speed flight includes the flight envelope up to 23 m/s ground speed and forward flight includes the flight envelope beyond 23 m/s ground speed [4]. In hover and low speed flight, a lateral acceleration is typically designed to yield a proportional change in lateral velocity, whereas in forward flight a lateral acceleration is designed to yield a proportional turn rate. The forward and vertical accelerations in both flight regimes are designed to yield proportional changes in forward and vertical velocities, respectively. Thus:

$$a_x = \dot{V}_h \tag{4.6}$$

$$a_y = \begin{cases} \dot{V}_l & \ldots \text{hover and low speed} \\ \dot{\chi} V_h & \ldots \text{forward flight} \end{cases} \tag{4.7}$$

$$a_z = \dot{V}_z \tag{4.8}$$

The helicopter plant model described by Eqns. (4.1)–(4.4) is implemented in real-time using the software package GenSim, which is a comprehensive model developed and validated over the past three decades. For the interested reader, Refs. [93, 94] describe GenSim's structure in greater detail, and Ref. [95] presents a comparison between similar state-of-the-art comprehensive rotorcraft models. The schematic of GenSim is reproduced from Ref. [93] in the following Fig. 4.1 for convenience. It shows a modular architecture for the different helicopter structural components, as well as the interactions and the data flow between them. Additionally, characteristic rotorcraft phenomena such as in ground and out of ground effects are also modeled and simulated by GenSim. GenSim permits the vehicle, aeromechanical and simulation parameters to be set by input data files, and during runtime it outputs the fuselage and rotor states for visualization and feedback purposes. For the simulation studies undertaken in this thesis, the vehicle and aeromechanical parameters for a BO105 model, which has a hingeless rotor system, are chosen. Thus, the helicopter plant model simulates realistic flight dynamics that are suitable for an economical assessment of flight guidance and control algorithms.

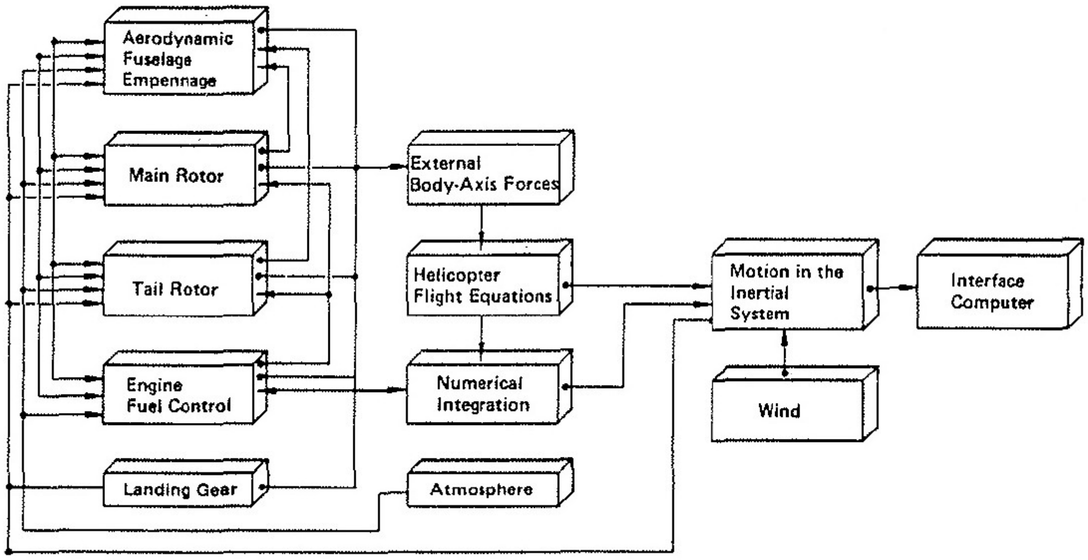

Figure 4.1: Code structure of the GenSim flight mechanics model, adapted from Ref. [93]

4.2 Model Linearization and Eigenspace Analysis

The vehicle dynamics in Eqns. (4.1)–(4.4) are not affine in terms of the pilot controls, namely displacements of the cyclic stick, the collective stick, and the pedals. Similarly, the Euler angles appear in the translational Eqn. (4.5) as trigonometric functions. To ease controller development, the nonlinear dynamics are linearized in this section. In addition to easing the control law development, a linearized system is well suited to analyze the stability characteristics of a bare-airframe helicopter.

For linearizing the vehicle dynamics, operating points are defined at fixed airspeed intervals of 5 m/s between hover ($V = 0\,\mathrm{m/s}$) and forward flight ($V = 70\,\mathrm{m/s}$) in steady, straight, and level flight condition. At each operating point, a trim routine determines the set of control inputs that yields steady-state conditions ($\dot{\mathbf{v}}_\mathbf{b} \to \mathbf{0}$, $\dot{\boldsymbol{\omega}} \to \mathbf{0}$). Numerical perturbations around the steady-state then yield the stability and control derivatives, $\mathbf{A}^*$ and $\mathbf{B}^*$, respectively, which are conveniently expressed in the state–space form as:

$$\dot{\mathbf{x}}_8(t) \quad = \quad \mathbf{A}^*\mathbf{x}(t) + \mathbf{B}^*\mathbf{u}(t) \tag{4.9}$$

where $\mathbf{x}_8 \equiv [\phi\ \theta\ u\ v\ w\ p\ q\ r]^T \in \mathbb{R}^8$ and $\mathbf{u} \equiv [D_\theta\ D_\alpha\ D_\beta\ D_\delta]^T \in \mathbb{R}^4$ denote change from trim at any operating point. It is found that the pair $\{\mathbf{A}^*, \mathbf{B}^*\}$ is controllable and $\mathbf{B}^*$ is full column rank over the full flight envelope. Note that, for the purpose of control design, rotor states have been neglected as they operate at much higher frequencies than the fuselage states that operate in the medium and low frequency range. Instead, the steady-state effects of the rotor modes are directly absorbed into the stability and control derivatives. Although rotor state feedback has shown to improve controller bandwidth and disturbance rejection for advanced rotorcraft applications, real-time measurements of rotor states is expensive and impractical. For this reason, rotor state feedback is considered beyond the scope of this work.

Fig. 4.2 plots the open loop eigenvalues of Eqn. (4.9). It can be seen that the phugoid mode, with positive real parts, is unstable over the full speed range. Among the other longitudinal modes, the heave mode is lightly damped and the pitch mode is heavily damped. Among the lateral/directional modes, the Dutch roll mode is lightly damped and its period varies with forward speed. While the spiral mode is lightly damped, the roll mode is heavily damped. Previous works reporting on flight testing the BO105 [96,

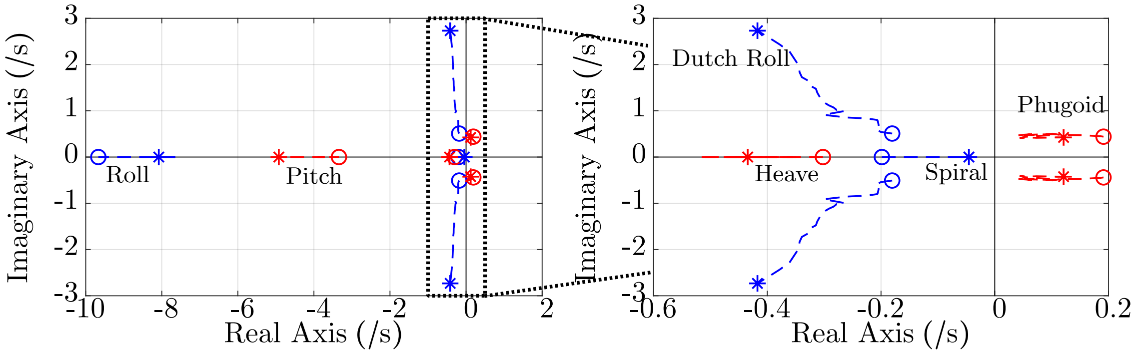

Figure 4.2: BO105 open-loop eigenvalues using quasi-steady 6-DOF linear model (- - -longitudinal modes, - - -lateral-directional modes, ∘ ∘ hover, ∗ ∗ 70 m/s)

97] and those identifying the linear system models of the BO105 [6] corroborate the findings in Fig. 4.2.

Finally, the simplified translational dynamics of Eqn. (4.5) are linearized such that the forward and lateral accelerations are affine in terms of the attitude angles. The following linear translational system is obtained:

$$\begin{bmatrix} a_x \\ a_y \end{bmatrix} \approx \begin{bmatrix} -g & g\tan\theta\tan\phi \\ 0 & g/(\cos\theta) \end{bmatrix} \begin{bmatrix} \Delta\theta \\ \Delta\phi \end{bmatrix} \tag{4.10}$$

where Δ identifies changes from trim. Note that in obtaining Eqn. (4.10), velocity stability derivatives have been neglected due to their much smaller influence as compared to the control derivatives.

4.3 Turbulence Model

A realistic simulation of harsh environmental conditions, such as the influence of ship airwakes on the helicopter dynamics, requires high fidelity turbulence models. However, conventional methods for turbulence modeling in rotorcraft applications suffer from high complexity and computational cost. The need for simpler, real-time-capable turbulence simulation for helicopter control design purposes led to the development of an empirical

Control Equivalent Turbulence Input (CETI) model. CETI was originally proposed by Lusardi et al. for the UH-60 Black Hawk [98] and later extended by Seher-Weiss et al. for the EC135 [99]. The underlying principle is to use flight test data and system identification methods to extract white-noise driven turbulence filters that reproduce the same system responses as real gusts. Previous flight control applications that used CETI include a SA330 Puma helicopter in a shipboard approach [24], and a precision hover task of a BO105 helicopter [18]. The CETI filters representing high turbulence in hover and low speed are identified by the following structure [99]:

$$\frac{\delta D_\beta}{W_n} = \frac{5.99}{(s+3)} \tag{4.11}$$

$$\frac{\delta D_\alpha}{W_n} = \frac{6.07}{(s+3)} \tag{4.12}$$

$$\frac{\delta D_\delta}{W_n} = \frac{21.5}{(s+7.28)} \tag{4.13}$$

$$\frac{\delta D_\theta}{W_n} = \frac{0.974(s+60)}{(s+1.89)(s+15)} \tag{4.14}$$

The nature of the turbulence inputs are illustrated in Fig. 4.3. The figure shows the percentage of displacements of the main rotor longitudinal cyclic, main rotor lateral cyclic, main rotor collective, and tail rotor collective simulated for 10 s. To simulate turbulence in closed-loop, these CETI filter outputs are superimposed on the controller output before inserting the sum in the plant model. Note that Eqns. (4.11)–(4.14) were obtained from EC135 tests and are primarily applicable in hover and low speed flight. However, due to the similarity of the EC135 and BO105 rotor systems, Eqns. (4.11)–(4.14) are assumed to be applicable to the BO105 model. This assumption is also validated by previous works applying the EC135 turbulence filters to a BO105 physical model [18]. Moreover, as turbulence filters in forward flight are not yet available, Eqns. (4.11)–(4.14) will be used for a qualitative assessment in forward flight in the simulations that follow.

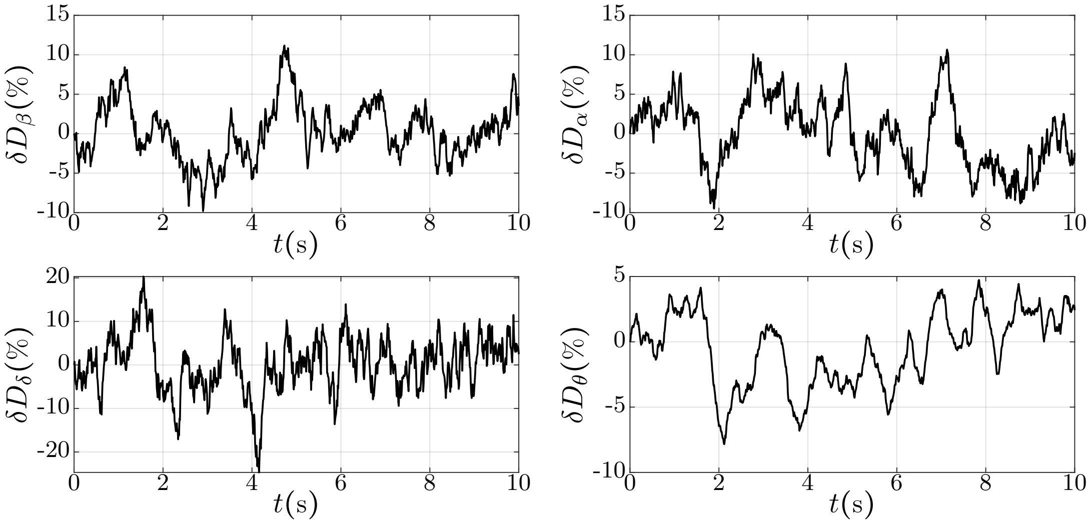

Figure 4.3: Illustration of control equivalent turbulence inputs applied to the main and tail rotor actuators

4.4 Matlab/Simulink Environment

The helicopter simulation model described in Sec. 4.1, together with the robust control design and optimal guidance laws that will be developed in Chapters 5–7, are hosted in a Matlab/Simulink framework within a rotorcraft simulation environment as described in Ref. [100]. The Matlab/Simulink development environment handles all internal data exchange between the controller and the plant, as well as external data exchange with the cockpit and the image generator. Fig. 4.4 depicts a high-level Simulink block diagram. It consists of a simulation control and flight control block, a flight dynamics block, a visualization block and an output feedback block. The simulation pace is set such that 1 s of simulation time corresponds to 1 s of clock time to yield real-time capability.

Fig. 4.5 shows the modules that comprise the flight dynamics block. The GenSim plant model has been originally developed in Fortran. For simulation purposes, the Fortran code is integrated as an external S-function into Simulink and is operated at 1000 Hz. This S-function receives parametric and control inputs at runtime and it outputs the fuselage and rotor states as outputs. Next, Fig. 4.6 shows the modules contained within

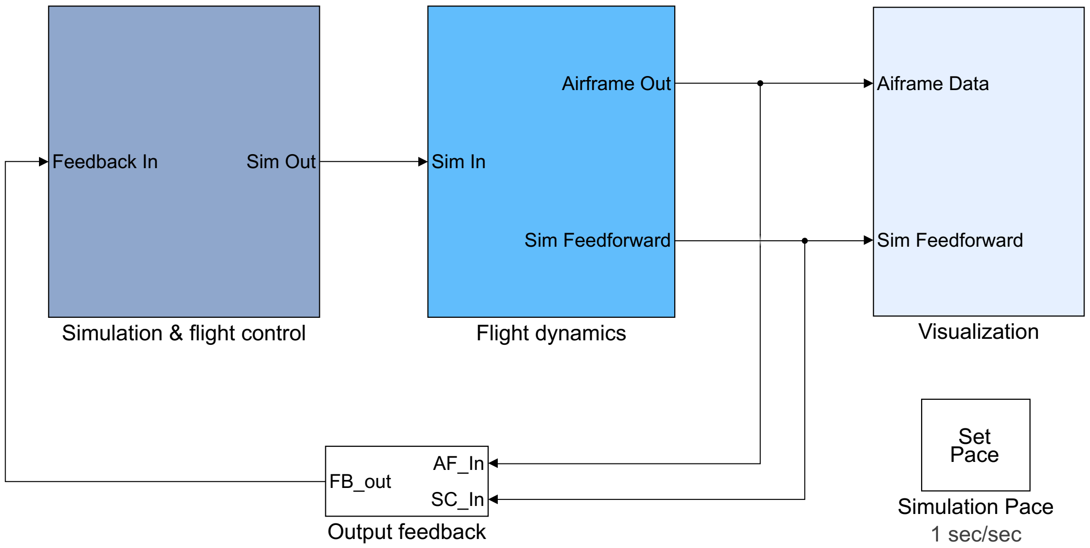

Figure 4.4: High-level view of Matlab/Simulink environment [100]

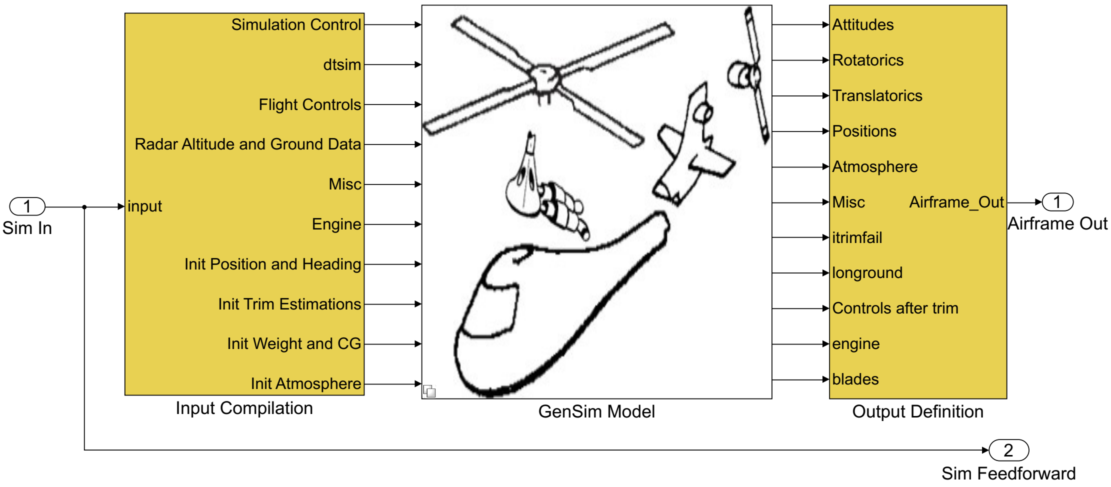

Figure 4.5: View of the flight dynamics block [100]

the simulation and flight control block. In this block, all the simulation parameters that are required at simulation start, including sampling time, initial trim estimates, and initial flight condition (position, speeds), are set. Runtime data required by GenSim, including control commands, engine parameters, switches, and environmental conditions are also supplied by this block. The guidance and control algorithms that are developed

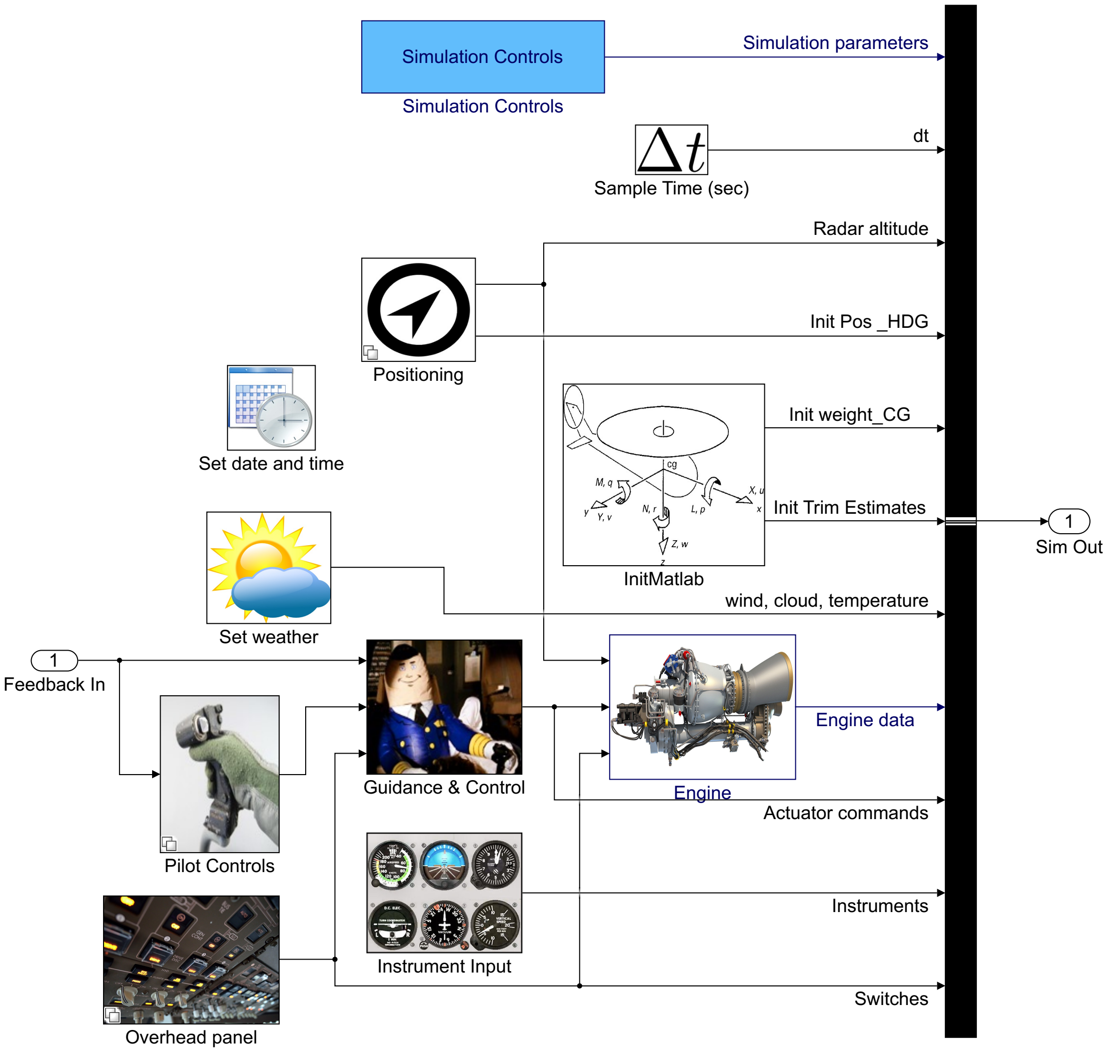

Figure 4.6: View of the simulation and flight control block [100]

in the following sections are integrated into the "Guidance & Control" module in Fig. 4.6. This module is operated at 100 Hz, which is of the same order of magnitude at which modern computing platforms of most serial helicopter avionics suites are operated.

5 Robust Helicopter Control Design

`This chapter is based on the following journal publication:`

[J2] O. Halbe and M. Hajek, “Robust Helicopter Sliding Mode Control for Enhanced Handling and Trajectory Following,” *Journal of Guidance, Control, and Dynamics*, vol. 43, no. 10, pp. 1805–1821, 2020.

FOLLOWING the theoretical foundation of the sliding mode control technique outlined in Chapter 3, this chapter aims to synthesize sliding mode control laws that satisfy helicopter handling quality specifications and robustness to interaxis coupling, turbulence, and other unmodeled dynamics. In this approach, first the required response types for enhancing helicopter handling qualities are specified, followed by a synthesis of a two-loop control architecture. Finally, stability analyses of the proposed control architecture and a comparative assessment with an explicit model following controller are presented.

5.1 Required Response Types

Helicopter handling becomes easier as the perceived closed loop dynamics move closer to an ideal system. The equivalent systems approach for enhancing HQ prescribes idealized lower order axial response characteristics in helicopters that are otherwise characterized by higher order dynamic modes [9]. The present work aims to demonstrate predicted Level 1 handling, autonomous execution of MTEs requiring moderate to aggressive agility, and turbulence rejection properties. For attitude and rate commands, the following response-types are chosen: attitude command attitude hold (ACAH) in both pitch and roll axes, rate command height hold (RCHH) in the vertical axis, and rate command direction hold (RCDH) in the yaw axis. While ACAH tracks the commanded attitude (pitch or roll) using the cyclic control input, RCHH tracks a commanded inertial vertical speed via normal speed dynamics and the collective control input. RCDH provides directional control in hover and low speed using the pedal input, and ensures turn coordination in forward flight. To assure predicted Level 1 HQs for each response-type, the on-axis responses must satisfy amplitude requirements at three levels: small, moderate, and large, and frequency requirements in three ranges ranges: long-term, mid-term, and short-term behavior. Moreover, the off-axis responses to on-axis inputs must remain within their specified bounds [4]. To satisfy these requirements, previous studies sought to define the on-axis responses as ideal transfer functions and to design feedback gains for satisfying the required closed-loop control performance [5, 17, 28]. This approach is particularly attractive because it offers design flexibility in choosing closed-loop response characteristics, while remaining independent of the underlying helicopter dynamics. Following previous studies, pitch and roll ACAH response-types in this work are specified as ideal second-order transfer functions, and RCDH and RCHH are specified as ideal first-order transfer functions, as follows:

$$\text{ACAH:} \quad \dot{\theta} + 2\zeta_\theta\omega_\theta\theta + \omega_\theta^2 \int_0^t (\theta - \theta_c)d\tau = 0 \tag{5.1}$$

$$\dot{\phi} + 2\zeta_\phi\omega_\phi\phi + \omega_\phi^2 \int_0^t (\phi - \phi_c)d\tau = 0 \tag{5.2}$$

$$\text{RCDH:} \quad r + \lambda_r \int_0^t (r - r_c)d\tau = 0 \tag{5.3}$$

$$\text{RCHH:} \quad w + \lambda_z \int_0^t (w - w_c)d\tau = 0 \tag{5.4}$$

It has been suggested in [37] that bandwidth (ω_{bw}), which is the stability margin available for piloting tasks, plays a critical role in ensuring Level 1 HQ.

For the second-order ACAH response types in Eqns. (5.1)–(5.2), the bandwidth is the frequency at which the phase angle between command signal and output signal is −135°. From [37], ω_{bw} can be expressed in terms of the natural frequency and the damping ratio as follows:

$$\omega_{\text{bw},\theta} = \omega_\theta(\zeta_\theta + \sqrt{\zeta_\theta^2 + 1}) \tag{5.5}$$

$$\omega_{\text{bw},\phi} = \omega_\phi(\zeta_\phi + \sqrt{\zeta_\phi^2 + 1}) \tag{5.6}$$

Here, $\omega_{\text{bw},(\theta,\phi)} > 2\,\text{rad/s}$ satisfies Level 1 HQ for both pitch and roll response types [4, 5, 37]. The ACAH response parameters in this work are used from recent helicopter HQ studies [28]: $\zeta_\theta = 0.9$, $\omega_\theta = 2.34$, $\zeta_\phi = 0.75$, $\omega_\phi = 2.34$, which yield $\omega_{\text{bw},\theta} = 5.25\,\text{rad/s}$ and $\omega_{\text{bw},\phi} = 4.68\,\text{rad/s}$. Fig. 5.1b shows that the pitch and roll bandwidth values correspond to their respective −135° phase angles. Furthermore, the required limits on pitch and roll oscillations, according to [4], are plotted in Fig. 5.1a. This suggests that the ACAH transfer function structure and parameters will ensure Level 1 HQ for both pitch and roll responses.

For the first-order RCDH and RCHH response types in (5.3)–(5.4), the bandwidth is defined by the cutoff frequency at −3 dB. For Level 1 HQ, $\omega_{\text{bw},r} > 2\,\text{rad/s}$ and $\omega_{\text{bw},w} > 0.2\,\text{rad/s}$ are required according to [4, 5]. Using $\lambda_r = 4$ and $\lambda_w = 0.8$ from [28], $\omega_{\text{bw},r} = 4\,\text{rad/s}$ and $\omega_{\text{bw},w} = 0.8\,\text{rad/s}$ are obtained. Fig. 5.1b shows that these yaw and heave bandwidth values correspond to their respective −3 dB gain limits.

Further, a translational rate command (TRC) response-type is chosen for trajectory following and execution of guidance commands. In hover and low speed TRC, pitch and roll attitudes produce a proportional change in forward and lateral velocities, respectively. In forward flight TRC, pitch and roll attitudes produce a proportional change in forward velocity and turn rate, respectively. Furthermore, ADS-33 requires a qualitative first-order behavior for the translational rates. To satisfy these requirements, the track-

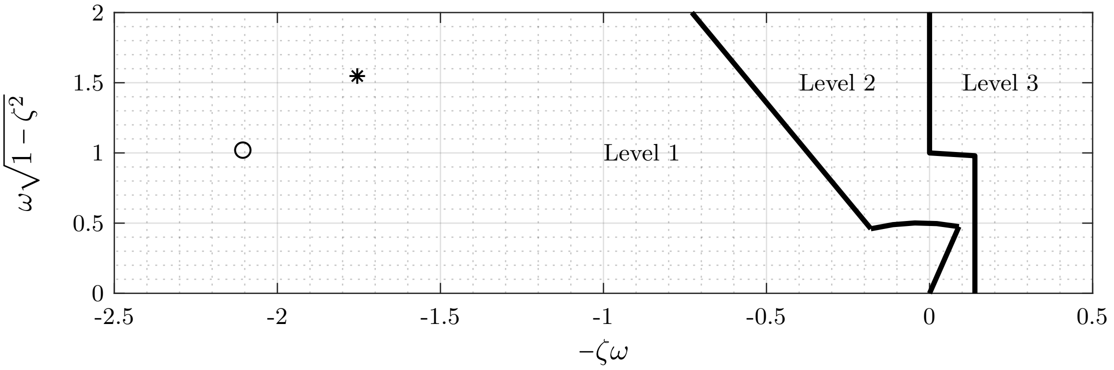

(a) Limits on pitch and roll oscillations [4], ∘ required pitch, ⁎ required roll

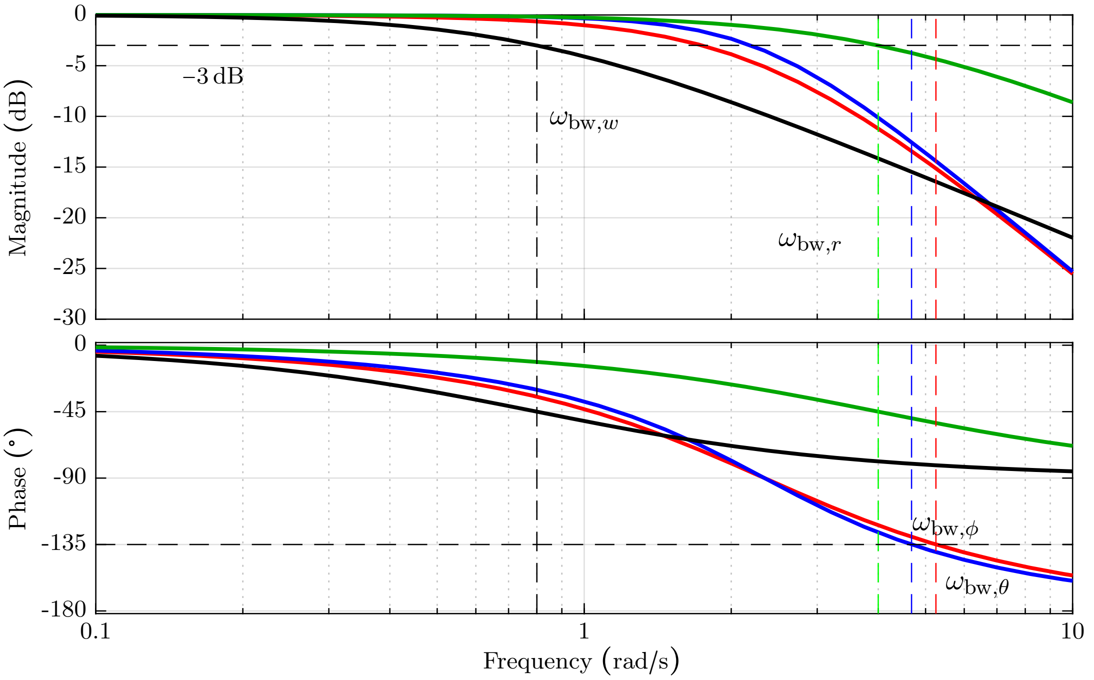

(b) Bode plot of required axial responses, — θ, — ϕ, — r, and — w

Figure 5.1: Frequency characteristics of the attitude command response types

ing errors in the ground velocities and the track angle are specified as ideal first-order transfer functions, as follows:

$$\text{TRC:} \quad (V_h - V_{h,c}) + \lambda_h \int_0^t (V_h - V_{h,c}) d\tau = 0 \tag{5.7}$$

$$\text{TRC hover/low speed:} \quad (V_l - V_{l,c}) + \lambda_h \int_0^t (V_l - V_{l,c}) d\tau = 0 \tag{5.8}$$

$$\text{TRC forward flight:} \quad (\chi - \chi_c) + \lambda_\chi \int_0^t (\chi - \chi_c) d\tau = 0 \tag{5.9}$$

Table 5.1: Summary of required on-axis response-types and parametric values

Commanded state	Intermediate state	Response-type	Flight envelope	ζ	ω	λ
θ	–	ACAH	full	0.9	2.34	–
ϕ	–	ACAH	full	0.75	2.34	–
r	–	RCDH	full	–	–	4
V_z	w	RCHH	full	–	–	0.5
V_l	ϕ	TRC	hover/low speed	–	–	0.2
V_h	θ	TRC	full	–	–	0.2
χ	ϕ	TRC	forward flight	–	–	0.1

Note that the set of ideal transfer functions Eqns. (5.1)–(5.9) is independent of the plant model. Table. 5.1 summarizes all commanded states and response-types. As discussed, the system parameters shown in Table. 5.1 are those that accord predicted Level 1 HQs based on previous studies [28, 5]. Moreover, these parametric values assure higher bandwidths in both pitch and roll ACAH response-types, as compared to the TRC response-type, which ensures adequate time-scale separation [28]. In summary, the control problem is to synthesize robust feedback control laws that ensure:

1. Required on-axis responses to on-axis control inputs according to Eqns. (5.1)–(5.9)
2. Regulation of off-axis responses to on-axis control inputs according to ADS-33 quantitative criteria
3. Stability of the overall closed-loop control architecture
4. Trajectory following in MTEs requiring moderate to aggressive agility

5. Turbulence rejection in shipboard approach and precision hover tasks

5.2 Sliding Mode Control Objectives

SMC-based robust control laws in a two-loop control architecture are now developed according to the steps outlined in Sec. 3.1.2. In a conventional helicopter configuration, the main rotor thrust magnitude controls its normal translation, the main rotor thrust inclination controls its pitch and roll rates, and the tail rotor thrust magnitude controls its yaw rate. For helicopter multivariable control law synthesis, it is thus prudent to group in the inner loop all directly actuated fuselage states, namely pitch and roll attitudes and angular rates, normal velocity, and yaw rate, even if they all do not operate on the same time scale. The translational rates required for guidance command execution are grouped in the outer loop. For controller synthesis, the problem statements in Sec. 5.1 can be translated into SMC objectives for the inner and outer loops as follows:

1. Design sliding surfaces to enforce ideal on-axis system responses according to Eqns. (5.1)–(5.9) and Table 5.1, and to asymptotically track the reference command signal, $\lim_{t\to\infty} \|\mathbf{y}(t) - \mathbf{r}(t)\| = 0$

2. Induce and sustain sliding motion in the presence of matched, bounded uncertainties in the form of interaxis coupling elements, turbulence effects, and any unmodeled dynamics

3. Ensure single-loop and two-loop stability

5.3 Attitude/Rate Command Sliding Mode Control

For simplicity, the notations used in Sec. 3.1.2 are retained in the inner loop control synthesis. The inner loop state, control, output, and command signal vectors are $\mathbf{x}_6 \equiv [\phi\ \theta\ w\ p\ q\ r]^{\mathrm{T}}$, $\mathbf{u} \equiv [D_\theta\ D_\alpha\ D_\beta\ D_\delta]^{\mathrm{T}}$, $\mathbf{y} \equiv [\phi\ \theta\ w\ r]^{\mathrm{T}}$, and $\mathbf{r} \equiv [\phi_c\ \theta_c\ w_c\ r_c]^{\mathrm{T}}$, respectively.

Note that u and v are omitted from the inner loop state vector as inertial translational commands are handled in the outer loop. The subscript in $\mathbf{x}_6$ is also dropped for brevity. The command vector is partitioned as $\mathbf{r} = [\mathbf{r}_1\ \mathbf{r}_2]^{\mathrm{T}}$, where $\mathbf{r}_1 \equiv [\phi_c\ \theta_c]^{\mathrm{T}}$ is generated by an outer loop TRC SMC, and $\mathbf{r}_2 \equiv [w_c\ r_c]^{\mathrm{T}}$ is generated using the respective kinematic relationships for trajectory following. As discussed previously, identification of cross-coupling system and control derivatives are found to have varying degrees of mismatch with actual flight data [6]. For this reason, all on-axis derivatives are separated from all off-axis derivatives in the stability matrix $\mathbf{A}^*$ and in the control matrix $\mathbf{B}^*$. The resulting on-axis stability and control matrices, $\mathbf{A}$ and $\mathbf{B}$, respectively, are therefore block-diagonal. All off-axis derivatives, together with CETI terms and any unmodeled dynamics are grouped into the unknown but bounded function $\mathbf{f}(\mathbf{x}, \mathbf{u} + \delta\mathbf{u}, t)$, where $\delta\mathbf{u}$ represents the CETI terms. This formulation has the effect of enhancing robustness to cross-coupling effects, albeit at the expense of higher gains of the discontinuous control terms. However, it will be shown in the simulation results that both chattering and saturation effects can be effectively mitigated by this approach. Using Eqn. (3.1)–(3.2), the uncertain inner loop linear system can be expressed as follows:

$$\begin{aligned} \dot{\mathbf{x}}(t) &= \mathbf{A}\mathbf{x}(t) + \mathbf{B}\mathbf{u}(t) + \mathbf{f}(\mathbf{x}, \mathbf{u} + \delta\mathbf{u}, t) && (5.10) \\ \mathbf{y}(t) &= \mathbf{C}\mathbf{x}(t) && (5.11) \end{aligned}$$

It is assumed that $\mathbf{f}(\mathbf{x}, \mathbf{u} + \delta\mathbf{u}, t) = \mathbf{B}\,\boldsymbol{\Gamma}(\mathbf{x}, \mathbf{u} + \delta\mathbf{u}, t)$ and $\|\boldsymbol{\Gamma}\| \leq L$, a known upper bound. This assumption holds because the upper bounds of the cumulative off-axis responses and turbulence effects can be estimated using flight or model data within the operational flight domain. Furthermore, although the pitch and roll attitude dynamics are unmatched, they do not contain any uncertainties. Thus, both matching and boundedness conditions of the uncertainties are satisfied. Next, as discussed in Sec. 3.1.2, $(\mathbf{A}, \mathbf{B}, \mathbf{C})$ are obtained in a special canonical form, known as the regular form, as follows:

$$\mathbf{A} = \begin{bmatrix} \mathbf{A}_{11} & \mathbf{A}_{12} \\ \mathbf{A}_{21} & \mathbf{A}_{22} \end{bmatrix} \quad \mathbf{B} = \begin{bmatrix} \mathbf{0} \\ \mathbf{B}_2 \end{bmatrix} \quad \mathbf{C} = \begin{bmatrix} \mathbf{C}_1 & \mathbf{C}_2 \end{bmatrix} \tag{5.12}$$

where $\mathbf{A}_{11} \in \mathbb{R}^{2\times 2}$, $\mathbf{A}_{12} \in \mathbb{R}^{2\times 4}$, $\mathbf{A}_{21} \in \mathbb{R}^{4\times 2}$, $\mathbf{A}_{22} \in \mathbb{R}^{4\times 4}$, $\mathbf{B}_2 \in \mathbb{R}^{4\times 4}$, $\mathbf{C}_1 \in \mathbb{R}^{4\times 2}$, and $\mathbf{C}_2 \in \mathbb{R}^{4\times 4}$. Also see Appendix A for details of the matrix structure.

Now, according to the first step in SMC synthesis, the output tracking error vector is defined as $\dot{\mathbf{x}}_e = (\mathbf{y} - \mathbf{r})$ and the augmented state vector becomes $\tilde{\mathbf{x}} \equiv [\mathbf{x}_e \ \mathbf{x}]^{\mathrm{T}}$. $\tilde{\mathbf{x}}$ can be repartitioned into unmatched and matched states as $\tilde{\mathbf{x}} \equiv [\mathbf{x}_1 \ \ \mathbf{x}_2]^{\mathrm{T}}$ where $\mathbf{x}_1 \in \mathbb{R}^6$ and $\mathbf{x}_2 \in \mathbb{R}^4$. The augmented uncertain system dynamics are then obtained as:

$$\begin{bmatrix} \dot{\mathbf{x}}_1 \\ \dot{\mathbf{x}}_2 \end{bmatrix} = \begin{bmatrix} \tilde{\mathbf{A}}_{11} & \tilde{\mathbf{A}}_{12} \\ \tilde{\mathbf{A}}_{21} & \tilde{\mathbf{A}}_{22} \end{bmatrix} \begin{bmatrix} \mathbf{x}_1 \\ \mathbf{x}_2 \end{bmatrix} + \begin{bmatrix} \mathbf{0} \\ \mathbf{B}_2 \end{bmatrix} \mathbf{u} - \begin{bmatrix} \mathbf{T}_1 \\ \mathbf{0} \end{bmatrix} \mathbf{r} + \begin{bmatrix} \mathbf{0} \\ \mathbf{B}_2\boldsymbol{\Gamma} \end{bmatrix} \tag{5.13}$$

Note from Eqn. (5.13) that while the uncertainties present in $\mathbf{x}_2$ are matched, the reference commands in $\mathbf{x}_2$ are unmatched. Eqn. (5.13), when written in compact form, yields the same form as Eqn. (3.5) and is reproduced for clarity:

$$\dot{\tilde{\mathbf{x}}} = \tilde{\mathbf{A}}\tilde{\mathbf{x}} + \tilde{\mathbf{B}}\mathbf{u} - \tilde{\mathbf{T}}\mathbf{r} + \tilde{\mathbf{f}} \tag{5.14}$$

In the second step, a suitable sliding surface is designed to enforce the ideal system behavior, specified by Eqns. (5.1)–(5.4), as follows:

$$\boldsymbol{\sigma} = \begin{bmatrix} w + \lambda_w \int_0^t (w - w_c) d\tau \\ r + \lambda_r \int_0^t (r - r_c) d\tau \\ \dot{\phi} + 2\zeta_\phi \omega_\phi \phi + \omega_\phi^2 \int_0^t (\phi - \phi_c) d\tau \\ \dot{\theta} + 2\zeta_\theta \omega_\theta \theta + \omega_\theta^2 \int_0^t (\theta - \theta_c) d\tau \end{bmatrix} \tag{5.15}$$

In terms of the new state vector $\tilde{\mathbf{x}}$, the sliding surface of Eqn. (5.15) can be written as:

$$\mathcal{S} = \{(\mathbf{x}_1, \mathbf{x}_2) : \boldsymbol{\sigma} = \mathbf{S}_1\mathbf{x}_1 + \mathbf{S}_2\mathbf{x}_2 = \mathbf{0}\} \tag{5.16}$$

where $\mathbf{S}_1$ and $\mathbf{S}_2$ contain the corresponding ideal system parameters listed in Table 5.1 (also see Appendix A). When sliding motion is induced, $\boldsymbol{\sigma} = \mathbf{0}$. Since $\mathbf{S}_2$ is square and nonsingular for nonzero gains, it follows that $\mathbf{x}_2 = -\mathbf{S}_2^{-1}\mathbf{S}_1\mathbf{x}_1$. Using Eqn. (5.13), one obtains:

$$\dot{\mathbf{x}}_1 = (\tilde{\mathbf{A}}_{11} - \tilde{\mathbf{A}}_{12}\mathbf{S}_2^{-1}\mathbf{S}_1)\mathbf{x}_1 - \mathbf{T}_1\mathbf{r} \tag{5.17}$$

Since the nominal system is controllable, the pair $(\tilde{\mathbf{A}}_{11}, \tilde{\mathbf{A}}_{12})$ is also controllable in accordance with [38]. Furthermore, Eqn. (5.17) reveals that ideal sliding motion yields a system where the output tracking errors in $\mathbf{x}_1$ are insensitive to the uncertainties.

In the third step, a control law is proposed to drive the system in Eqn. (5.13) to the sliding manifold in Eqn. (5.16) and sustain the sliding motion thereafter. In physical terms, the helicopter is expected to exhibit the required attitude and normal response characteristics on the sliding manifold. For simplicity, setting $\boldsymbol{\Phi} = -0.5\,\mathbf{I}_{4\times4}$ in the Lyapunov equation gives $\mathbf{P} = \mathbf{I}_{\mathbf{4}\times\mathbf{4}}$. The inner loop continuous control law is then obtained according to Eqn. (3.13) as:

$$\mathbf{u} \;=\; -(\mathbf{S}\tilde{\mathbf{B}})^{-1}\Big((\mathbf{S}\tilde{\mathbf{A}} - 0.5\,\mathbf{S})\tilde{\mathbf{x}} + \mathbf{S}\tilde{\mathbf{T}}\mathbf{r}_h - \boldsymbol{\rho}\,\mathrm{SAT}(\boldsymbol{\sigma}/\epsilon)\Big) \tag{5.18}$$

where $\mathbf{S} = [\mathbf{S}_1\ \mathbf{S}_2]$, $\boldsymbol{\rho} = \mathrm{diag}(\rho_1, \rho_2, \rho_3, \rho_4)$, and $\mathrm{SAT}(\boldsymbol{\sigma}/\epsilon) = [\mathrm{sat}(\sigma_1/\epsilon)\ \ldots\ \mathrm{sat}(\sigma_4/\epsilon)]^{\mathrm{T}}$. Note that an optional PCH layer can be added to the inner loop so that $\boldsymbol{\sigma}$ in Eqn. (5.18) is computed using $\mathbf{r}_h$, where $\mathbf{r}_h$ is computed from $\mathbf{r}$ according to Eqn. (3.41). However, when control saturation is not an issue, $\mathbf{r}$ from the outer loop can be directly applied to Eqn. (5.18).

As shown in Sec. 3.1.2, the boundary layer is reached in finite time despite the continuous approximation in Eqn. (5.18). However, ideal sliding motion does not occur within the boundary layer and the system is not completely insensitive to the matched uncertainties [38]. When the saturation element operates in the linear region (i.e., $\|\boldsymbol{\sigma}\| \leqslant \epsilon$), the augmented inner loop SMC law has a high-gain PID-like structure, as follows:

$$\mathbf{u} = -(\mathbf{S}\tilde{\mathbf{B}})^{-1}\Big((\mathbf{S}\tilde{\mathbf{A}} - 0.5\mathbf{S} + \frac{\boldsymbol{\rho}}{\epsilon}\mathbf{S})\tilde{\mathbf{x}} - \mathbf{S}\tilde{\mathbf{T}}\mathbf{r}\Big) \tag{5.19}$$

Substituting Eqn. (5.19) in Eqn. (5.14), one obtains:

$$\dot{\tilde{\mathbf{x}}} = \Big(\tilde{\mathbf{A}} - \tilde{\mathbf{B}}(\mathbf{S}\tilde{\mathbf{B}})^{-1}(\mathbf{S}\tilde{\mathbf{A}} - \boldsymbol{\Phi}\mathbf{S} + \frac{\boldsymbol{\rho}}{\epsilon}\mathbf{S})\Big)\tilde{\mathbf{x}} + \Big(\tilde{\mathbf{B}}(\mathbf{S}\tilde{\mathbf{B}})^{-1}\mathbf{S}\tilde{\mathbf{T}} - \tilde{\mathbf{T}}\Big)\mathbf{r} + \tilde{\mathbf{f}} \tag{5.20}$$

The closed-loop augmented system in Eqn. (5.20) is of the form $\dot{\tilde{\mathbf{x}}} = (\tilde{\mathbf{A}} - \tilde{\mathbf{B}}\tilde{\mathbf{K}}_1)\tilde{\mathbf{x}} + (\tilde{\mathbf{B}}\tilde{\mathbf{K}}_2 - \tilde{\mathbf{T}})\mathbf{r} + \tilde{\mathbf{f}}$. Fig. 5.2 plots the closed-loop eigenvalues of the nominal augmented system that are found to have negative real parts. Furthermore, the eigenvalue variations with airspeed are small. This suggests that the closed-loop nominal system is stabilized within the boundary layer, and that the system responses between hover, low speed, and forward flight are uniform.

5.4 Translational Rate Command Using Sliding Mode Control

In forward flight, the outer loop state, control, output, and command vectors are denoted by $\mathbf{z} \equiv [\chi \; V_h]^{\mathrm{T}}$, $\mathbf{r}_1 \equiv [\phi \; \theta]^{\mathrm{T}}$, $\mathbf{w} \equiv [\chi \; V_h]^{\mathrm{T}}$, and $\mathbf{q} \equiv [\chi_c \; V_{h,c}]^{\mathrm{T}}$, respectively. Note that, in obtaining Eqn. (4.10), the nonlinearities have been neglected and the coupling of attitudes and translations has been simplified. For this reason, the TRC SMC law needs to be robust to the unknown but bounded uncertainties. Using Eqn. (4.10), the

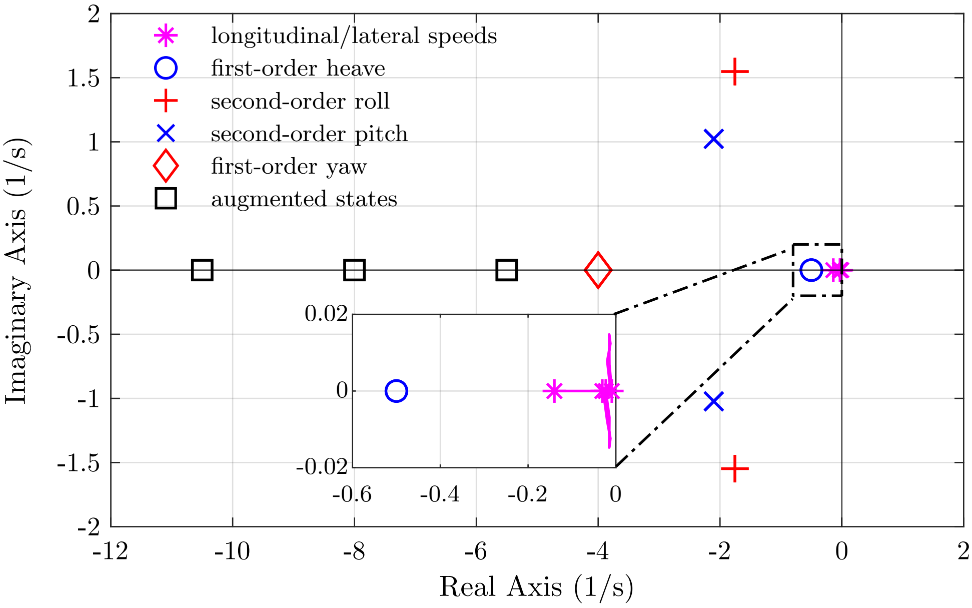

Figure 5.2: BO105 closed-loop eigenvalues using SMC feedback (0 m/s to 70 m/s)

horizontal inertial translational dynamics are written as:

$$\dot{\mathbf{z}}(t) = \mathbf{F}\mathbf{z}(t) + \mathbf{G}\mathbf{r}_1(t) + \mathbf{d}(\mathbf{z}, \mathbf{r}_1, t) \tag{5.21}$$

$$\mathbf{w}(t) = \mathbf{H}\mathbf{z}(t) \tag{5.22}$$

where $\mathbf{F} = \mathbf{0}_{2\times2}$, $\mathbf{G}$ from Eqn. (4.10), and $\mathbf{H} = \mathbf{I}_2$ are already in regular form. The disturbance term that groups the nonlinearities and any neglected effects of the pitch and roll attitudes on the translational rates is matched and assumed to be bounded, so that $\mathbf{d}(\mathbf{z}, \mathbf{r}_1, t) = \mathbf{G}\,\boldsymbol{\Gamma}_o(\mathbf{z}, \mathbf{r}_1, t)$ and $\|\boldsymbol{\Gamma}_o\| \leq L_o$. The control objective is for the command signal $\mathbf{q}$ to asymptotically track the output $\mathbf{w}$, and enforce the required closed-loop behavior of Eqns. (5.7)–(5.9).

In the first step, defining the tracking error as $\dot{\mathbf{z}}_e = (\mathbf{w} - \mathbf{q})$, the augmented state vector is obtained as $\tilde{\mathbf{z}} \equiv [\mathbf{z}_e \ \mathbf{z}]^{\mathrm{T}}$. Since the number of outputs is identical to the number of inputs, a further partitioning is not necessary. The augmented system dynamics are expressed as:

$$\begin{aligned}\dot{\tilde{\mathbf{z}}} &= \tilde{\mathbf{F}}\tilde{\mathbf{z}} + \tilde{\mathbf{G}}\mathbf{r}_1 - \tilde{\mathbf{T}}_o\mathbf{q} + \tilde{\mathbf{d}} \qquad (5.23)\\ \text{where} \quad \tilde{\mathbf{F}} &= \begin{bmatrix}\mathbf{0} & \mathbf{I}\\ \mathbf{0} & \mathbf{0}\end{bmatrix}, \quad \tilde{\mathbf{G}} = \begin{bmatrix}\mathbf{0}\\ \mathbf{G}\end{bmatrix}, \quad \tilde{\mathbf{T}}_o = \begin{bmatrix}\mathbf{I}\\ \mathbf{0}\end{bmatrix}, \text{and} \quad \tilde{\mathbf{d}} = \begin{bmatrix}\mathbf{0}\\ \mathbf{d}\end{bmatrix}\end{aligned}$$

In the second step, a sliding surface is designed for enforcing the required translational response characteristics in Eqns. (5.7)–(5.9). In forward flight, the sliding surface is obtained as:

$$\boldsymbol{\mu} = \begin{bmatrix}(\chi - \chi_c) + \lambda_\chi \int_0^t (\chi - \chi_c)d\tau\\ (V_h - V_{h,c}) + \lambda_h \int_0^t (V_h - V_{h,c})d\tau\end{bmatrix} \qquad (5.24)$$

and expressed in terms of the new state vector as:

$$\mathcal{R} = \{(\mathbf{z}_e, \mathbf{z}) : \boldsymbol{\mu} = \mathbf{R}_1\mathbf{z}_e + \mathbf{R}_2\mathbf{z} - \mathbf{R}_3\mathbf{q} = \mathbf{0}\} \qquad (5.25)$$

In the third step, a control law is proposed that drives the system of Eqn. (5.23) to the sliding surface of Eqn. (5.25) and sustains sliding motion thereafter. Using $\mathbf{\Phi} = -0.5\,\mathbf{I}_{2\times2}$, $\mathbf{P} = \mathbf{I}_{2\times2}$ as before, and replacing the discontinuous control term with a saturation function in Eqn. (3.13), the outer loop continuous control law is obtained as:

$$\mathbf{r}_1 = -(\mathbf{R}\tilde{\mathbf{G}})^{-1}\Big((\mathbf{R}\tilde{\mathbf{F}} - 0.5\mathbf{R})\tilde{\mathbf{z}} + (0.5\mathbf{R}_3 - \mathbf{R}\tilde{\mathbf{T}}_o)\mathbf{q}_h - \mathbf{R}_3\dot{\mathbf{q}}_h + \boldsymbol{\rho}_o\text{sat}(\boldsymbol{\mu}/\epsilon_o)\Big) \qquad (5.26)$$

where $\mathbf{R} = [\mathbf{R}_1\ \mathbf{R}_2]$, $\boldsymbol{\rho}_o = \text{diag}(\rho_{o,1}, \rho_{o,2})$, and $\text{sat}(\boldsymbol{\mu}/\epsilon_o) = [\text{sat}(\mu_1/\epsilon_o)\ \text{sat}(\mu_2/\epsilon_o)]^{\mathrm{T}}$. An optional PCH layer can be added to the outer loop so that the command vector $\mathbf{q}_h$ in Eqn. (5.26) and in the sliding variable $\boldsymbol{\mu}$ is the output of the outer loop PCH layer according to Eqn. (3.41).

Alternatively, in hover and low speed flight, the outer loop state, output, and command vectors become $\mathbf{z} \equiv [V_l \; V_h]^{\mathrm{T}}$, $\mathbf{w} \equiv [V_l \; V_h]^{\mathrm{T}}$, and $\mathbf{q} \equiv [V_{l,c} \; V_{h,c}]^{\mathrm{T}}$, respectively, while the control vector $\mathbf{r}_1$ is identical. The hover/low speed SMC law can be easily synthesized analogous to Eqn. (5.26), and is therefore omitted for brevity.

The transition point between forward flight and low speed is 23 m/s corresponding to the 45 kts threshold in ADS-33. However, the transition between the two sets of lateral-directional SMC laws can be a challenge due to the presence of integrators. To avoid instabilities and to ensure a smooth transition, the integrators in the lateral-directional control laws are reset at each transition point crossing such that their outputs match the current state values.

5.5 Yaw/Normal Rate Command Using Kinematics

To complete the control design, $\mathbf{r}_2 \equiv [w_c \; r_c]^{\mathrm{T}}$ remains to be computed. These commands are readily obtained using algebraic manupulations of their respective kinematic relationships in forward flight and low speed/hover. This obviates the need for a separate SMC loop.

In the yaw axis, a yaw rate command (r_c) in turning forward flight is generated internally for executing a steady, coordinated turn. This yaw rate command ensures that the helicopter's heading is sufficiently aligned with the ground track angle and sideslip remains small. From [101], when the helicopter is in a steady turn about an Earth-referenced vertical axis with a turn rate $\dot{\psi}$, the yaw angular rate about the body axis is:

$$r = \dot{\psi} \cos\theta \cos\phi, \tag{5.27}$$

and the bank angle is related to the turn rate as:

$$\tan\phi = \frac{\dot{\psi} V_h}{g}. \tag{5.28}$$

Eliminating turn rate, the yaw rate command is obtained as:

$$r_c = \frac{g \sin\phi \cos\theta}{V_h}. \tag{5.29}$$

In straight, level forward flight, the commanded yaw rate is simply $r_c = 0$. Alternatively, in hover and low speed flight, the yaw rate can be approximated to the rate of heading change. To effectuate a required heading change, a constant yaw rate magnitude can be commanded for the time required to execute the heading change.

In the vertical axis, an inertial vertical speed command ($V_{z,c}$) that is issued by the guidance loop can be transformed into a proportional normal speed command (w_c) using the transformation matrix $\mathbf{T}_{\mathrm{be}}$. Assuming small sideslip in a coordinated turn, the inertial vertical speed can be expressed as:

$$V_{z,c} = -u \sin\theta + w \cos\theta \cos\phi \tag{5.30}$$

Using the actual values of the longitudinal speed, pitch and roll attitudes, the commanded normal speed is obtained as:

$$w_c = \frac{u \sin\theta + V_{z,c}}{\cos\theta \cos\phi} \tag{5.31}$$

5.6 Two-Loop Stability Analysis and Controller Implementation

Although the continuous SMC laws ease controller implementation, further analysis is needed on the overall stability and tracking performance of the two-loop controller, as discussed in [42, 40]. From Eqn. (3.9), the inner loop sliding variable dynamics can be written as:

$$\dot{\boldsymbol{\sigma}} = (0.5\mathbf{I} - \boldsymbol{\rho}/\epsilon)\boldsymbol{\sigma} + \mathbf{S}\tilde{\mathbf{f}} \tag{5.32}$$

The stability of the inner loop continuous SMC can be proved using the Lyapunov analysis in Eqn. (3.15). If the inner loop sliding variable $\boldsymbol{\sigma}$ lies outside the boundary layer, then it is attracted and remains uniformly bounded to $\|\boldsymbol{\sigma}\| < \epsilon$, where the reaching time is given by Eqn. (3.12). From this result, the inner loop output tracking performance can be shown to be bounded to a region that is a function of the inner loop boundary layer size as $\|\dot{\mathbf{x}}_1\| < \Lambda(\epsilon)$. Furthermore, asymptotic tracking performance is achieved if $\|\mathbf{S}\tilde{\mathbf{f}}\| \rightarrow$ constant [42].

When ideal inner loop sliding motion does not occur (i.e. $\boldsymbol{\sigma} \neq 0$), Eqn. (5.17) is modified to:

$$\dot{\mathbf{x}}_1 = (\tilde{\mathbf{A}}_{11} - \tilde{\mathbf{A}}_{12}\mathbf{S}_2^{-1}\mathbf{S}_1)\mathbf{x}_1 + \tilde{\mathbf{A}}_{12}\mathbf{S}_2^{-1}\boldsymbol{\sigma} - \mathbf{T}_1\mathbf{r} \tag{5.33}$$

The inner loop controller tracks the outer loop SMC commands with an error $\dot{\mathbf{x}}_e = \mathbf{y} - \mathbf{r}$. The true outer loop sliding variable dynamics $(\boldsymbol{\mu})$ must therefore account for this tracking error in the form of the actual output, $\mathbf{y} = \dot{\mathbf{x}}_e + \mathbf{r}$. Furthermore, since only pitch and roll tracking errors from the inner loop are transferred to the outer loop, the subset of the output vector that influences the outer loop dynamics is $\mathbf{y}_1 = \mathbf{M}\dot{\mathbf{x}}_1 + \mathbf{r}_1$, where $\mathbf{y}_1 \equiv [\phi\ \theta]$ and $\mathbf{M} \in \mathbb{R}^{2\times 6}$. The true outer loop sliding dynamics can be obtained analogous to Eqn. (3.9) as:

$$\dot{\boldsymbol{\mu}} = (0.5\mathbf{I} - \boldsymbol{\rho}_o/\epsilon_o)\boldsymbol{\mu} + \mathbf{R}_2\mathbf{G}\mathbf{M}\dot{\mathbf{x}}_1 + \mathbf{R}\tilde{\mathbf{d}} \tag{5.34}$$

The Lyapunov function for the outer loop using the continuous SMC form can be expressed as:

$$\dot{V}_o \leqslant -2\|\boldsymbol{\mu}\|(\boldsymbol{\rho}_o\|\boldsymbol{\mu}\|/\epsilon_o - \|\mathbf{R}_2\mathbf{G}\mathbf{M}\|\|\dot{\mathbf{x}}_1\| - \|\mathbf{R}\tilde{\mathbf{d}}\|) \tag{5.35}$$

For negative definiteness of its derivative, requiring $\dot{V}_o \leqslant -2\|\boldsymbol{\mu}\|\gamma_o$ and $\gamma_o > 0$ yields $\|\boldsymbol{\mu}\| \leqslant \boldsymbol{\rho}_o^{-1}\epsilon_o(\gamma_o + \|\mathbf{R}_2\mathbf{G}\mathbf{M}\|\|\dot{\mathbf{x}}_1\| + \|\mathbf{R}\tilde{\mathbf{d}}\|)$. As $\|\dot{\mathbf{x}}_1\|$ is bounded, it implies that the outer loop sliding variable $\boldsymbol{\mu}$, and consequently the translational rate tracking error $\dot{\mathbf{z}}_e$, are both uniformly bounded. Using Eqn. (5.25) and the fact that $\dot{\mathbf{z}}_e = \mathbf{w} - \mathbf{q} = \mathbf{H}\mathbf{z} - \mathbf{q}$, the outer loop tracking error can be expressed in terms of the outer loop sliding variable as:

$$\dot{\mathbf{z}}_e = \mathbf{H}\mathbf{R}_2^{-1}\boldsymbol{\mu} - \mathbf{H}\mathbf{R}_2^{-1}\mathbf{R}_1\mathbf{z}_e - \mathbf{q} \tag{5.36}$$

It is clear that the output tracking performance depends on the choice of the boundary layer sizes and the SMC gains. In the outer loop, $\boldsymbol{\rho}_o$ should be sufficiently large to overcome uncertainties and ϵ_o should be sufficiently small to constrain $\boldsymbol{\mu}$ to a smaller bound, and yet avoid chattering. Moreover, to avoid overwhelming the outer loop dynamics with inner loop tracking error $\dot{\mathbf{x}}_e$, $\boldsymbol{\rho}$ should be large and ϵ should be small. Ideally, the inner loop should achieve its commanded values at a much faster rate and thereby ensure adequate time-scale separation with the outer loop. For this reason, in addition to the choice of the ideal system parameters in Table 5.1, $\boldsymbol{\rho}$ is set much higher than $\boldsymbol{\rho}_o$.

For controller implementation, offline simulations were performed in different operational conditions within the flight envelope of interest to determine the values of the SMC gains and the boundary layer sizes. The final SMC gains applied to the closed-loop controller are as follows: $\rho_\theta = 1.5$, $\rho_\phi = 2$, $\rho_r = 1$, $\rho_w = 1$, $\rho_\chi = 0.2$, and $\rho_{Vh} = \rho_{Vl} = 0.5$. Boundary layer sizes of $\epsilon_o = \epsilon = 0.2$ were found to provide adequate robustness while nearly avoiding chattering effects.

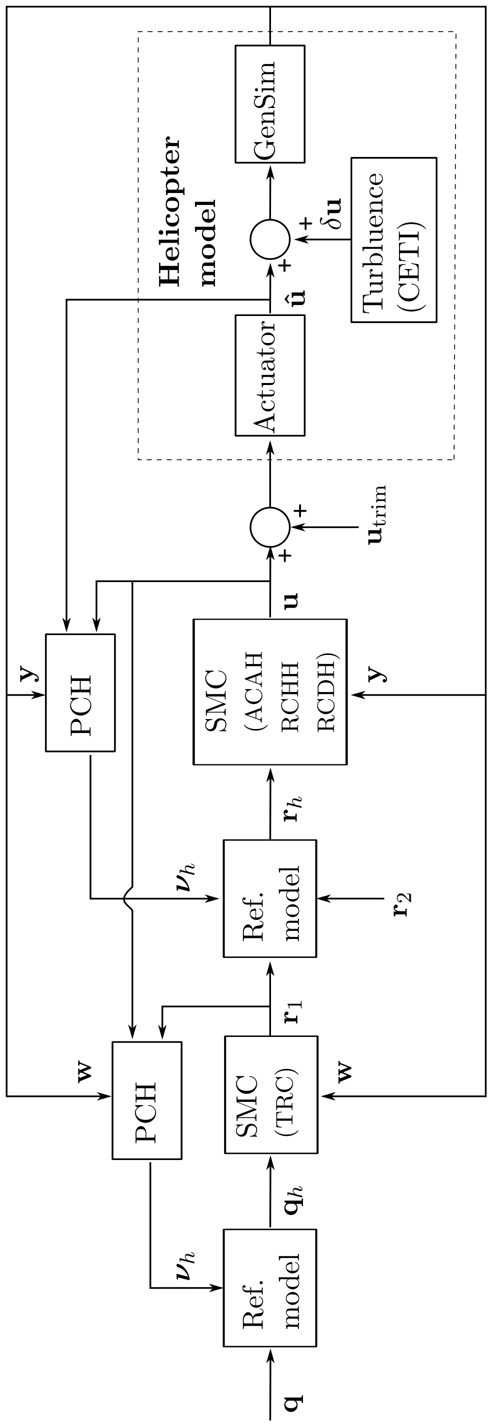

Figure 5.3: Closed-loop simulation environment using SMC and PCH

Fig. 5.3 illustrates the controller implementation as part of the closed-loop flight simulation environment. It consists of a two-loop SMC structure with an optional PCH layer in each loop. The outer loop receives guidance commands $\mathbf{q}$ and generates a virtual control signal $\mathbf{r}_1$ for the inner loop. The inner loop receives $\mathbf{r}_1$ and $\mathbf{r}_2$ via an optional PCH layer. The inner loop then generates collective, cyclic, and pedal commands, which are added to their respective trim values. These control commands are expressed as a percentage of their absolute displacement, where 0 % represents collective stick down, longitudinal cyclic stick aft, lateral cyclic stick left, and maximum left pedal. These control commands drive the main and tail rotor swashplate actuators and, together with CETI turbulence filters, form the inputs to the helicopter plant.

5.7 Comparison with an Explicit Model-Following Control Design

In contrast to SMC, the explicit model-following (EMF) control design approach relies on a full, well-identified linear model to synthesize feedforward control laws. For the purpose of comparative evaluation, EMF-based attitude and rate control laws are developed in this section based on the work of [15]. It is noted that the EMF approach has been evaluated on many contemporary helicopter platforms [15, 16, 102]. Synthesis of EMF-based translational rate command control laws and their comparison with the SMC-based translational rate command laws are, however, beyond the scope of this thesis.

First, the directly controlled states are separated from the Euler angles to obtain a reduced dimensional linear system as:

$$\dot{\bar{\mathbf{x}}}(t) = \mathbf{A}_{22}\bar{\mathbf{x}}(t) + \mathbf{B}_2\mathbf{u}(t) + \mathbf{f}_2(\bar{\mathbf{x}}, \mathbf{u}, t) \tag{5.37}$$

where $\bar{\mathbf{x}} \equiv [w\ p\ q\ r]^{\mathrm{T}}$ and $\mathbf{u}$ as before. In contrast to the SMC synthesis, both $\mathbf{A}_{22}$ and $\mathbf{B}_2$ in Eqn. (5.37) now contain all axial and cross-coupling stability and control derivatives.

Furthermore, the availability of full state feedback is assumed. To satisfy the required response types Eqns. (5.1)–(5.4), model states are obtained from commanded states as follows:

$$\begin{aligned} w_m &= \frac{\lambda_w}{s+\lambda_w} w_c && (5.38) \\ r_m &= \frac{\lambda_r}{s+\lambda_r} r_c && (5.39) \\ \phi_m &= \frac{\omega_\phi^2}{s^2+2\zeta_\phi\omega_\phi s+\omega_\phi^2} \phi_c && (5.40) \\ \theta_m &= \frac{\omega_\theta^2}{s^2+2\zeta_\theta\omega_\theta s+\omega_\theta^2} \theta_c && (5.41) \end{aligned}$$

The remaining model states are obtained using the kinematic relationships between the Euler angular rates and the body angular rates as follows:

$$\begin{aligned} \dot{\psi}_m &= (r_m + \dot{\theta}_m \sin\phi_m)/(\cos\theta_m \cos\phi_m) && (5.42) \\ p_m &= \dot{\phi}_m - \dot{\psi}_m \sin\theta_m && (5.43) \\ q_m &= \dot{\theta}_m \cos\phi_m + \dot{\psi}_m \cos\theta_m \sin\phi_m && (5.44) \end{aligned}$$

Note that Eqns. (5.38)–(5.41) also yield $\dot{w}_m$, $\dot{r}_m$, $\dot{\phi}_m$, and $\dot{\theta}_m$, respectively, which are required in Eqns. (5.42)–(5.44). The first derivatives of p_m and q_m are computed by numerical differentiation. The required feedforward control inputs that satisfy the command model states, $\bar{\mathbf{x}}_m \equiv [w_m \; p_m \; q_m \; r_m]^{\mathrm{T}}$ are then obtained by inverting the nominal linear model as follows:

$$\mathbf{u}_{ff} = \mathbf{B}_2^{-1}(\dot{\bar{\mathbf{x}}}_m - \mathbf{A}_{22}\bar{\mathbf{x}}_m) \qquad (5.45)$$

where $\mathbf{B}_2$ is known to be square and invertible. In obtaining Eqn. (5.45), the first derivatives of the command model states are computed by numerical differentiation. A feedback stabilization control component is computed using the command model states

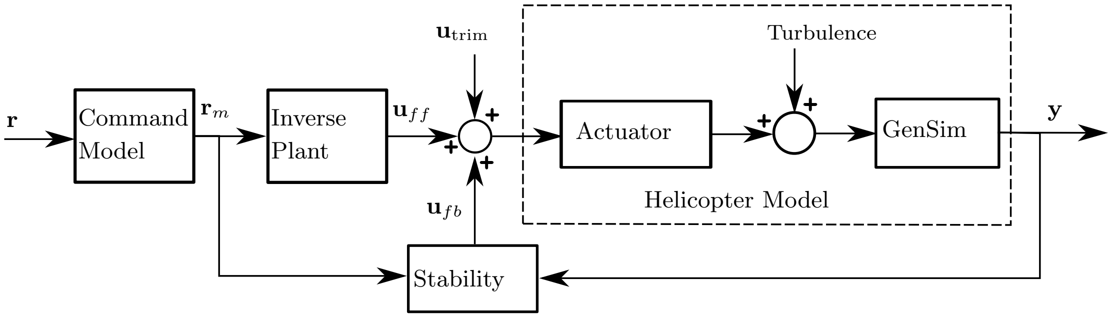

Figure 5.4: Closed-loop simulation of an EMF attitude/rate controller

and measured states as follows:

$$\mathbf{u}_{fb} = \begin{bmatrix} G_w(w_m - w) \\ G_\phi(\phi_m - \phi) + G_p(p_m - p) \\ G_\theta(\theta_m - \theta) + G_q(q_m - q) \\ G_r(r_m - r) \end{bmatrix} \tag{5.46}$$

where $G_{(\cdot)}$ are tunable feedback gains. Eqn. (5.46) seeks to stabilize the system Eqn. (5.37) in the presence of $\mathbf{f}_2$ that includes turbulence, unmodeled dynamics, and any unstable modes that may be excited by the feedforward component. Finally, using Eqn. (5.45) and Eqn. (5.46), the cumulative control applied to the plant is:

$$\mathbf{u} = \mathbf{u}_{ff} + \mathbf{u}_{fb} \tag{5.47}$$

Fig. 5.4 illustrates the closed-loop implementation of the EMF attitude, yaw rate and vertical rate controller. The commanded states are passed through the command model and then inverted to obtain the feedforward control component $\mathbf{u}_{ff}$. $\mathbf{u}_{ff}$ and the stability feedback control component $\mathbf{u}_{fb}$ together form the control input that is then superimposed over the trim control.

It is noted that EMF does not explicitly offer robustness to $\mathbf{f}_2$. Nevertheless, the EMF feedback gains must be carefully tuned for acceptable system performance. On the one hand, $G_{(\cdot)}$ should be sufficient to stabilize the system against uncertainties; on the other hand, large $G_{(\cdot)}$ will tend to excite the high frequency rotor fuselage coupled modes, which may affect stability or produce oscillatory responses. Based on offline simulations, the following values are found to be acceptable: $[G_w \; G_\phi \; G_p \; G_\theta \; G_q \; G_r]$ = $[0.1 \; 0.5 \; 0.04 \; 0.4 \; 0.04 \; 0.25]$.

6 Online Waypoint Trajectory Generation

`This chapter is based on the following journal publication:`

[J1] O. Halbe and M. Hajek, "Online Waypoint Trajectory Generation Using State-Dependent Riccati Equation," *Journal of Guidance, Control, and Dynamics*, vol. 42, no. 12, pp. 2687–2693, 2019.

THIS chapter describes the development of SDRE-based suboptimal guidance control laws following the steps outlined in Sec. 3.2. This aim is to demonstrate for a full-scale helicopter flight model automatic flight path vector generation and tracking between waypoints with constraints on the flight path vector at each waypoint.

6.1 Trajectory Generation Problem Definition

Consider the scenario depicted in Fig. 6.1. The local reference frame originates at the rotorcraft's center of gravity. The Z-axis (local vertical) points vertically up, the X-axis (local horizontal) is rotated from North about the Z-axis to align with the rotorcraft's heading, and the Y-axis (local lateral) points port side. Sideslip has been neglected. The rotorcraft is in trimmed forward flight at present position (x, y, z) with velocity vector (V_h, V_z, χ). The final states at the next waypoint are denoted by $(V_{h,t}, V_{z,t}, \chi_t)$, which are assumed to be computed using an appropriate path planner, such as [49]. The

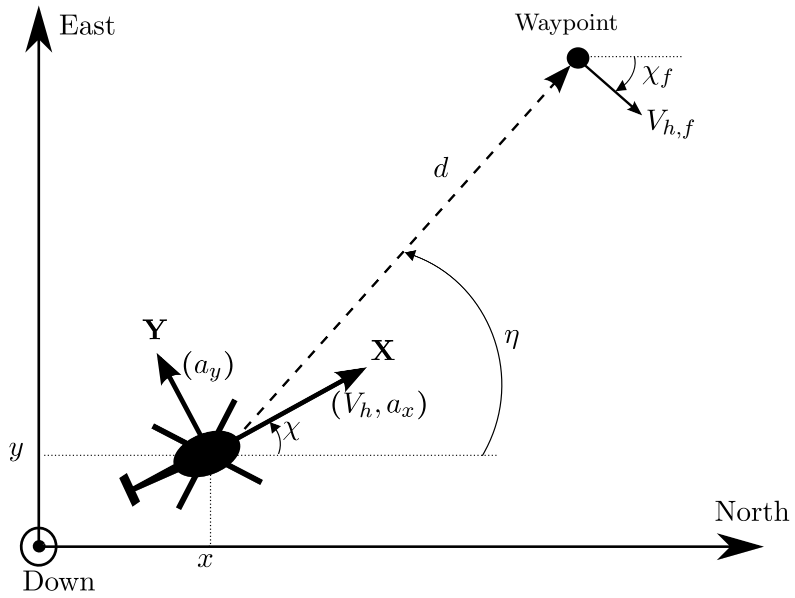

(a) Lateral geometry

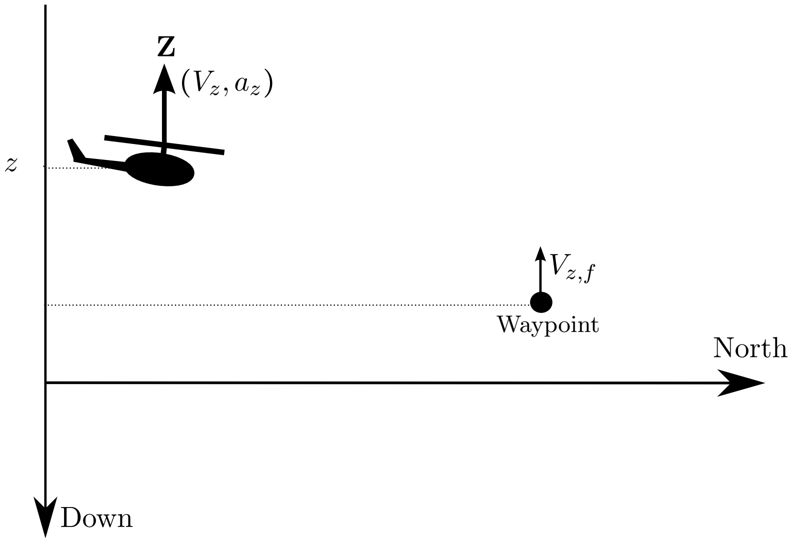

(b) Vertical geometry

Figure 6.1: Waypoint trajectory generation geometry

kinematics using a point mass model are:

$$\textbf{Horizontal Axis} \quad \begin{cases} \dot{d} = -V_h \cos(\chi - \eta) \\ \dot{V}_h = a_x \end{cases} \tag{6.1}$$

$$\textbf{Lateral Axis} \quad \begin{cases} \dot{\eta} = \frac{V_h}{d} \sin(\chi - \eta) \\ \dot{\chi} = \frac{a_y}{V_h} \end{cases} \tag{6.2}$$

$$\textbf{Vertical Axis} \quad \begin{cases} \dot{z} = V_z \\ \dot{V}_z = a_z \; - \; g \end{cases} \tag{6.3}$$

The necessary conditions for successful tracking of waypoint coordinates and velocity vector are:

- Lateral Axis: $\eta \rightarrow \chi_t$ and $\chi \rightarrow \chi_t$ for horizontal position and ground track;
- Vertical Axis: $z \rightarrow z_t$ for altitude and $V_z \rightarrow V_{z,t}$ for vertical velocity;
- Horizontal Axis: $V_h \rightarrow V_{h,t}$ for horizontal velocity.

Note that lateral axis objectives imply $\chi - \eta \rightarrow 0$, which from Eqn. (6.1) will ensure $\dot{d} \rightarrow -V_h$, and therefore $d \rightarrow 0$ for $V_h > 0$. Defining the state vector $\mathbf{X} = [V_h \; V_z \; \chi \; \eta \; z]^T$ and the control vector $\mathbf{U} = [a_x \; a_y \; a_z]^T$, the trajectory generation problem essentially becomes a problem of state tracking. Control limits in terms of the maximum values of the forward, lateral and vertical acceleration are not explicitly considered in the problem formulation. Rather, these limits are enforced during implementation using rate limiters and saturation blocks at the output of the guidance command generation.

6.2 Translational Acceleration Command Generation

As shown in Section 3.2, the SDRE nonlinear regulator is ideally suited for a nonlinear control-affine system of the form $\dot{\mathbf{x}} = \mathbf{F}(\mathbf{x}) + \mathbf{B}(\mathbf{x})\mathbf{u}$. Note that the system of Eqns. (6.1)–(6.3) is affine in control. In SDRE, a linear-like structure with state dependent coefficients (SDC) is first obtained by direct parameterization as $\dot{\mathbf{x}} = \mathbf{A}(\mathbf{x})\mathbf{x} + \mathbf{B}(\mathbf{x})\mathbf{u}$. The algebraic Riccati equation is then solved to obtain the nonlinear feedback control law [82]. The SDRE control solution of a multivariable system is suboptimal, and converges to its optimal solution as the states are driven to zero [84]. SDRE has been successfully applied to several probems, including helicopter flight control [85] and impact angle constrained missile guidance [87]. The reader is referred to [84], which surveys a wide spectrum of aerospace control applications using SDRE. In the present work, the state tracking problem in each axis is decoupled under the condition that dynamic effects in any axis, due to control inputs in another axis in a single time step, are small. This approach leads to the formulation of three independent infinite-horizon nonlinear regulators. Axis decoupling serves two purposes. First, it simplifies the parameterization of the state-dependent coefficients, which plays a key role in recovering the optimal control solution. Second, the algebraic Riccati equations are solved analytically to guarantee deterministic control solutions in finite-time, as opposed to iterative numerical methods for the general multivariable case [103]. It will be shown in Sec. 8 that a trajectory tracking flight controller with cross-coupling compensation can overcome any impact of acceleration decoupling on control performance.

6.2.1 Lateral Acceleration Control Law

The state tracking errors in the lateral axis are given by $e_\chi = \chi - \chi_t$ and $e_\eta = \eta - \chi_t$. With $(\chi - \eta) \equiv (e_\chi - e_\eta)$, Eqn. (6.2) is parameterized for e_η and e_χ, and written in nonlinear SDC form as:

$$\begin{bmatrix} \dot{e}_\eta \\ \dot{e}_\chi \end{bmatrix} = \begin{bmatrix} -\frac{V_h \sin(e_\chi - e_\eta)}{d(e_\chi - e_\eta)} & \frac{V_h \sin(e_\chi - e_\eta)}{d(e_\chi - e_\eta)} \\ 0 & 0 \end{bmatrix} \begin{bmatrix} e_\eta \\ e_\chi \end{bmatrix} + \begin{bmatrix} 0 \\ \frac{1}{V_h} \end{bmatrix} a_y \tag{6.4}$$

with $\mathbf{x} = [e_\eta \;\; e_\chi]^{\mathrm{T}}$ and $\mathbf{u} = [a_y]$. $\mathbf{B}(\mathbf{x}) \neq \mathbf{0}$ for $V_h > 0$. The SDRE necessary conditions are recalled from [82] as: 1) $\{\mathbf{A}, \mathbf{B}\}$ is controllable; 2) $\mathbf{F}(\mathbf{x})$ is continuously differentiable; and 3) $\mathbf{F}(\mathbf{0})$ goes through the origin. To verify the first condition, the rank of the controllability matrix $\mathbf{M}(\mathbf{x})$ is found using:

$$|\mathbf{M}(\mathbf{x})| = |\{\mathbf{B}(\mathbf{x}),\; \mathbf{A}(\mathbf{x})\mathbf{B}(\mathbf{x})\}| = \begin{vmatrix} 0 & \frac{\sin(e_\chi - e_\eta)}{d(e_\chi - e_\eta)} \\ \frac{1}{V_h} & 0 \end{vmatrix} = -\frac{\sin(e_\chi - e_\eta)}{ur(e_\chi - e_\eta)} \neq 0$$

except for $\chi - \eta = \pi$. In Fig. 6.1, this condition occurs when the rotorcraft flies along the horizontal line of sight but radially away from the next waypoint. This point is considered outside the domain of operation, and the system is therefore controllable at all points of interest. The differentiability condition and initial condition are satisfied as follows:

$$\mathbf{F}(\mathbf{x}) = \begin{bmatrix} \frac{V_h}{d}\sin(e_\chi - e_\eta) \\ 0 \end{bmatrix} \in C^1 \quad \text{and} \quad \mathbf{F}(\mathbf{0}) = \begin{bmatrix} V_h \sin(0) \\ 0 \end{bmatrix} = \begin{bmatrix} 0 \\ 0 \end{bmatrix}$$

Consider the following infinite horizon quadratic cost function to be minimized.

$$J = \frac{1}{2}\int_{t_0}^{\infty} [\mathbf{x^T Q x} + \mathbf{u^T R u}]\, dt \tag{6.5}$$

The weighting elements for the present problem are chosen as $\mathbf{Q} = \text{diag}(q_1^2, q_2^2) > 0$ and $\mathbf{R} = [1]$. The feedback control law is obtained by solving the algebraic Riccati equation for the unique, symmetric and positive-definite matrix $\mathbf{P(x)}$ [82].

$$\mathbf{A^T(x)P(x) + P(x)A(x) - P(x)B(x)R^{-1}B^T(x)P(x) + Q = 0} \tag{6.6}$$

Upon substitution, one obtains:

$$\begin{bmatrix} -\frac{V_h \sin(e_\chi - e_\eta)}{d(e_\chi - e_\eta)} & 0 \\ \frac{V_h \sin(e_\chi - e_\eta)}{d(e_\chi - e_\eta)} & 0 \end{bmatrix} \begin{bmatrix} p_{11} & p_{12} \\ p_{12} & p_{22} \end{bmatrix} + \begin{bmatrix} p_{11} & p_{12} \\ p_{12} & p_{22} \end{bmatrix} \begin{bmatrix} -\frac{V_h \sin(e_\chi - e_\eta)}{d(e_\chi - e_\eta)} & \frac{V_h \sin(e_\chi - e_\eta)}{d(e_\chi - e_\eta)} \\ 0 & 0 \end{bmatrix}$$
$$- \begin{bmatrix} p_{11} & p_{12} \\ p_{12} & p_{22} \end{bmatrix} \begin{bmatrix} 0 \\ \frac{1}{V_h} \end{bmatrix} [1] \begin{bmatrix} 0 & \frac{1}{V_h} \end{bmatrix} \begin{bmatrix} p_{11} & p_{12} \\ p_{12} & p_{22} \end{bmatrix} + \begin{bmatrix} q_1^2 & 0 \\ 0 & q_2^2 \end{bmatrix} = 0$$

This yields three simultaneous algebraic equations in p_{11}, p_{12} and p_{22}. Denoting $\xi \equiv \frac{V_h \sin(e_\chi - e_\eta)}{d(e_\chi - e_\eta)}$, the system of equations is solved analytically to obtain:

$$\begin{aligned} p_{22} &= -\xi V_h^2 \pm V_h \sqrt{\xi^2 u^2 + 2\xi V_h \sqrt{q_1^2 + q_2^2} + q_2^2} \\ p_{12} &= V_h \sqrt{q_1^2 + q_2^2} - p_{22} \end{aligned}$$

Since $\{\mathbf{A}, \mathbf{B}\}$ is controllable, the existence of a positive definite solution of $\mathbf{P}(\mathbf{x})$, which also gives the optimal control solution for the system, is guaranteed [84]. Clearly, p_{22} has two real roots, one positive and one negative. Note that p_{11} does not need to be explicitly computed as it does not appear in the final control law of Eqn. (6.7). Using the positive root of p_{22}, the closed form lateral acceleration control law is obtained from the solution of the algebraic Riccati Eqn. (6.6) as $a_y^* = -R^{-1}\mathbf{B}(\mathbf{x})^{\mathrm{T}}\mathbf{P}(\mathbf{x})\mathbf{x}$, according to [82].

$$\begin{aligned} a_y^* &= -\frac{p_{12}(\eta - \chi_t)}{V_h} - \frac{p_{22}(\chi - \chi_t)}{V_h} \\ &= -\Big[\xi V_h - \sqrt{\xi^2 u^2 + 2\xi V_h \sqrt{q_1^2 + q_2^2} + q_2^2} + \sqrt{q_1^2 + q_2^2}\,\Big](\eta - \chi_t) \\ &\quad -\Big[-\xi V_h + \sqrt{\xi^2 u^2 + 2\xi V_h \sqrt{q_1^2 + q_2^2} + q_2^2}\Big](\chi - \chi_t) \end{aligned} \tag{6.7}$$

6.2.2 Vertical and Forward Acceleration Control Laws

To simplify the vertical axis tracking, consider $V_{z,t} = 0$. The altitude tracking error is $e_z = z - z_t$, and from Eqn. (6.3), $\dot{e}_z = \dot{z} = V_z$. $\dot{V}_z$ is also given by Eqn. (6.3). To satisfy SDRE conditions at the origin, the gravity term is removed from the formulation and added directly to the final control law. The vertical axis equations are parameterized and written in matrix form as:

$$\begin{bmatrix} \dot{e}_z \\ \dot{V}_z \end{bmatrix} = \begin{bmatrix} 0 & 1 \\ 0 & 0 \end{bmatrix} \begin{bmatrix} e_z \\ V_z \end{bmatrix} + \begin{bmatrix} 0 \\ 1 \end{bmatrix} a_z \tag{6.8}$$

$\mathbf{x} = [e_z \;\; V_z]^{\mathrm{T}}$ and $\mathbf{u} = [a_z]$. $\mathbf{B}(\mathbf{x}) \neq 0$. The controllability matrix $\mathbf{M}(\mathbf{x})$ has full rank, since:

$$|\mathbf{M}(\mathbf{x})| = |\{\mathbf{B}(\mathbf{x}),\ \mathbf{A}(\mathbf{x})\mathbf{B}(\mathbf{x})\}| = \begin{vmatrix} 0 & 1 \\ 1 & 0 \end{vmatrix} = -1 \neq 0$$

The system is thus controllable. The differentiability condition and initial condition are also satisfied:

$$\mathbf{F}(\mathbf{x}) = \begin{bmatrix} V_z \\ 0 \end{bmatrix} \in C^1 \quad \text{and} \quad \mathbf{F}(\mathbf{0}) = \begin{bmatrix} 0 \\ 0 \end{bmatrix}$$

Using the cost function of Eqn. (6.5), with $\mathbf{Q} = \text{diag}(q_1^2, q_2^2) > 0$ and $\mathbf{R} = [1]$, the algebraic Riccati Eqn. (6.6) in the vertical axis is obtained as:

$$\begin{aligned} &\begin{bmatrix} 0 & 0 \\ 1 & 0 \end{bmatrix}\begin{bmatrix} p_{11} & p_{12} \\ p_{12} & p_{22} \end{bmatrix} + \begin{bmatrix} p_{11} & p_{12} \\ p_{12} & p_{22} \end{bmatrix}\begin{bmatrix} 0 & 1 \\ 0 & 0 \end{bmatrix} \\ -&\begin{bmatrix} p_{11} & p_{12} \\ p_{12} & p_{22} \end{bmatrix}\begin{bmatrix} 0 \\ 1 \end{bmatrix}[1]\begin{bmatrix} 0 & 1 \end{bmatrix}\begin{bmatrix} p_{11} & p_{12} \\ p_{12} & p_{22} \end{bmatrix} + \begin{bmatrix} q_1^2 & 0 \\ 0 & q_2^2 \end{bmatrix} = 0 \end{aligned} \tag{6.9}$$

The analytical solutions using the positive roots of p_{12} and p_{22} are:

$$\begin{aligned} p_{12} &= q_1 \\ p_{22} &= \sqrt{2q_1 + q_2^2} \end{aligned}$$

The closed-form vertical acceleration control law is obtained using $a_z^* = -R^{-1}\mathbf{B}^{\mathrm{T}}\mathbf{P}\mathbf{x}$, and is compensated with the gravity term.

$$a_z^* = -\left[q_1(z - z_t) + V_z\sqrt{2q_1 + q_2^2}\right] + g \tag{6.10}$$

Eqn. (6.10) can be extended to $V_{z,t} \neq 0$ by modifying its second term such that it vanishes at $V_z = V_{z,t}$. Eqn. (6.10) becomes:

$$a_z^* = -\left[q_1(z - z_t) + (V_z - V_{z,t})\sqrt{2q_1 + q_2^2}\right] + g \tag{6.11}$$

For the forward acceleration, it is recalled that $d \to 0$ is satisfied by the lateral acceleration control law. Therefore, it only remains to regulate $e_{V_h} = (V_h - V_{h,t}) \to 0$ using a_x, as $d \to 0$. The derivation of a_x is trivial, because $\dot{e}_{V_h} = \dot{V}_h$ from Eqn. (6.1) is scalar, linear in control, and without state dependencies. For $\mathbf{R} = [1]$ and $\mathbf{Q} = [q^2]$, the closed-form forward acceleration becomes:

$$a_x^* = -q(V_h - V_{h,t}) \tag{6.12}$$

6.2.3 Waypoint Spacing Analysis

The closed-form acceleration control laws operate without reference trajectories between waypoints. However, successful convergence to the terminal constraints depends on the rotorcraft's performance limits, the horizontal and vertical distances to the waypoint, and the chosen SDRE weights. To ensure convergence, it is proposed to identify the limiting horizontal and vertical distances to the velocity vector constrained waypoint. First, to satisfy $\chi \to \chi_t$, d_χ is parameterized in terms of the rotorcraft's minimum turn radius as $d_\chi > \Gamma\ R_{\min}$. For a conventional helicopter configuration in a steady, level turn and low sideslip, $R_{\min} = \frac{V_h^2}{g \tan \phi_{\max}}$. For the variable horizontal velocity case, $\max(V_h, V_{h,t})$ is used in the numerator. $\Gamma > 0$ is determined by closed-loop simulations, using values of the pair $\{\chi, \chi_t\}$ that represent all combinations of the four quadrants. Note that the Dubins long path, which consists of a curved path, a straight line, and another curved path sequentially, is defined for $\Gamma \geqslant 4$ [104]. Next, to satisfy $(V_h \to V_{h,t})$, d_{V_h} is estimated using the maximum forward acceleration as $d_{V_h} > \frac{|V_h^2 - V_{h,t}^2|}{2|a_{x_{\max}}|}$. This value is conservative, because the actual along-track distance in a turning flight will be greater than the straight-line distance between waypoints. Thus, the minimum horizontal waypoint separation is obtained as $\max(d_\chi, d_{V_h})$. Finally, the achievable d_z can be estimated using the maximum vertical acceleration from level flight as $d_z < 0.5|a_{z_{\max}}|t_{\text{go}}^2$, where t_{go} for $\max(d_\chi, d_{V_h})$ is approximated by Eqn.(6.14) in the following section.

6.3 Design Parameters and Implementation Aspects

The choice of the SDRE weighting factors determines the evolution of the trajectory between waypoints. The state regulation error at the start of the trajectory is typically large, which may result in a large control demand leading to control saturation. Since $\mathbf{R} = [1]$ in each axis, choosing the diagonal elements of $\mathbf{Q}$ as inversely proportional to the time–to–go (i.e. the estimated time to reach the waypoint) ensures a smooth and gradually converging state trajectory, and reduces the likelihood of control saturation, as demonstrated in [87].

$$q_{(\cdot)} \quad = \quad \frac{N_{(\cdot)}}{t_{\text{go}}}$$

where $(\cdot)$ denotes any state tracking variable. The t_{go} is approximated at the k^{th} time step using the following approximations for the actual horizontal distance–to–go, horizontal velocity and forward acceleration.

$$\begin{aligned} \text{if} \quad t_{\text{go},(k)} \quad &\approx \quad \frac{-V_{h,(k-1)} + \sqrt{V_{h,(k-1)}^2 + 2a_{x_{(k-1)}} d_{(k-1)}}}{a_{x_{(k-1)}}} \quad \text{for} \quad a_{x_{(k-1)}} \neq 0, \qquad (6.13) \\ \text{else} \quad t_{\text{go}(k)} \quad &\approx \quad \frac{d_{(k-1)}}{V_{h,(k-1)}} \end{aligned}$$

Gain values $N_{(\cdot)}$ are selected such that the state tracking component and control component in the cost function Eqn. (6.5) have the same order of magnitude. Extremal values of state tracking errors, accelerations and time-to-go give the numerical range for gain selection. With this logic, the following gain values were found to satisfy tracking constraints while avoiding control saturation over a wide envelope: $N_\eta = 800$, $N_\chi = 200$; $N_z = 0.07$, $N_{V_z} = 0.05$; and $N_{V_h} = 1$.

For simulation purposes of the guidance law, forward flight conditions are used: $u \in [20, 60]$m/s, $w \in [-6, 6]$m/s. Moreover, obstacle-free paths are assumed. The acceleration commands are constrained by saturation blocks to the following limits:

$a_y \in [-10, 10]\text{m/s}^2$ corresponding to $|\Delta\phi_{\max}| = 45°$, $a_z \in [-0.5, 0.5]\text{m/s}^2$ corresponding to the available a_n margin at $|\Delta\phi_{\max}|$, and $a_x \in [-1.5, 1.5]\text{m/s}^2$ corresponding to $|\Delta\theta_{\max}| = 10°$.

7 Online Rendezvous Trajectory Generation

`This chapter is based on the following conference publication:`

[C5] O. Halbe and M. Hajek, “Online Rendezvous Guidance for Helicopter Using State Dependent Riccati Equation,” in *AIAA Scitech 2020 Forum (GNC Session)*, Orlando, FL, USA, January 2020, AIAA Paper 2020–1827.

THIS chapter applies the state-dependent Riccati equation (SDRE) technique for online rendezvous guidance to a moving target waypoint. For this purpose, the SDRE-based online guidance to a fixed waypoint described in Chapter 6 is extended to a mobile target scenario. A 3D rendezvous scenario of a helicopter with a slower maneuvering target is considered. The guidance objective is to intercept the 3D target position with zero relative velocity. Three independent, decoupled, nonlinear state regulation problems in each of the lateral, vertical and forward axes of motion are formulated using the SDRE technique [82]. The resulting algebraic Riccati equations are then solved analytically to obtain deterministic, closed-form, state-feedback guidance laws for the vehicle accelerations.

7.1 Trajectory Generation Problem Definition

Consider the scenario depicted in Fig. 7.1. The helicopter is in trimmed forward flight at present position (x, y, z) in the North-East-Down (NED) frame with track angle χ with respect to North. A local, vehicle-carried XYZ reference frame is obtained by rotating the NED frame about its vertical axis by an angle χ and translating it to the helicopter's center of gravity. The helicopter's horizontal velocity V_h lies along this local X-axis, and its vertical velocity V_z lies along the local Z-axis. Sideslip is neglected for the purpose of guidance command generation. Although helicopters exhibit nonzero sideslip in practice, most helicopter autopilots can effectively regulate sideslip and ensure turn coordination using an appropriate yaw rate command.

Consider a moving target of constant speed $V_t < V_h$, course angle χ_t with respect to North, and current position at (x_t, y_t, z_t) as shown in Fig. 7.1. The horizontal position error is $d = \sqrt{(x_t - x)^2 + (y_t - y)^2}$, the vertical position error is $z - z_t$, and the angle of the horizontal line of sight with respect to North is $\eta = \arctan((y_t - y)/(x_t - x))$. The

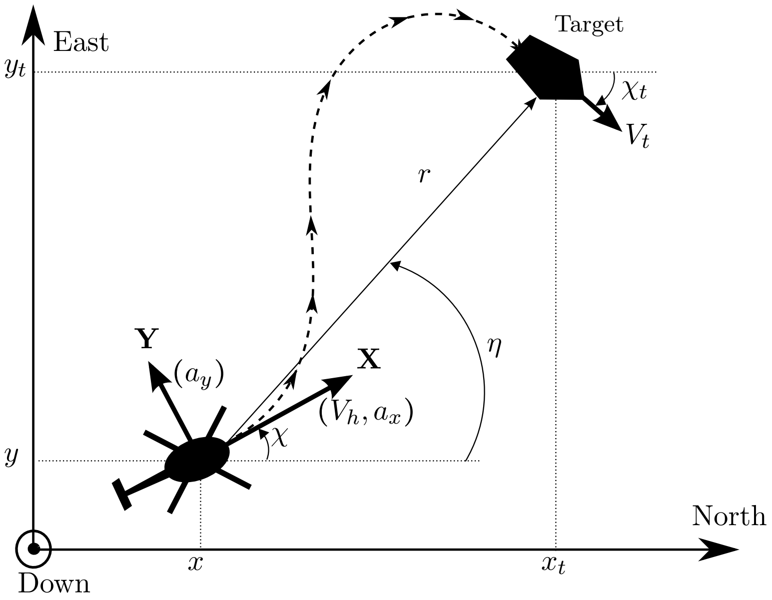

Figure 7.1: Helicopter-target rendezvous trajectory generation geometry

engagement kinematics are governed by the following equations:

$$\begin{aligned}
\dot{\eta} &= \frac{V_h}{d}\sin(\chi-\eta) - \frac{V_t}{d}\sin(\chi_t-\eta) && (7.1)\\
\dot{\chi} &= \frac{a_y}{V_h} && (7.2)\\
\dot{z} &= V_z && (7.3)\\
\dot{V}_z &= a_z - g && (7.4)\\
\dot{V}_h &= a_x && (7.5)
\end{aligned}$$

where a_x, a_y, and a_z are the helicopter's forward, lateral, and vertical accelerations, respectively, in the local frame. It can be noticed in Fig. 7.1 that the sufficient conditions for successful 3D rendezvous are:

1. $\eta \to \chi_t$ and $\chi \to \chi_t$,
2. $z \to z_t$ and $V_z \to 0$, and
3. $V_h \to V_t$

These conditions together will ensure that the helicopter reaches the target position with a velocity vector identical to that of the target. Defining the state tracking errors as $e_\eta = \eta - \chi_t$, $e_\chi = \chi - \chi_t$, $e_z = z - z_t$, $e_{V_z} = V_z$, and $e_{V_h} = V_h - V_t$, the rendezvous guidance problem can be posed as a nonlinear state regulation problem with the lateral, vertical, and forward accelerations as control variables. Analytical solutions for these accelerations are derived in the following section.

7.2 Translational Acceleration Command Generation

7.2.1 Lateral Acceleration Guidance Law

The state vector for regulating the horizontal position error is defined as $[e_\eta \; e_\chi]^{\mathrm{T}}$. The control variable is the lateral acceleration a_y. For a slow maneuvering target, $\dot{\chi}_t$ is much smaller than the helicopter heading rate $\dot{\chi}$. Therefore, $\dot{\chi}_t$ can be neglected and one obtains $\dot{e}_\eta = \dot{\eta}$ and $\dot{e}_\chi = \dot{\chi}$. Knowing that $(\chi - \eta) \equiv (e_\chi - e_\eta)$, Eqns. (7.1)-(7.2) followed by algebraic manipulations yield the following dynamic equation:

$$\dot{e}_\eta = \frac{V_h}{d} \sin(e_\chi - e_\eta) + \frac{V_t}{d} \sin(e_\eta) \tag{7.6}$$

which can be parameterized in terms of the states as follows:

$$\dot{e}_\eta = \frac{V_h \sin(e_\chi - e_\eta)}{d(e_\chi - e_\eta)} e_\chi - \frac{V_h \sin(e_\chi - e_\eta)}{d(e_\chi - e_\eta)} e_\eta + \frac{V_t \sin(e_\eta)}{d e_\eta} e_\eta \tag{7.7}$$

The lateral kinematics can be represented in nonlinear SDC form according to Eqn.(3.19), and written in matrix form as follows:

$$\begin{bmatrix} \dot{e}_\eta \\ \dot{e}_\chi \end{bmatrix} = \underbrace{\begin{bmatrix} (X - Y) & Y \\ 0 & 0 \end{bmatrix}}_{\mathbf{A(x)}} \begin{bmatrix} e_\eta \\ e_\chi \end{bmatrix} + \underbrace{\begin{bmatrix} 0 \\ 1/V_h \end{bmatrix}}_{\mathbf{B(x)}} a_y \tag{7.8}$$

where,

$$X = \frac{V_t \sin(e_\eta)}{d e_\eta} \tag{7.9}$$

$$Y = \frac{V_h \sin(e_\chi - e_\eta)}{d(e_\chi - e_\eta)} \tag{7.10}$$

Note that $\mathbf{B(x)} \neq \mathbf{0}$ for $V_h > 0$. The SDRE necessary conditions are recalled from [82] as: 1) The pair $\{\mathbf{A}, \mathbf{B}\}$ is controllable; 2) $\mathbf{f(x)}$ is continuously differentiable; and 3) $\mathbf{f(0)}$ goes through the origin. To verify the first condition, the rank of the controllability matrix $\mathbf{M(x)}$ is given by:

$$|\mathbf{M(x)}| = |\{\mathbf{B(x)},\ \mathbf{A(x)B(x)}\}| = \begin{vmatrix} 0 & \frac{Y}{V_h} \\ \frac{1}{V_h} & 0 \end{vmatrix} = -\frac{Y}{V_h^2} \neq 0$$

as $V_h > 0, d > 0$, and $\lim_{x\to 0} \frac{\sin x}{x} = 1$, except for the case $\chi - \eta = \pi$. This singular case is, however, considered outside the domain of interest. Furthermore, $\mathbf{f(x)} \in C^1$ and $\mathbf{f(0)} = 0$ are easily verified from Eqns. (7.8)–(7.10).

Using Eqn. (3.20), the quadratic cost function becomes:

$$\begin{aligned} \text{minimize} \quad J &= \frac{1}{2}\int_{t_0}^{\infty} [\mathbf{x^T Q x} + \mathbf{R} a_y^2]\, dt && (7.11) \\ \text{where} \quad \mathbf{Q} &= \begin{bmatrix} q_1^2 & 0 \\ 0 & q_2^2 \end{bmatrix} \quad \text{and} \quad \mathbf{R} = [1] \quad \text{are chosen.} \end{aligned}$$

Substituting the relevant terms from Eqn. (7.8) into the algebraic Riccati Eqn. (3.24), one obtains:

$$\begin{bmatrix} (X-Y) & 0 \\ Y & 0 \end{bmatrix}\begin{bmatrix} p_{11} & p_{12} \\ p_{12} & p_{22} \end{bmatrix} + \begin{bmatrix} p_{11} & p_{12} \\ p_{12} & p_{22} \end{bmatrix}\begin{bmatrix} (X-Y) & Y \\ 0 & 0 \end{bmatrix} - \begin{bmatrix} p_{11} & p_{12} \\ p_{12} & p_{22} \end{bmatrix}\begin{bmatrix} 0 \\ \frac{1}{V_h} \end{bmatrix}\begin{bmatrix} 0 & \frac{1}{V_h} \end{bmatrix}\begin{bmatrix} p_{11} & p_{12} \\ p_{12} & p_{22} \end{bmatrix} + \begin{bmatrix} q_1^2 & 0 \\ 0 & q_2^2 \end{bmatrix} = 0$$

which yields three algebraic equations:

$$\begin{aligned} p_{12}(X-Y) + p_{11}Y - \frac{p_{12}p_{22}}{V_h^2} &= 0 && (7.12) \\ 2p_{11}(X-Y) + q_1^2 - \frac{p_{12}^2}{V_h^2} &= 0 && (7.13) \\ 2p_{12}Y + q_2^2 - \frac{p_{22}^2}{V_h^2} &= 0 && (7.14) \end{aligned}$$

It now remains to determine p_{11}, p_{12}, p_{22}. Elimination of p_{11} and p_{12} from Eqns. (7.12)–(7.14) yields a quartic polynomial in p_{22} as follows:

$$\begin{aligned} p_{22}^4 - \big[4u^2(X-Y)\big]p_{22}^3 + \big[4u^4(X-Y)^2 - 2u^2q_2^2\big]p_{22}^2 + {}& \\ \big[4u^4(X-Y)q_2^2\big]p_{22} + \big[V_h^4 q_2^4 - 4Y^2u^6q_1^2 - 4u^6(X-Y)^2q_2^2 &= 0 && (7.15) \end{aligned}$$

The general quartic function $x^4 + bx^3 + cx^2 + dx + e = 0$ has at least two real roots if the derived polynomial $D = 64a^3e - 16a^2c^2 + 16ab^2c - 16a^2bd - 2b^4 < 0$ and $P = 8ac - 3b^2 < 0$. This can easily be shown in the case of Eqn. (7.15) for $q_1 > 0, q_2 > 0, V_h > 0$, and $X \neq Y$, as follows:

$$
\begin{aligned}
D &= -256V_h^6\big[(X-Y)^2q_2^2 + Y^2q_1^2\big] < 0 && (7.16)\\
P &= -16u^2\big[V_h^2(X-Y)^2 + 16q_2^2\big] < 0 && (7.17)
\end{aligned}
$$

Eqn. (7.15) can be solved for p_{22} using existing numerical techniques for polynomial roots. Using the positive real root of p_{22}, p_{11} and p_{12} are readily computed using Eqns. (7.13)–(7.14). Finally, the suboptimal lateral acceleration control law is obtained as follows:

$$a_y^* = -\frac{p_{12}(\eta - \chi_t)}{V_h} - \frac{p_{22}(\chi - \chi_t)}{V_h} \tag{7.18}$$

7.2.2 Vertical and Forward Acceleration Guidance Law

The target motion is assumed to be planar so that the target has no motion in the vertical plane. This assumption makes the engagement geometry in the vertical and forward axes identical to the geometry depicted in the Chapter 6.1, Fig. 6.1b. The derivation of the vertical and forward acceleration guidance laws is also identical to Sec. 6.2.2. For the sake of brevity, the derivations are not reproduced here.

7.2.3 Design Parameters and Implementation Aspects

A similar approach as Sec. 6.3 is followed for the choice of the parameters. The static gains $N_{(\cdot)}$ are selected in a manner that balances the state and control components in the SDRE cost function. The following gain values were found to satisfy tracking constraints while avoiding control saturation over a wide envelope: $N_\sigma = 700$, $N_\chi = 450$; $N_z = 0.07$, $N_w = 0.05$; and $N_u = 1$.

8 Simulation Results and Discussion

THE flight controller and guidance laws synthesized in the preceding chapters are now evaluated with regard to their closed-loop performance. The real-time capable modeling and simulation framework hosted in Matlab/Simulink and presented earlier in Section 4.4 is used for this purpose.

It is important to note the following points in respect of the simulation results presented in this section:

1. All simulations are performed in a real-time sense on a desktop computer that hosts the previously described Matlab/Simulink-based simulation environment.
2. With regard to handling quality ratings of the controller, an objective assessment based on the time-domain response criteria described in Ref. [4] is presented.
3. Subjective handling quality ratings based on pilot-in-the-loop evaluations are beyond the scope of this thesis.

8.1 Controller Performance Evaluation

The first set of simulations evaluates the performance of the SMC flight controller using the ADS-33 temporal responses criteria for each of the required response-types and interaxis coupling. Where relevant, the results are accompanied by a discussion of the HQs enhancement using the EMF controller [15], as well as the HQs of an unaugmented

BO105 helicopter based on flight testing results [96, 97]. Simulation results are then presented for the two selected MTEs.

8.1.1 Response-Types Characteristics

This section evaluates the character of SMC attitude hold, heading hold, and altitude hold by measuring impulse responses in trimmed hover, in accordance with the criteria specified by ADS-33E-PRF [4]. Beginning from $t = 0$, successive impulses of 20 % displacement from trim are inserted directly in the main and tail rotor actuators in the following sequence: longitudinal cyclic at $t = 3\,\mathrm{s}$, lateral cyclic at $t = 6\,\mathrm{s}$, tail rotor collective at $t = 9\,\mathrm{s}$, and main rotor collective at $t = 12\,\mathrm{s}$, as depicted in Fig. 8.1.

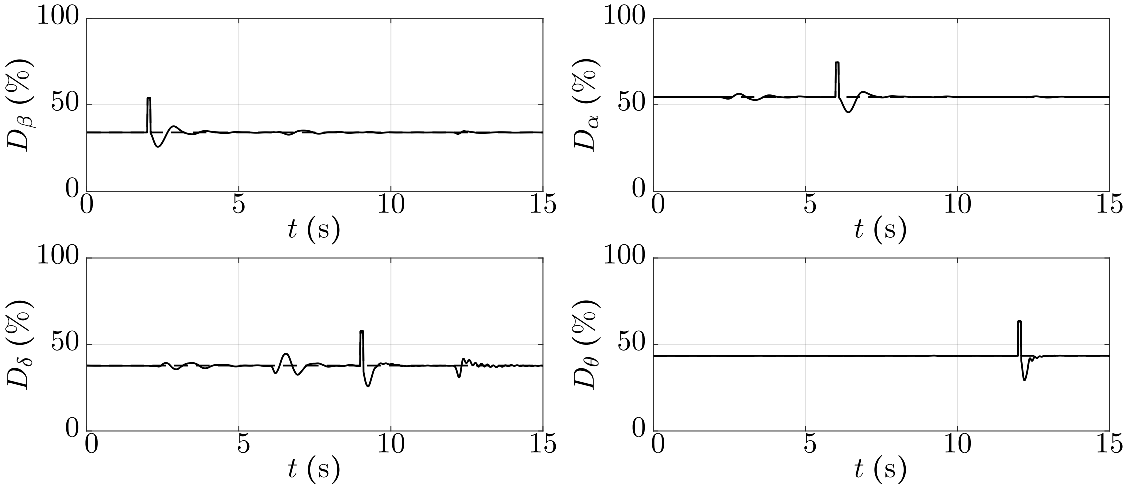

Figure 8.1: Impulse inputs in hover inserted in the main and tail rotor actuators, as required by ADS-33E-PRF [4] (- - -open loop, ——closed loop using SMC)

The resulting fuselage state histories in open-loop and closed-loop are plotted in Fig. 8.2. On the one hand, the open-loop responses highlight the helicopter's unstable dynamics and interaxis coupling. A longitudinal cyclic impulse induces a 5 °/s peak pitch rate accompanied by smaller roll and yaw rates, which lead to divergent longitudinal and lateral velocity components. An unstable phugoid mode can be observed from the longitudinal velocity response. Thereafter, a lateral cyclic impulse induces a

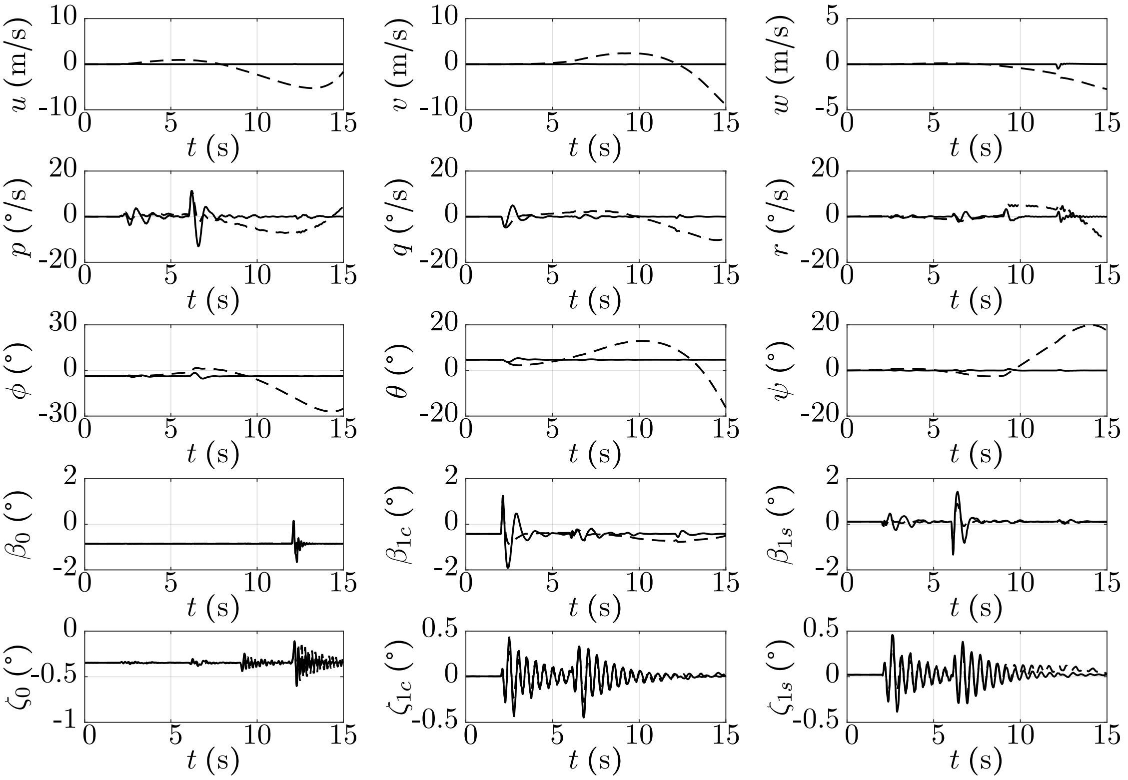

Figure 8.2: Open and closed-loop state responses to impulse inputs in hover (- - -open loop, ——closed loop using SMC)

10 °/s peak roll rate leading to a divergent roll attitude and lateral velocity component. The pitch rate continues to increase in amplitude. Subsequently, a tail rotor impulse produces a peak yaw rate, and finally, a main rotor collective affects both the normal velocity component and the yaw rate. On the other hand, the closed-loop responses are found to stabilize the angular rates. The pitch and roll attitudes, the normal velocity component, and the yaw rate return to their trim values within 1 s and remain stable thereafter, as required by ADS-33. Furthermore, the flapping and lead-lagging angle plots in Fig. 8.2 show all oscillations decaying to zero indicating that the continuous SMC laws stabilize the helicopter without interfering with the rotor dynamic modes.

These closed-loop responses also validate the controller's attitude hold, direction hold, and height hold characteristics.

8.1.2 Attitude Quickness and Interaxis Coupling

Attitude quickness determines the level of agility by measuring how rapidly commanded attitude changes are achieved. Whereas the required attitude changes must be quick, the resulting cross-coupling responses must be sufficiently mitigated. In hover and low speed, the interaxis coupling criteria specified by ADS-33 are pitch due to roll, roll due to pitch, and yaw due to collective. In forward flight, pitch due to roll, roll due to pitch, and pitch due to collective are specified. The following results evaluate predicted HQ for the SMC closed-loop with PCH and without PCH.

8.1.2.1 Pitch/roll attitude quickness and pitch/roll coupling

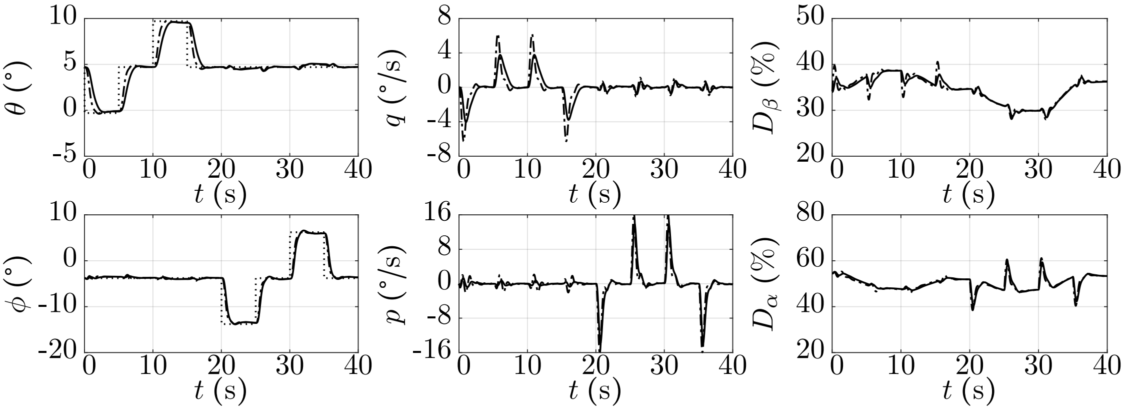

Figure 8.3: Pitch/roll quickness and coupling in hover (····· command, -·-· SMC, —— SMC with PCH)

Fig. 8.3 plots the responses of the pitch and roll attitudes and angular rates, and the cyclic inputs in hover to a ±5° commanded pitch attitude change from trim and a ±10° commanded roll attitude change from trim. As expected, both pitch and roll attitudes exhibit qualitative second-order system characteristics in accordance with the specified behavior for the ACAH response-type given by Eqn. (5.1)–(5.2).

SMC without PCH results in higher peak pitch and roll angular rates of 6 °/s and 16 °/s, respectively, as compared to 4 °/s and 14 °/s, respectively, for SMC with PCH. The corresponding control demand without PCH is also higher as compared to the control demand with PCH. In reaching the new steady states, the control inputs are devoid of reversals in the sign relative to the initial trim position. Furthermore, both the control inputs and the state responses are not found to contain high frequency chatter, which suggests that the choice of the boundary layer has provided a satisfactory continuous approximation for the discontinuous sliding mode control terms.

Pitch attitude quickness, which is measured as the ratio of peak pitch rate to change in pitch attitude ($q_{\text{pk}}/\Delta\theta_{\text{pk}}$), is 1.2 without PCH and 0.8 with PCH, whereas the Level 1 threshold in hover is ($q_{\text{pk}}/\Delta\theta_{\text{pk}}$) > 0.65 [4]. Likewise, roll attitude quickness, measured as ($p_{\text{pk}}/\Delta\phi_{\text{pk}}$), is 1.6 without PCH and 1.4 with PCH, whereas the Level 1 threshold in hover is ($p_{\text{pk}}/\Delta\phi_{\text{pk}}$) > 1.4 [4]. Thus, the closed-loop SMC including PCH satisfies predicted Level 1 HQ measured against the moderate amplitude pitch and roll attitude quickness criteria. In comparison, previous flight testing suggests that a bare-airframe BO105 possesses Level 1 HQ for the moderate amplitude pitch and roll criteria in hover [96]. This implies that SMC with PCH retains the Level 1 roll quickness HQ of the bare-airframe helicopter.

Next, roll due to pitch (or pitch due to roll) coupling is measured as the ratio of the peak off-axis roll attitude response (or peak off-axis pitch attitude response) from trim within 4 seconds to the required pitch attitude response (or required roll attitude response) from trim at 4 seconds. Quantitatively, both $|\Delta\phi_{\text{pk}}/\Delta\theta_{(t=4)}| \leqslant 0.25$ and $|\Delta\theta_{\text{pk}}/\Delta\phi_{(t=4)}| \leqslant 0.25$ for Level 1 HQ [4]. From Fig. 8.3, it is observed that $|\Delta\phi_{\text{pk}}/\Delta\theta_{(t=4)}| \leqslant 0.07$ and $|\Delta\theta_{\text{pk}}/\Delta\phi_{(t=4)}| \leqslant 0.04$ for the SMC closed-loop with PCH and without PCH, so that predicted Level 1 HQ are easily satisfied for the pitch and roll interaxis coupling. In comparison, a bare-airframe BO105 was found to possess Level 3 HQ for roll due to pitch coupling, and Level 1 and Level 2 HQ for pitch due to roll coupling in left and right roll motion, respectively [96]. This suggests that SMC including PCH significantly overcomes the severe pitch/roll coupling of the bare-airframe helicopter.

8.1.2.2 Yaw due to collective

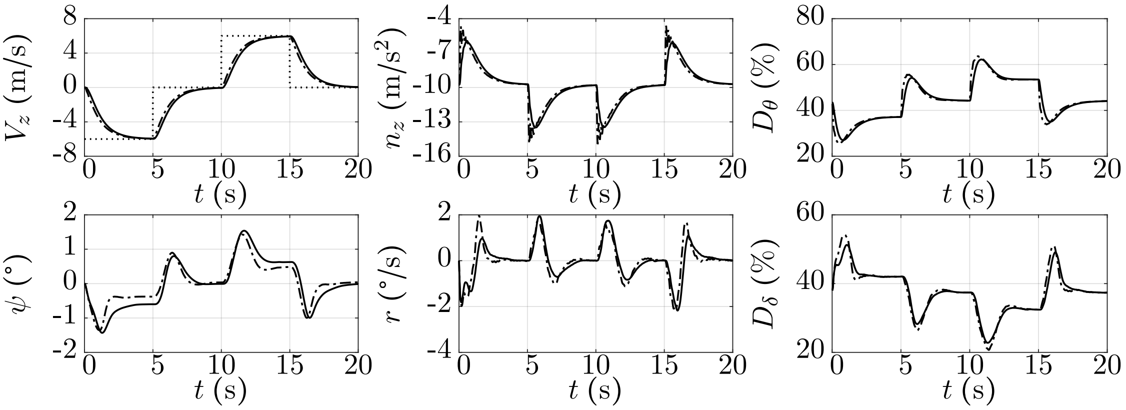

Figure 8.4: Yaw due to collective coupling in hover (····· command, -·-· SMC, —— SMC with PCH)

Yaw due to collective coupling assumes significance in hover and low speed when changes in the main rotor torque result in a yawing moment on the fuselage without the pilot's yaw compensation. Fig. 8.4 plots the responses in hover to vertical speed commands of ±6 m/s. It can be noticed that the vertical speed response has a qualitative first-order appearance as required for the RCHH response-type, and that steady state is reached within 5 s for both descent and climb. The response of the SMC closed-loop without PCH is more aggressive with peak incremental normal acceleration of $0.5g$ from $1g$ flight on either side, compared to $0.38g$ from $1g$ flight with PCH. The peak yaw rate induced by the collective input is bounded to within ±2 °/s and decays to zero within 4 s following the collective input. The helicopter heading remains essentially constant in descent and climb both. The collective and pedal control inputs are devoid of reversals in the sign relative to the initial trim position and are also free of high frequency chatter.

Yaw due to collective coupling is measured in terms of $r_3/|V_{z,(t=3)}|$°/s/ft/s and $|r_1/V_{z,(t=3)}|$°/s/ft/s, where r_1 is the first yaw rate peak following a vertical speed command, and $r_3 = r_{(t=3)} - r_1$ for $r_1 > 0$, or $r_3 = r_1 - r_{(t=3)}$ for $r_1 < 0$. The Level 1 HQ boundaries are set as $-0.15 \leqslant r_3/|V_{z,(t=3)}| \leqslant 0.2$ and $|r_1/V_{z,(t=3)}| \leqslant 0.65$ [4]. These metrics for the SMC closed-loop with and without PCH, as computed from Fig. 8.4, are found to lie in the following range: $-0.12 \leqslant r_3/|V_{z,(t=3)}| \leqslant -0.08$ and $0.08 \leqslant |r_1/V_{z,(t=3)}| \leqslant 0.12$. This implies that the SMC closed-loop responses lie within the Level 1 thresholds for yaw due to collective coupling. In contrast, a bare-airframe BO105 was found to possess Level 3 HQ for the yaw due to collective coupling criteria for climb and descent both [97], once again highlighting the efficacy of the SMC closed-loop.

8.1.2.3 Pitch due to collective

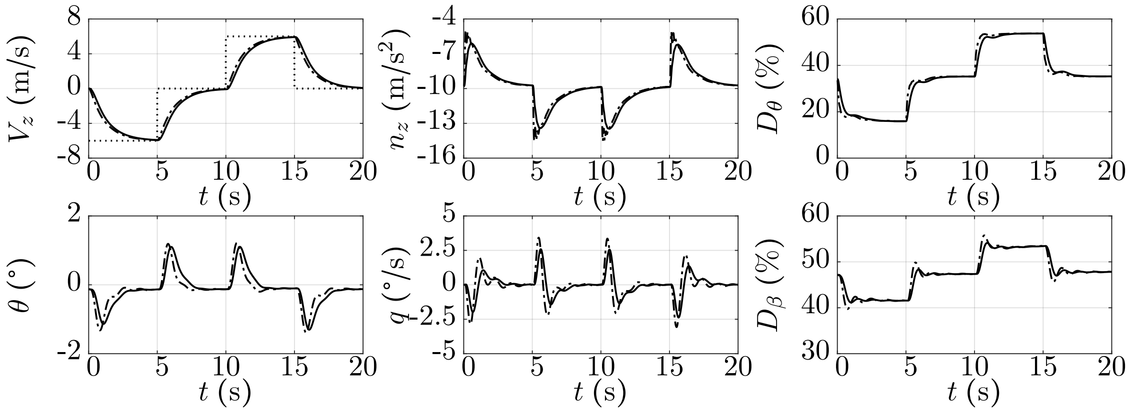

Figure 8.5: Pitch due to collective in 40 m/s forward flight (——SMC, -·-·SMC+PCH)

Fig. 8.5 plots the responses in 40 m/s forward speed to vertical speed commands of ±6 m/s. As in the hover case, the vertical speed response in forward flight too depicts a qualitative first-order appearance as required for the RCHH response-type, and steady state is reached within 5 s. The SMC closed-loop without PCH induces a higher peak incremental normal acceleration of $0.48g$ from $1g$ flight on either side as compared to $0.37g$ from $1g$ flight with PCH. The deviation of pitch attitude from trim is bounded to within $\pm 1.5^\circ$.

Pitch due to collective is measured as the ratio of the peak change in pitch altitude within the first 3 s to the peak incremental normal acceleration. As the change in collective inputs amounts to a torque change of less than 20 %, the small collective input criterion is applied so that $|\Delta\theta_{\text{peak}}/\Delta n_{z\text{peak}}| < 1^\circ/\text{ft/s}^2$ for Level 1 HQ [4]. From Fig. 8.5, $|\Delta\theta_{\text{peak}}/\Delta n_{z\text{peak}}| \leqslant 0.1^\circ/\text{ft/s}^2$ is observed in both descent and climb indicating that Level 1 HQ are achieved. In comparison, a bare-airframe BO105 has Level 2 pitch/collective coupling [96], which demonstrates the improved responses with the SMC closed-loop.

8.1.3 Slalom Mission Task Element

The ADS-33 slalom MTE from Ref. [4] is chosen to evaluate maneuverability, turn coordination, and axes decoupling in forward flight. Slalom is an aggressive task element and requires moderate agility: $\theta_c \in [-30, +20]^\circ$, $\phi_c \in [-60, +60]^\circ$ and $r_c \in [-22, 22]^\circ/\text{s}$ for Level 1 HQs [4].

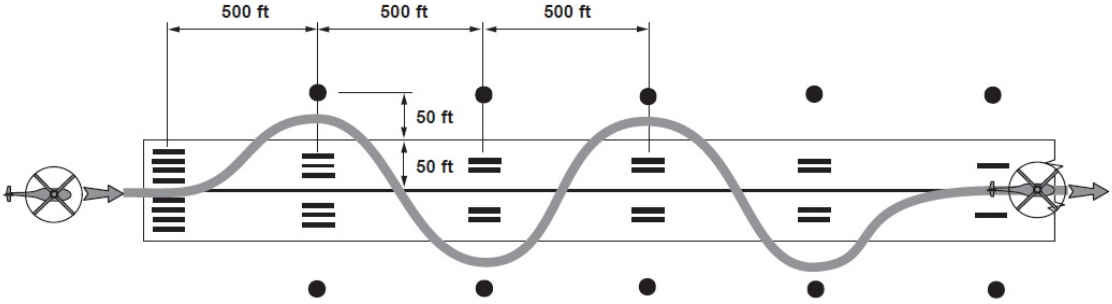

Figure 8.6: Course setup and desired flight path in the slalom MTE from Ref. [4]

Fig. 8.6 depicts the course setup and the required flight path in the slalom MTE. The maneuver is initiated in trimmed, level flight oriented along North. A series of turns at 500 ft. (150 m) are performed on each side of the North axis. Each turn requires at least 50 ft. (15 m) and up to 100 ft. (30 m) of lateral distance from the North axis. For the purpose of command tracking by the flight controller, the required flight path can be modeled using sinusoidal functions of the y-coordinate and the ground track angle as follows:

$$\begin{aligned} y &= A_{\mathrm{sl}} \sin\left(\frac{2\pi x}{d_{\mathrm{sl}}}\right) && (8.1) \\ \chi_c &= \arctan\left\{\frac{2\pi A_{\mathrm{sl}}}{d_{\mathrm{sl}}} \cos\left(\frac{2\pi x}{d_{\mathrm{sl}}}\right)\right\} && (8.2) \\ V_{h,c} &= [20, 30]\frac{\mathrm{m}}{\mathrm{s}} && (8.3) \end{aligned}$$

where $A_{\mathrm{sl}} \in [15, 30]\mathrm{m}$, and $d_{\mathrm{sl}} = 600\,\mathrm{m}$. Executing slalom at 30 m/s is considered desirable, whereas 20 m/s is considered adequate. The altitude shall be maintained essentially constant in the entire maneuver. During simulations, actuator saturations were observed in the slalom MTE. To alleviate this issue, PCH layers in the inner and outer loop were activated.

Fig. 8.7 plots the ground positions and the altitude in a slalom MTE flown at 30 m/s forward speed and 30 m altitude. It shows that for the SMC closed-loop with PCH and without PCH, the lateral flight path successfully passes between the ground markers on either side of the reference line until wings level at 750 m horizontal distance. Also observed in Fig. 8.7 is the altitude that is held to within ±1 m from its reference value during the entire maneuver.

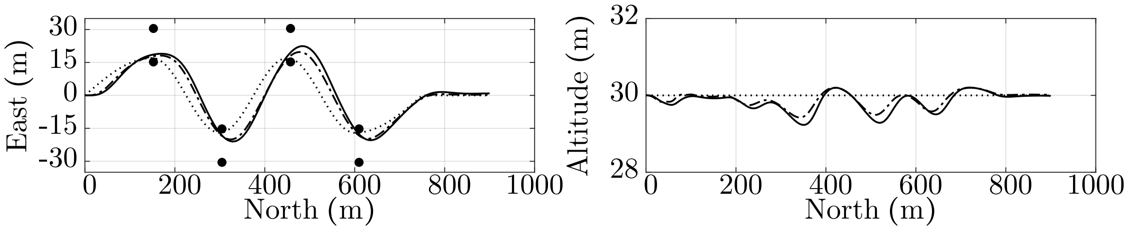

Figure 8.7: Flight paths during slalom MTE at 30 m/s (····· desired, -·-· SMC, —— SMC with PCH)

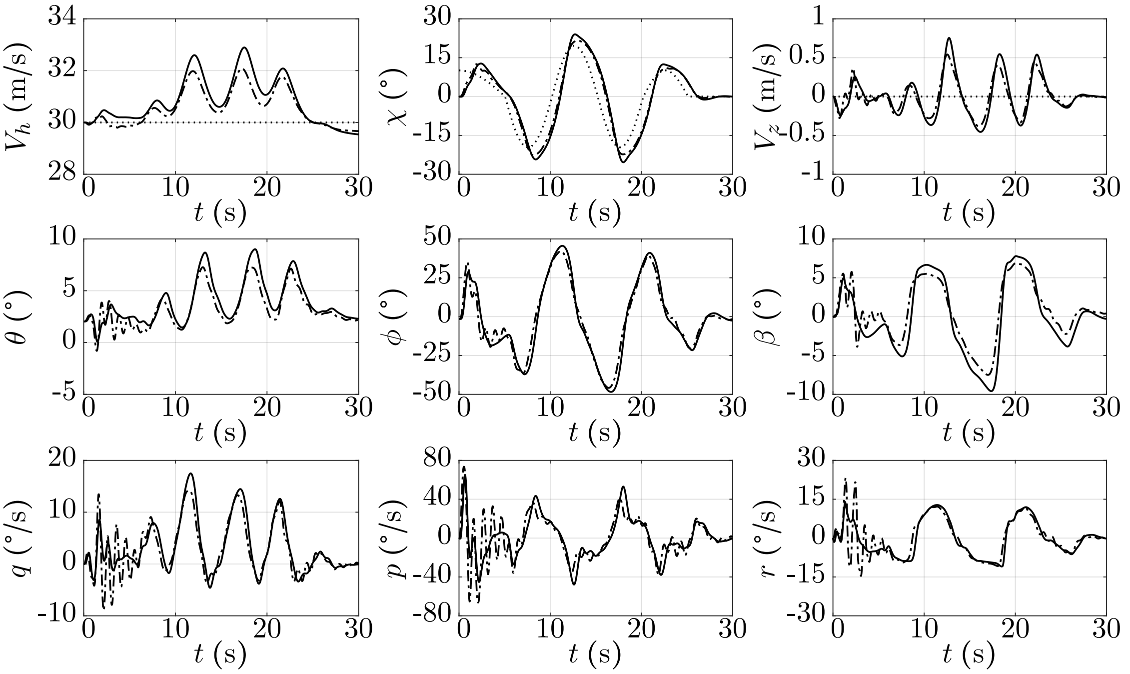

Figure 8.8: State variables during slalom MTE at 30 m/s (⋯⋯ command, -·-· SMC, —— SMC with PCH)

The time histories of the fuselage states are plotted in Fig. 8.8. It can be observed that the deviation in forward speed (V_h) and vertical speed (V_z) from the respective reference values is small. The ground track (χ) plot shows the rapid track changes induced while passing between the ground markers. The successive turns induce high roll rates (p) of up to 50 °/s, and peak pitch rates (q) and peak yaw rates (r) of 18 °/s and 15 °/s, respectively. Sideslip (β) remains within ±10° during the entire maneuver suggesting that the yaw rate command achieves satisfactory turn coordination. It can be observed that the angular rate responses for the SMC closed-loop with PCH are significantly less aggressive than those without PCH while still meeting the desired level of performance in the slalom MTE.

The time histories of the control inputs are plotted in Fig. 8.9. It can be observed that the SMC closed-loop without PCH commands aggressive lateral cyclic (D_α) and pedal (D_δ) leading to actuator saturations in these control channels in the initial phase of the

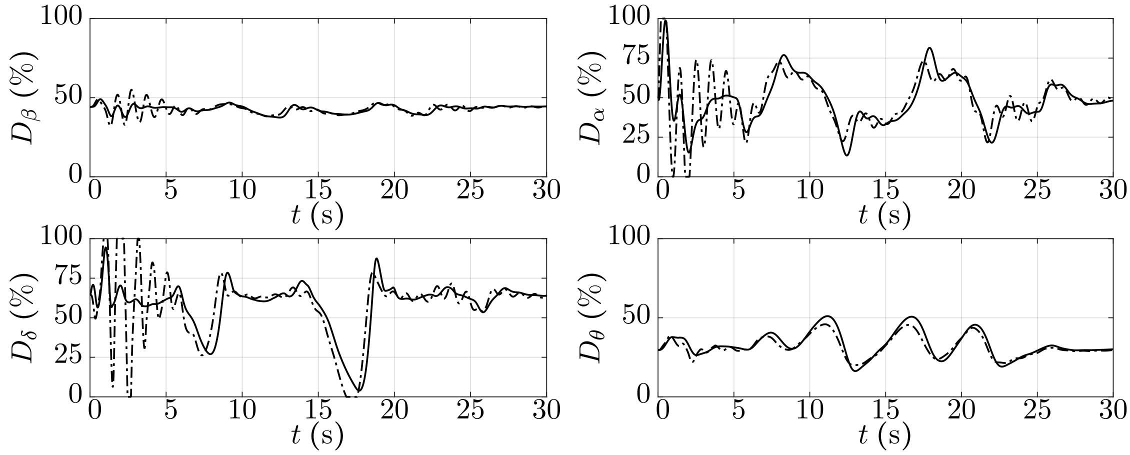

Figure 8.9: Control inputs in slalom MTE at 30 m/s (-·-·SMC, ——SMC with PCH)

trajectory. The pedal is again saturated while executing a right banked turn around one of the ground markers. However, the control responses of the SMC closed-loop with PCH are found to be smoother, less aggressive, and devoid of actuator saturations while still meeting the desired level of performance. These results illustrate the effectiveness of PCH in moderating aggressive SMC control action in the presence of uncertainties.

8.1.4 Combined Acceleration/Deceleration and Bob-Up/Bob-Down Mission Task Element

A combination of two MTEs, namely the acceleration/deceleration MTE requiring aggressive agility, and the vertical maneuver MTE requiring moderate agility, both based on Ref. [4], is chosen to evaluate maneuverability and axes decoupling in low speed and hover. For aggressive agility, the large amplitude requirements for Level 1 HQs are: $\theta_c \in [-30, 30]^\circ$, $\phi_c \in [-60, +60]^\circ$ and $r_c \in [-60, 60]^\circ$/s [4].

Fig. 8.10 depicts the course setup and the required flight path in the combined acceleration/deceleration and bob-up/bob-down MTE. The maneuver is initiated in trimmed, level flight at an altitude of 50 m and forward speed 25 m/s. The helicopter is rapidly decelerated to stable hover, followed by a 30 m descent and stabilization for 2 s, followed

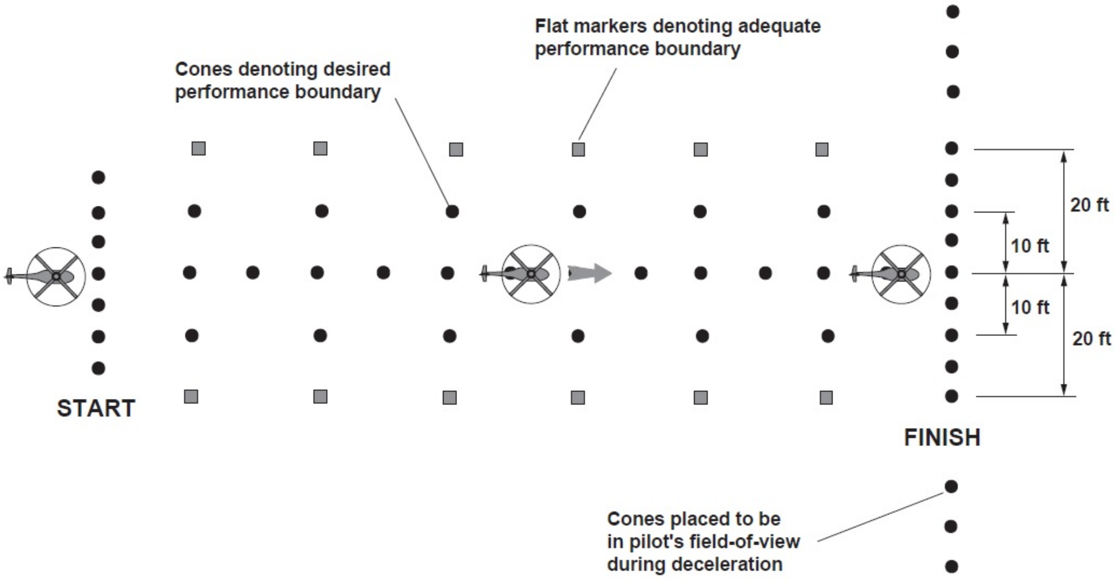

Figure 8.10: Course setup and required flight path in the acceleration/deceleration and bob-up/bob-down MTE from Ref. [4]

by a 30 m ascent and stabilization for 2 s. Thereafter, the helicopter is rapidly accelerated to 25 m/s followed by a deceleration back to stable hover. Finally, a 30 m ascent, stabilization for 2 s, and a 30 m descent completes the task.

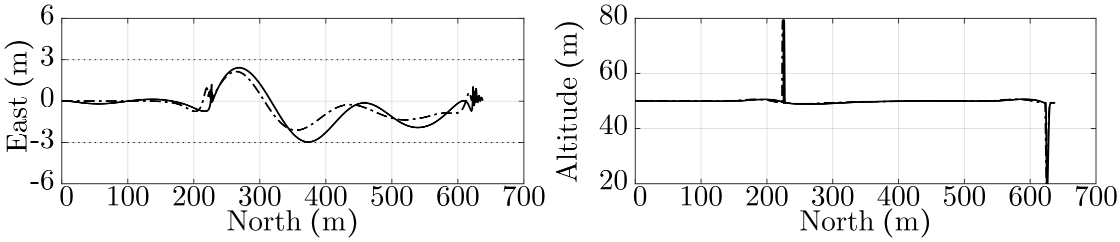

Figure 8.11: Flight paths during combined acceleration/deceleration and bob-up/bob-down MTE (····· desired performance bound, -·-· SMC, —— SMC with PCH)

In the combined acceleration/deceleration and bob-up/bob-down MTE, the roll attitude tracks lateral velocity commands for regulating the cross-track error, and the yaw rate regulates heading to zero. In Fig. 8.11, the ground positions plot shows that the desired path performance of up to 3 m cross-track deviation from the centerline is achieved. The altitude remains constant during acceleration/deceleration, and rapidly achieves the 30 m ascent and descent while in hover.

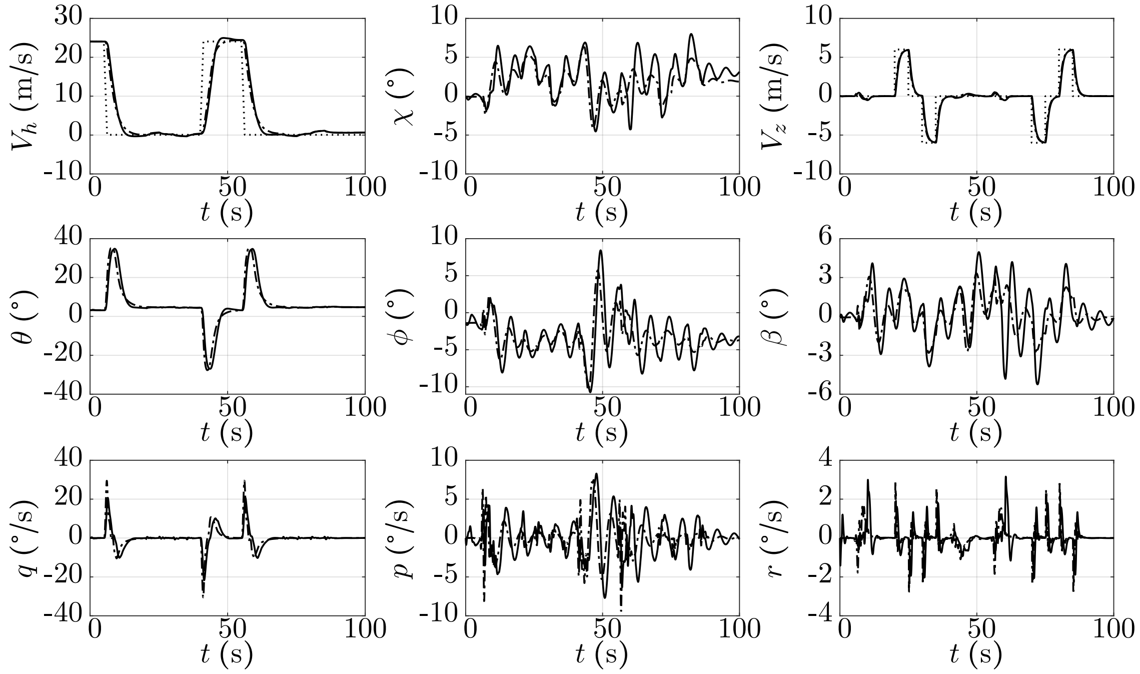

Figure 8.12: State variables during combined acceleration/deceleration and bob-up/bob-down MTE (·····command, -·-·SMC, ——SMC with PCH)

Fig. 8.12 plots the fuselage states. The deceleration to hover and acceleration to forward flight phases observed in the forward speed (V_h) plot demand a peak pitch change ($\Delta\theta$) of 30°, as required for desired performance [4]. The peak pitch rate (q) is 30 °/s without PCH, and 20 °/s with PCH. The ground track (χ) and the sideslip (β) are held within ±6° as a consequence of the commanded yaw rate (r) and roll attitude (ϕ) tracking in the inner loop, respectively, which also satisfies desired performance [4]. The vertical speed (V_z) plot is regulated to zero during the acceleration/deceleration, and depicts a first-order behavior in climb and descent rates.

Fig. 8.13 plots the four control inputs. As observed there, actuator saturation is not encountered in this MTE. The control performance of the SMC closed-loop is satisfactory with PCH and without PCH. These results suggest that ADS-33 desired performance

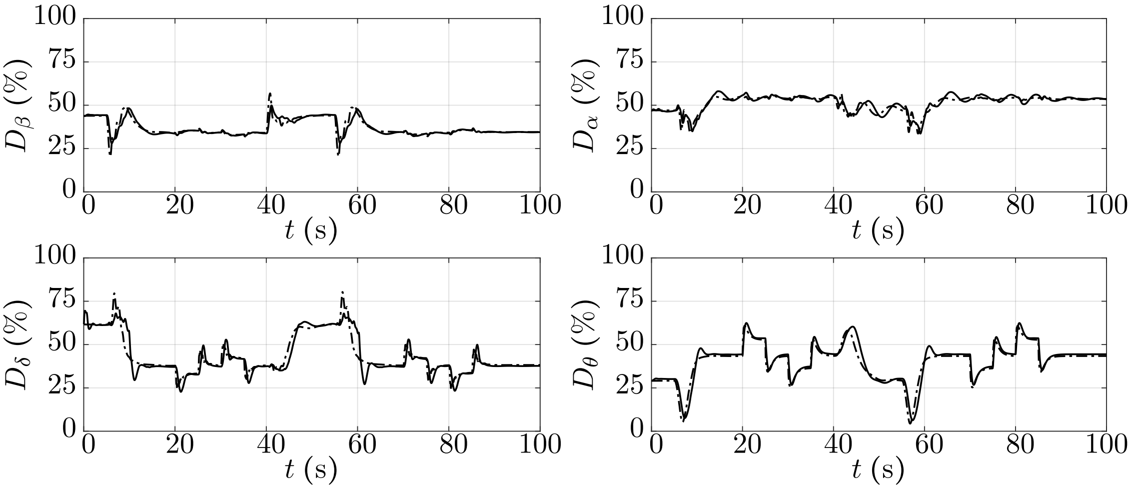

Figure 8.13: Control inputs during combined acceleration/deceleration and bob-up/bob-down MTE (-·-·SMC, —SMC with PCH)

criteria are met in the case of the acceleration/deceleration and bob-up/bob-down maneuver.

8.1.5 Comparison of SMC and EMF Control Performances

For comparison purposes, the same required response characteristics that were chosen for the SMC (see Sec. 5.1) were also applied to the EMF controller: $\zeta_\theta = 0.9$, $\omega_\theta = 2.34$, $\zeta_\phi = 0.75$, $\omega_\phi = 2.34$. These parameters yield $\omega_{\mathrm{bw},\theta} = 5.25\,\mathrm{rad/s}$ and $\omega_{\mathrm{bw},\phi} = 4.68\,\mathrm{rad/s}$. However, during simulations with the EMF controller, it was observed that larger roll amplitude commands led to instabilities. Therefore, only ω_ϕ in Eqn. (5.2) for the EMF controller was reduced from 2.34 to 1.6. This modification, however, degrades the roll axis HQ in EMF as seen in the following discussion.

8.1.5.1 Comparison of Moderate Amplitude Responses

The achievable on-axis handling qualities for the SMC and EMF controller are compared here. Figs. 8.14a–8.14c plot $q_{\mathrm{pk}}/\Delta\theta_{\mathrm{pk}}$ versus $\Delta\theta_{\min}$ for pitch attitude quickness, $p_{\mathrm{pk}}/\Delta\phi_{\mathrm{pk}}$ versus $\Delta\phi_{\min}$ for roll attitude quickness, and $r_{\mathrm{pk}}/\Delta\psi_{\mathrm{pk}}$ versus $\Delta\psi_{\min}$ for yaw

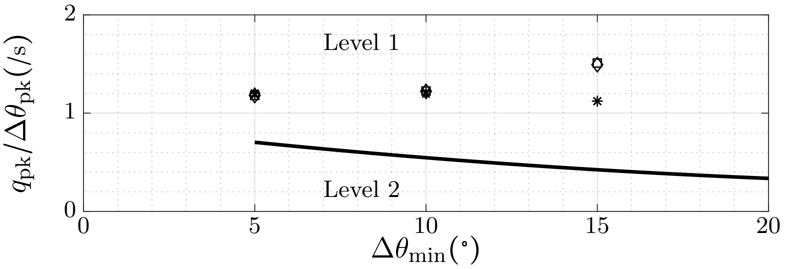

(a) Pitch axis (□ SMC pitch down, ◇ SMC pitch up, × EMF pitch down, ∗ EMF pitch up)

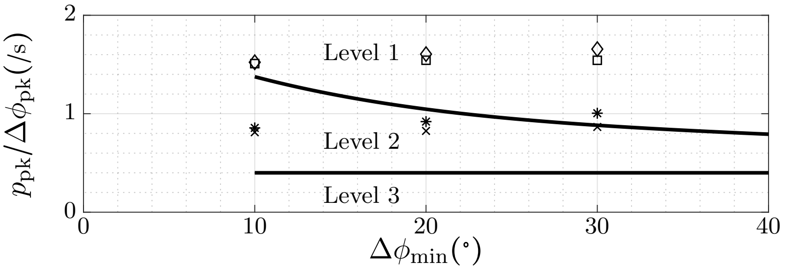

(b) Roll axis (□ SMC roll left, ◇ SMC roll right, × EMF roll left, ∗ EMF roll right)

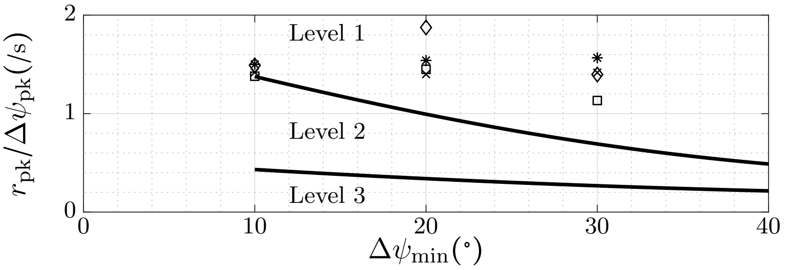

(c) Yaw axis (□ SMC yaw left, ◇ SMC yaw right, × EMF yaw left, ∗ EMF yaw right)

Figure 8.14: Comparison of the moderate-amplitude responses between SMC and EMC controller

attitude quickness, respectively. Here, $(\cdot)_{\mathrm{pk}}$ is the peak following a step command and $(\cdot)_{\min}$ is the minimum after the first peak. Using thresholds defined by ADS-33 [4], it is observed that the SMC controller satisfies predicted Level 1 HQ in pitch, roll, and yaw axes, whereas the EMF controller satisfies predicted Level 1 HQ in pitch and yaw axes, but only Level 2 HQ in roll axis. The roll axis HQ degradation is, however, a result of the reduction in natural frequency of the required response characteristics in the EMF controller.

8.1.5.2 Comparison of Level of Interaxis Coupling

Fig. 8.15 shows a summary of the comparison of the level of interaxis coupling achieved by each of the two flight controllers - SMC and EMF - using the thresholds specified in ADS-33 [4]. A comparison of the pitch due to roll coupling, plotted in Fig. 8.15a, shows that the off-axis peak pitch attitude response of the EMF controller in hover extends to the Level 2 zone. In low-speed, however, its response remains well within the Level 1 threshold. In contrast, the same quantity measured for the SMC controller remains within the Level 1 threshold in both hover and low-speed.

Further, Fig. 8.15b plots the off-axis peak roll attitude to the on-axis desired pitch attitude and the corresponding thresholds specified in ADS-33 [4]. It is noticed that both SMC and EMF are well within the Level 1 threshold in both hover and low-speed.

Finally, Fig.8.15c shows the yaw due to collective in hover for climb and descent based on the evaluation criteria and thresholds specified in ADS-33 [4]. It can be noticed that the EMF controller in both climb and descent possesses Level 2 HQ, whereas the SMC controller lies within the Level 1 threshold.

8.1.5.3 Comparison of Hover Performance in Turbulence

This simulation compares the robustness of the SMC and the EMF controllers in a station-keeping task in the presence of turbulence. The helicopter is oriented along north ($\psi = 0$) in stable hover and the CETI filters, defined in Sec. 4.3, corresponding to high-intensity turbulence are applied [99]. Each controller is command to regulate the pitch, roll, and yaw attitudes in order to maintain stable hover despite the turbulence. No additional robustness countermeasures are applied.

The dynamic responses are plotted in Fig. 8.16. The responses using the SMC controller depict maximum deviations of 1.5°, 3°, and 4° in pitch, roll, and yaw attitudes, respectively, from the respective trim values. The vertical speed variation lies in the range of ±0.2 m/s. Fig. 8.16 also shows that the helicopter is able to hold ground posi-

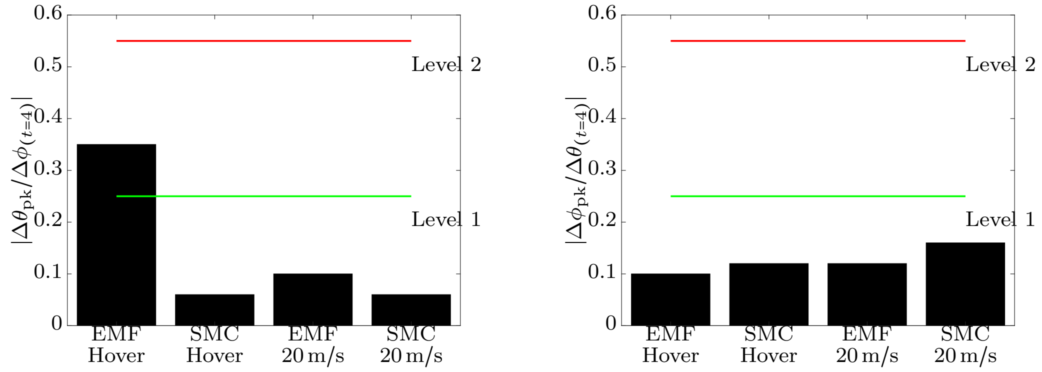

(a) Comparison of pitch due to roll coupling **(b)** Comparison of roll due to pitch coupling

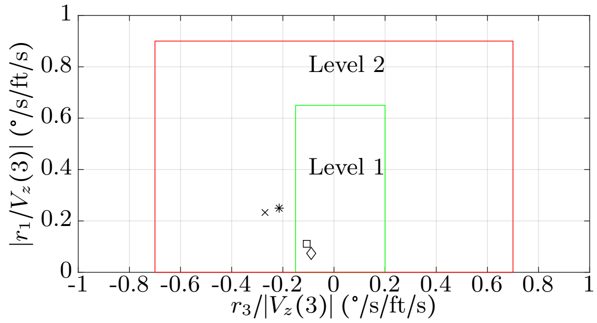

(c) Comparison of yaw due to collective coupling in hover (□ SMC in climb, ◊ SMC in descent, × EMF in climb, ∗ EMF in descent)

Figure 8.15: Comparison of interaxis coupling between SMC and EMF controllers

tion to within 0.25 m from simulation start. The corresponding responses using the EMF controller show maximum deviations of 4°, 3°, and 10° in pitch, roll, and yaw attitudes, respectively, from the respective trim values. The vertical speed variation with EMF lies in the range of ±0.6 m/s. Ground positions using EMF are held to within 0.6 m from simulation start. These results suggest that SMC has a slight advantage over EMF in terms of tracking accuracy and active exogenous disturbance rejection.

8.1.6 Summary of Predicted Handling Quality Enhancement

Table 8.1 summarizes the predicted HQ levels evaluated from the preceding simulation studies for each of the different control augmentation approaches evaluated in this

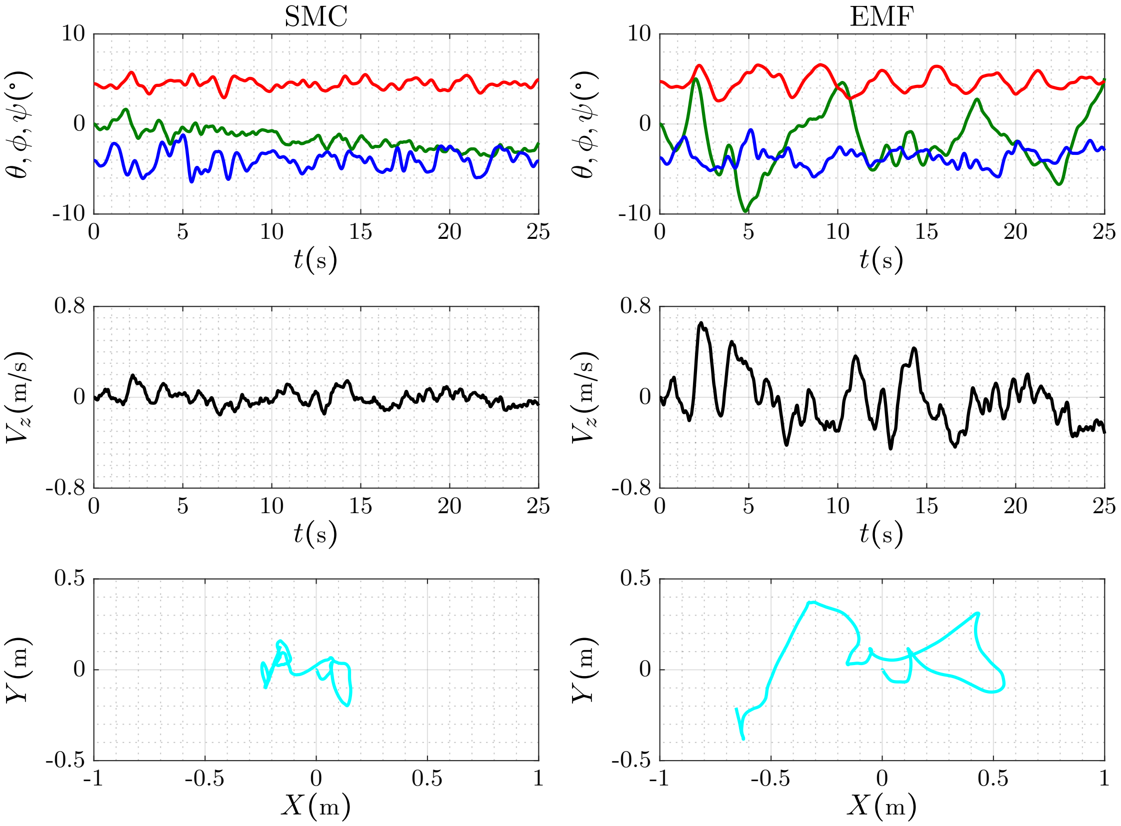

Figure 8.16: SMC versus EMF performance in high-intensity turbulence (—θ, —ϕ, —ψ, —V_z, —ground positions)

section. Unsurprisingly, the BO105 bare-airframe responses, determined from extensive flight testing in Ref. [96, 97], are rather poor. While EMF control design shows satisfactory performance with up to Level 1 HQ for the moderate amplitude criterion, its interaxis coupling performance is unsatisfactory. In contrast, the SMC controller achieves Level 1 HQ for both moderate amplitude and interaxis coupling criteria. The inclusion of the PCH layer, as discussed, reduces the peak angular rates but still achieves up to Level 1 HQ.

It is noted that the closed-loop sliding mode control responses are in accordance with the required lower-order response characteristics as defined in Section 5.1. For other helicopter flight controllers where comfort is desirable (for instance in civilian applica-

Evaluation Method		Predicted HQ Level			
Criterion	Axes	BO105 Bare-airframe From [96, 97]	EMF	SMC	SMC +PCH
Moderate Amplitude	Pitch	NA	1	1	1
	Roll	1	2	1	1
	Yaw	NA	1	1	1
Interaxis Coupling	Pitch due to roll	1-2	2	1	1
	Roll due to pitch	3	1	1	1
	Pitch due to collective	2	2-3	1	1
	Yaw due to collective	NA	2	1	1

Table 8.1: Summary of predicted handling quality enhancement using sliding mode control

tions), the designer may choose to specify lower-order response characteristics that yield less aggressive responses.

8.2 Waypoint Guidance Performance Evaluation

In this section, the waypoint guidance laws are evaluated in a real-time, online sense for different waypoint constraints and different target maneuvers. Once again, all simulations are performed in a real-time sense on a desktop computer that hosts the previously described Matlab/Simulink-based simulation environment. In the following simulations, the success criterion for waypoint tracking is set as $r < 10\,\mathrm{m}$.

8.2.1 Minimum Waypoint Spacing

To demonstrate waypoint spacing limits, a scenario with $V_h = V_{h,t} = 60\,\mathrm{m/s}$, $z = z_t = 800\,\mathrm{m}$, and $\{\chi, \chi_t\} \in \{-135°, -45°, 45°, 135°\}$ is considered. For $|\phi_{\max}| \approx 45°$, $R_{\min} = 370\,\mathrm{m}$ is obtained. Closed-loop simulations are performed from initial position $(0, 0, 800)$m. At $\Gamma = 6$, and $d_\chi = 2220\,\mathrm{m}$, the trajectories converge to $|e_\chi| \leqslant 15°$ and $d \leqslant 20\,\mathrm{m}$ for all $\{\chi, \chi_t\}$, and the convergence improves for $\Gamma \geqslant 6$. The 2D flight paths with $\Gamma = 6$ are plotted in Fig. 8.17. Note that, for $|a_{x_{\max}}|$ and for all $V_h \in [20, 60]$m/s, $d_{V_h} < 2220\,\mathrm{m}$ is obtained. Furthermore, $d_z \leqslant 340\,\mathrm{m}$ is estimated using d_χ and t_{go} from Eqn. (6.14).

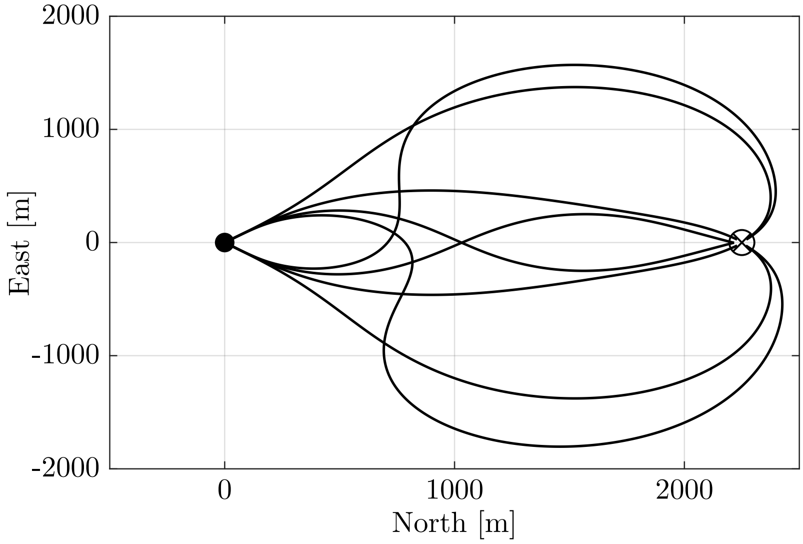

(a) $\chi \in \{-45°, 45°\}$

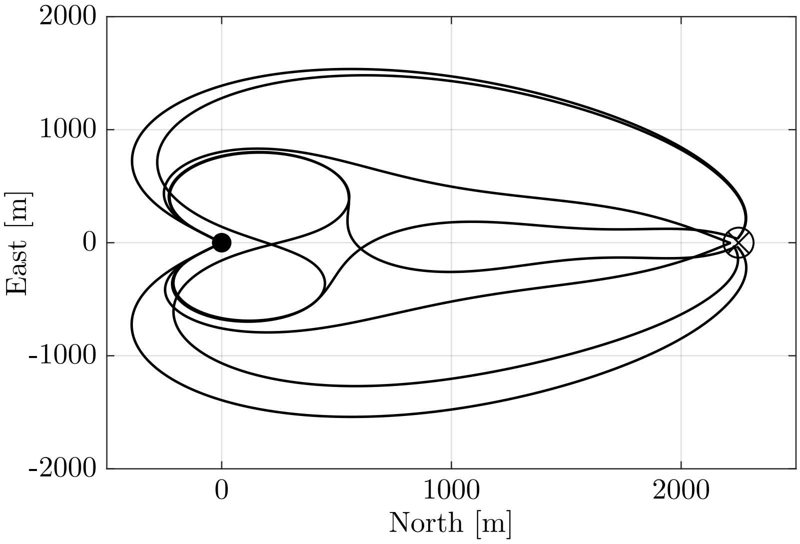

(b) $\chi \in \{-135°, 135°\}$

Figure 8.17: 2D flight paths for $d_\chi = 2220\,\mathrm{m}$, $|\phi_{\max}| \approx 45°$, $\chi_t \in \{-135°, -45°, 45°, 135°\}$

These results indicate that the SDRE guidance laws are suboptimal in terms of the flight path distance between two waypoints, when compared to the Dubins long path distance, where the Dubin's long path consists of a curved path, a straight line, and another curved path sequentially. However, beyond the minimum horizontal distance, satisfactory convergence to the terminal constraints with minimum number of turns is observed. Furthermore, by directly delivering acceleration commands to the flight controller, an intermediate trajectory generation step for path following is avoided.

8.2.2 3D Waypoint Trajectory Generation Results and Discussion

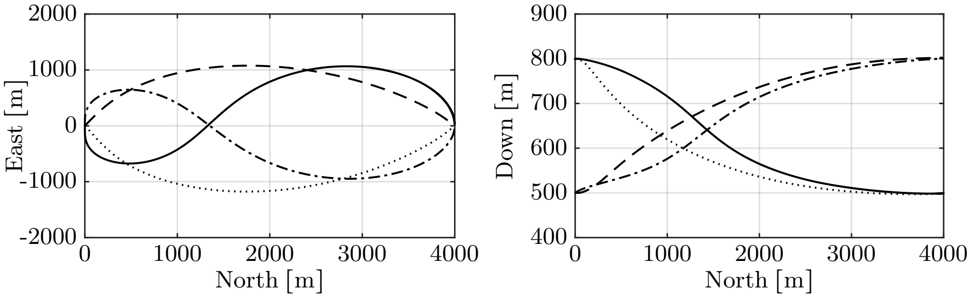

Figure 8.18: 3D flight path under terminal velocity vector constraints (——Case1 - - -Case2 -·-·Case3 ·····Case4)

Next, two waypoints with ground coordinates $(0,0)$m and $(4000,0)$m are considered for simultaneous tracking of three-dimensional velocity vector constraints. Four cases are simulated to cover different combinations of horizontal, lateral and vertical flight path profiles. Case 1 is a deceleration from 60 m/s to 20 m/s with a descent from 800 m to 500 m. The initial and final track angles are $-90°$. Case 2 is an acceleration from 30 m/s to 60 m/s with a climb from 500 m to 800 m. The initial track is 60° and the final track is $-60°$. Case 3 is a deceleration from 60 m/s to 30 m/s with a climb from 500 m to 800 m. The initial and final track angles are 90°. Case 4 is an acceleration from 20 m/s to 60 m/s and a descent from 800 m to 500 m. The initial track is $-60°$ and the final track is 60°.

The ground position and altitude histories are plotted in Fig. 8.18, which shows a smooth evolution (i.e. without discontinuities) of the flight paths from the initial to the

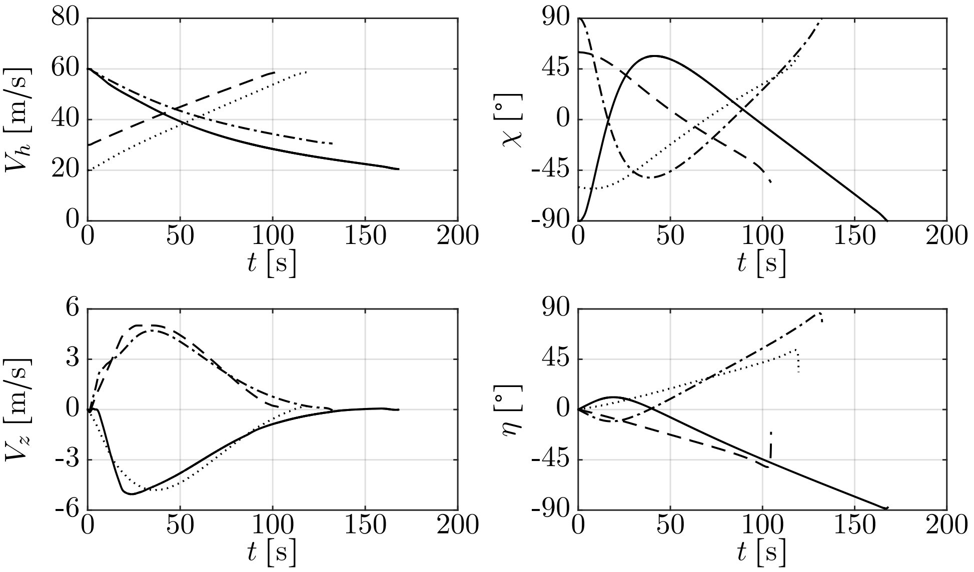

Figure 8.19: Velocity and track angle trajectories under terminal velocity vector constraints (——Case1 - - -Case2 -·-·Case3 ·····Case4)

final coordinates. Lateral turns and altitude changes are evenly distributed over the flight path trajectories. The velocity vector and line-of-sight histories are plotted in Fig. 8.19. The required horizontal velocities are achieved and the vertical velocities approach zero, allowing the helicopter to level off at the terminal waypoint. The actual ground track and the line-of-sight angle are simultaneously regulated to the value of the required final track angle to ensure precise directional and ground position tracking. The corresponding acceleration commands for each case are depicted in Fig. 8.20. The forward and vertical acceleration commands approach zero, yielding steady-state conditions in these axes. The lateral acceleration plot depicts a steady demand for turning flight tending to zero towards the end.

Finally, a scenario with a sequence of 6 waypoints, each separated by 2800 m horizontally and 100 m vertically, is simulated. The constraints on the horizontal velocity and

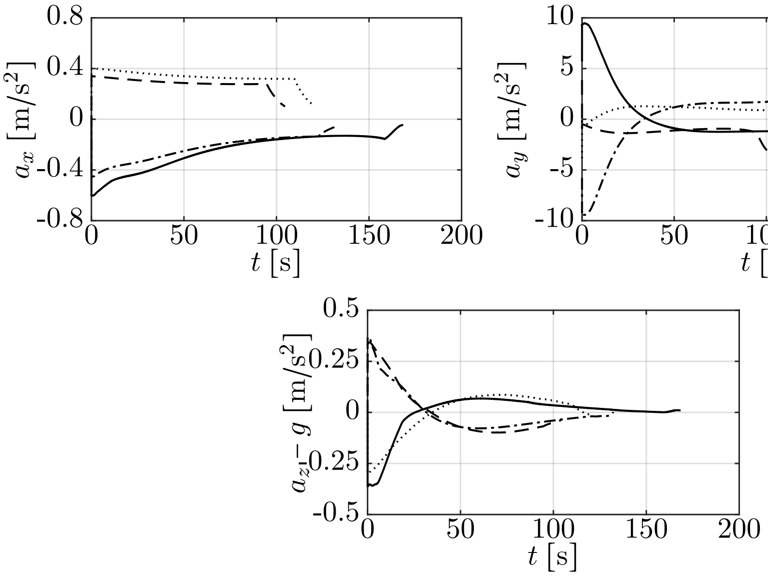

Figure 8.20: Acceleration histories under terminal velocity vector constraints (——Case1 - - -Case2 -·-Case3 ·····Case4)

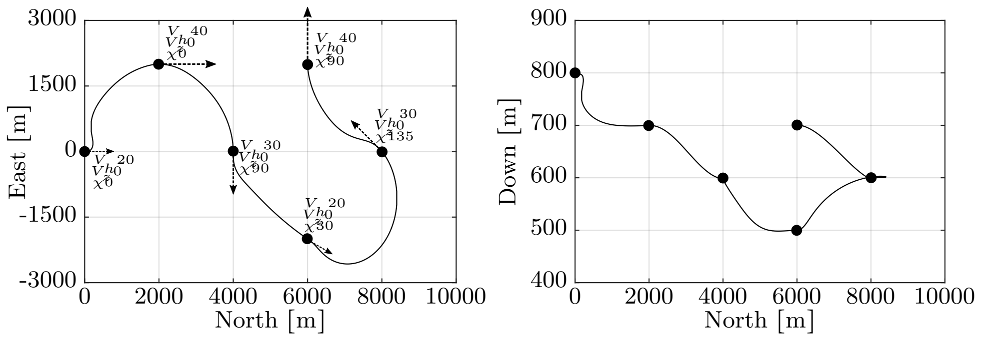

Figure 8.21: 3D flight path in a waypoint sequence

ground track are varied in the range of $[20, 40]$m/s and $[-90, 135]°$ respectively, and each waypoint requires a level off ($V_{z,t} = 0\,\text{m/s}$) as shown by the arrowheads in Fig. 8.21.

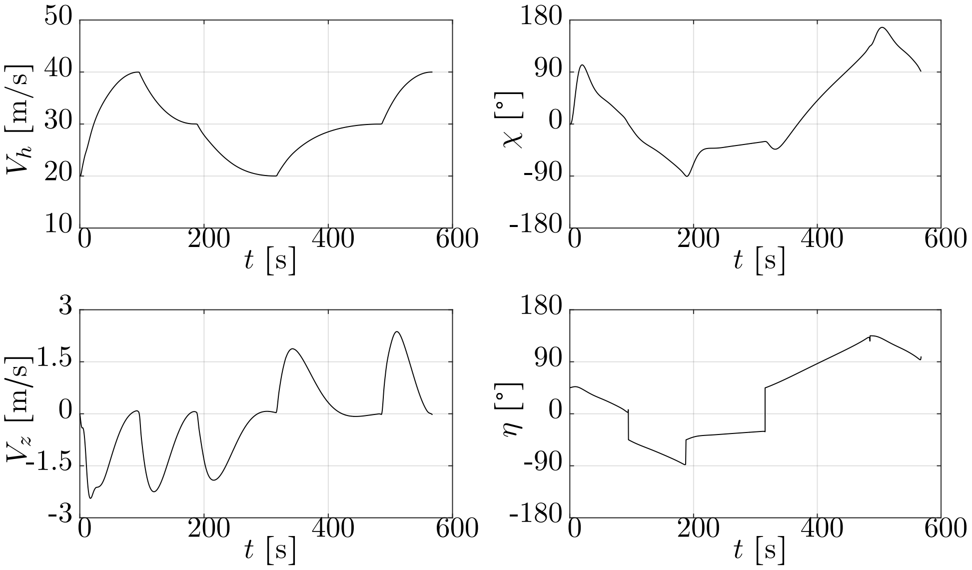

Figure 8.22: Velocity and track angle trajectories in a waypoint sequence

Also shown in the same figure are the actual smooth geometric flight paths between the waypoints executed by the helicopter. The corresponding velocity vector histories plotted in Fig. 8.22 highlight that the velocity vector constraint at each waypoint is achieved. The helicopter reaches steady state at each waypoint. In all simulation scenarios, it is observed that despite decoupling of the axes for trajectory generation, the flight path and velocity vector objectives in each axis are satisfied.

8.3 Rendezvous Guidance Performance Evaluation

A slow moving target with constant speed $V_t = 20\,\text{m/s}$ is considered for rendezvous. Four cases of lateral maneuvering profiles for the target are simulated: constant heading, constant heading rate, sinusoidal heading rate, and multisinusoidal heading rate. In all cases, the target's initial position is $(2000, 2000, 10)$m. The helicopter's initial position, horizontal velocity, and heading are $(0, 0, 400)$m, 50 m/s, and 0°, respectively.

To reduce the likelihood of aggressive lateral maneuvers in low speed, the horizontal velocity regulation is performed in three phases. The first phase applies when $r > 250\,\mathrm{m}$, in which the helicopter is required to attain a target horizontal velocity as $V_h \to 30\,\mathrm{m/s}$. The second phase applies when $250\,\mathrm{m} < r < 100\,\mathrm{m}$, in which the horizontal velocity of the helicopter is held constant at $V_h = 30\,\mathrm{m/s}$. The third phase applies when $r < 100\,\mathrm{m}$, in which the target horizontal velocity of the helicopter is $V_h \to V_t$. Moreover, for successful rendezvous, the helicopter's final horizontal velocity at rendezvous is required to be slightly higher than the target's ground speed.

8.3.1 Case A: Target With Constant Heading

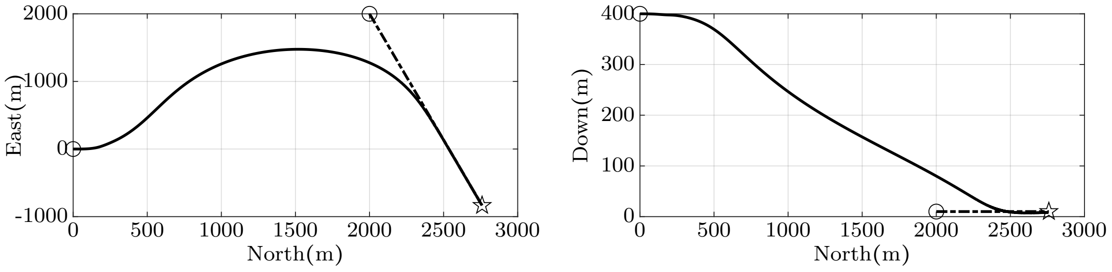

Figure 8.23: 3D positions for constant heading target, ○ Initial Position, ☆ Rendezvous Position, ——Helicopter, -·-· Target

Case A simulates a target with a constant heading angle of 120° and a constant speed of 20 m/s. The ground positions and altitude profiles for both scenarios are plotted in Fig. 8.23. The guidance laws with the chosen static gains appear to result in a pursuit-like guidance, as seen from the ground position plot. The altitude plot shows successful descent to the target altitude. The ground position and altitude profiles both depict a smooth evolution of the flight path.

The velocity vector and target parameters are plotted in Fig. 8.24. The horizontal velocity plot shows three distinct phases of deceleration terminating in a final horizontal velocity slightly greater than the target velocity. The vertical velocity plot approaches

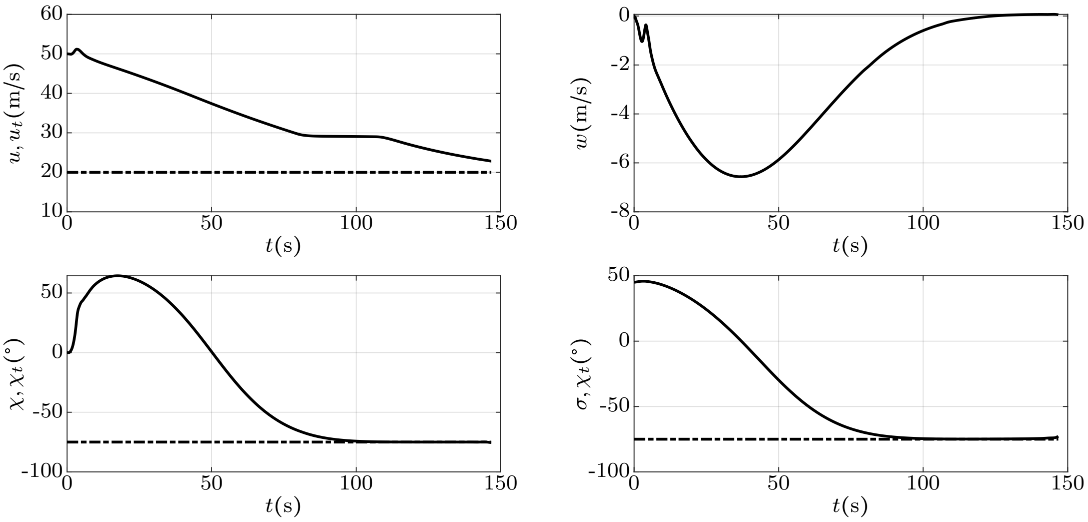

Figure 8.24: State variables for constant heading target, ——Helicopter, -·-·Target

zero well before the rendezvous point, indicating level off at the target altitude much before interception. The helicopter's ground track angle approaches the target's track angle and the horizontal line of sight simultaneously, which satisfies the necessary conditions for rendezvous.

The translational accelerations are plotted in Fig. 8.25. The forward acceleration plot depicts the three deceleration phases described earlier. The lateral acceleration demand is high in the beginning especially for the scenario that induces a reversal in the turn direction. The reversal is due to a large difference between the initial values of the horizontal line of sight angle and the helicopter ground track angle. Both the lateral and vertical accelerations converge to zero prior to the point of interception. This indicates that the helicopter achieves stable and almost stationary flight with respect to the target at rendezvous point.

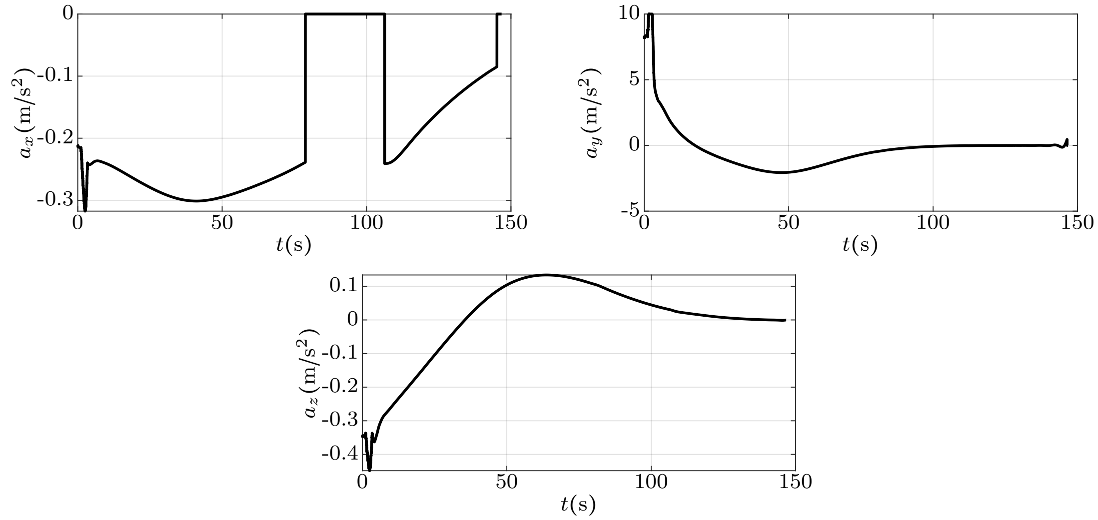

Figure 8.25: Helicopter accelerations to controller for constant heading target

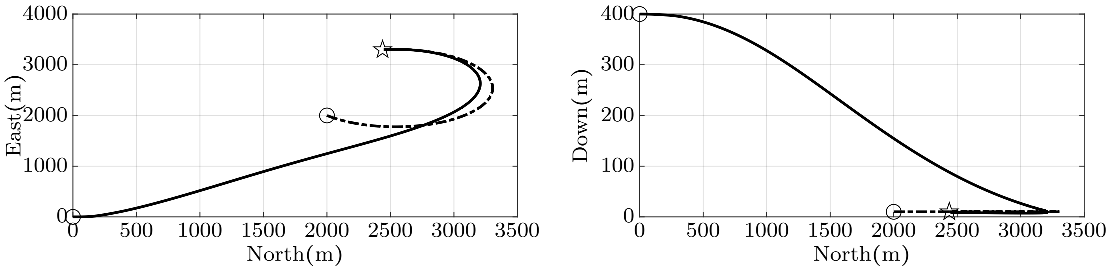

Figure 8.26: 3D positions for constant heading rate target, ○ Initial Position, ☆ Rendezvous Position, ——Helicopter, -·-·Target

8.3.2 Case B: Target with Constant Heading Rate

Case B simulates a target with constant heading rate of $\dot{\chi}_t = 1.5\,°/\mathrm{s}$, which is considerably smaller than the maximum heading rate achievable by the helicopter. The speed of the target is kept constant at 20 m/s. The ground positions and altitude profiles are plotted in Fig. 8.26. Despite being formulated and solved for a constant heading target, the guidance laws are found to robustly achieve rendezvous in the horizontal plane with a smooth evolution of the flight path. Similarly, the altitude profile shows successful descent to the target altitude.

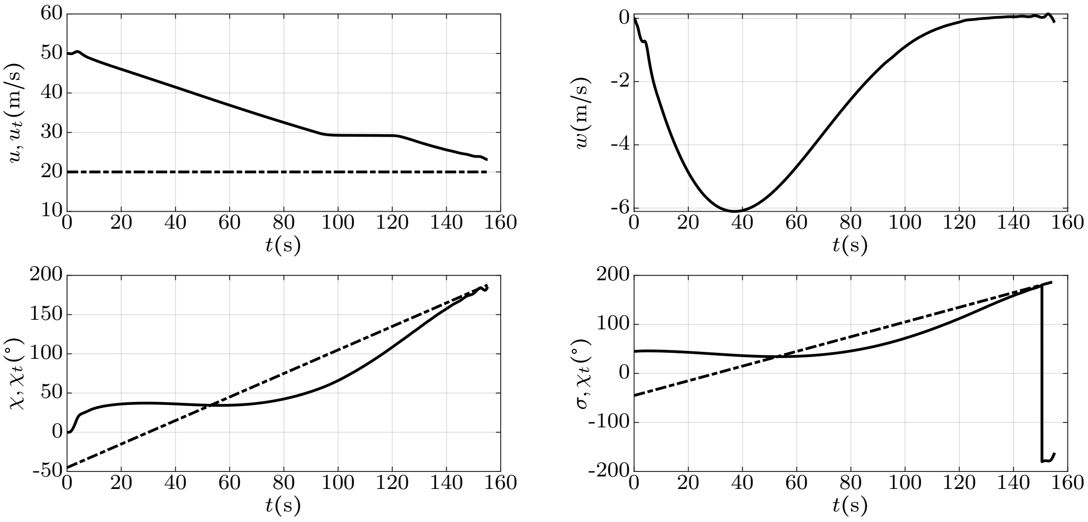

Figure 8.27: State variables for constant heading rate target, ——Helicopter, -·-·Target

The velocity vector and target parameters are plotted in Fig. 8.27. The horizontal velocity plot in red shows the three distinct deceleration phases. The vertical velocity plot in both scenarios approaches zero before the rendezvous to allow the helicopter to level off at the end of the trajectory. The helicopter's ground track angle successfully aligns with the target's track angle and the horizontal line of sight.

The translational accelerations are plotted in Fig. 8.28. The forward, lateral, and vertical accelerations approach zero towards the end of the trajectory. One outlier can be seen for the lateral acceleration plot in red, which appears to command higher values at the interception point. This behavior appears to result from a small misalignment between the horizontal line of sight and the helicopter ground track angle, as observed previously in Fig. 8.27. This indicates that although the rendezvous guidance laws

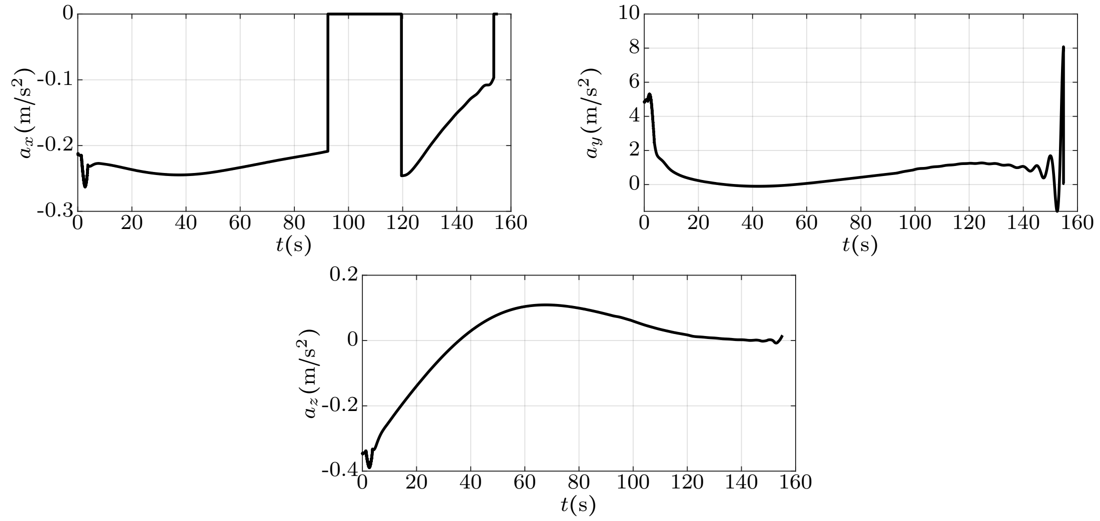

Figure 8.28: Helicopter accelerations to controller for constant heading rate target

appear to be robust to variable heading over most of the trajectory, they may lead to a large lateral acceleration demand in proximity to the target position.

8.3.3 Case C: Target With Sinusoidal Heading

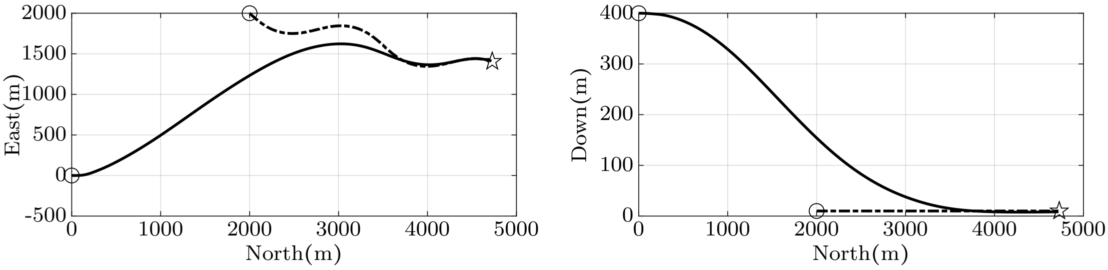

Figure 8.29: 3D positions for target with sinusoidal heading, ○ Initial Position, ☆ Rendezvous Position, ——Helicopter, -·-· Target

Case C simulates a target with a sinusoidally varying heading rate as $\dot{\chi}_t = A\sin(\omega t)$, where $A = 1.5\,^{\circ}/\mathrm{s}$ and $\omega = 0.075\,\mathrm{rad/s}$. Although this heading rate is higher than Case B, it is still much lower than the maximum heading rate achievable by the helicopter. The speed of the target is held constant at 20 m/s. The ground positions and altitude profiles for both scenarios are plotted in Fig. 8.29. The guidance laws are again found to robustly achieve rendezvous in the horizontal and vertical planes with a smooth evolution of the flight path.

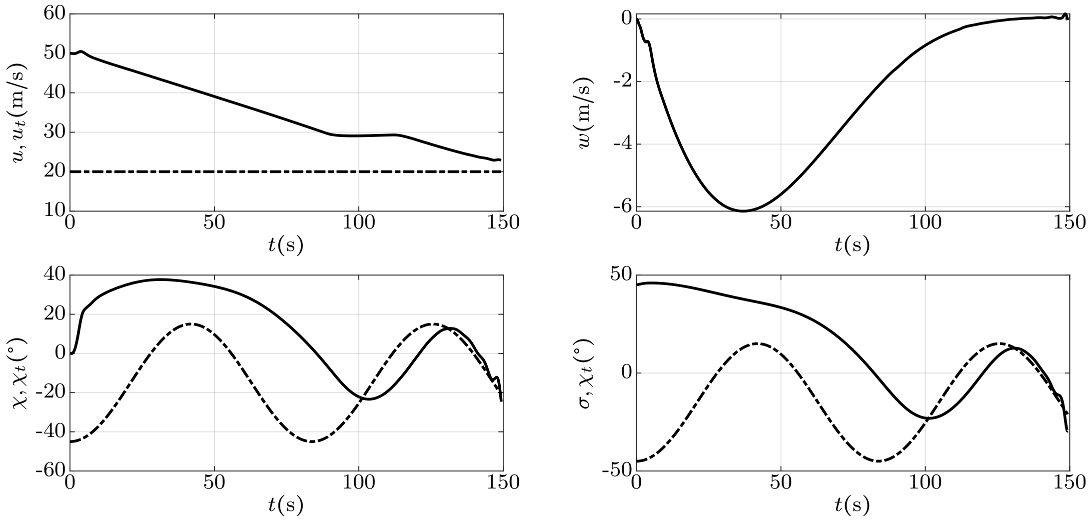

Figure 8.30: State variables for target with sinusoidal heading, ——Helicopter, -·-·Target

The velocity vector and the kinematics are plotted in Fig. 8.30. The horizontal velocity plot the three distinct deceleration phases. The helicopter's final velocity is close to the target velocity. The vertical velocity approach zero well before the rendezvous point. The track angle and horizontal line of sight plots show that the helicopter's ground track angle successfully aligns with the target's track angle and the horizontal line of sight.

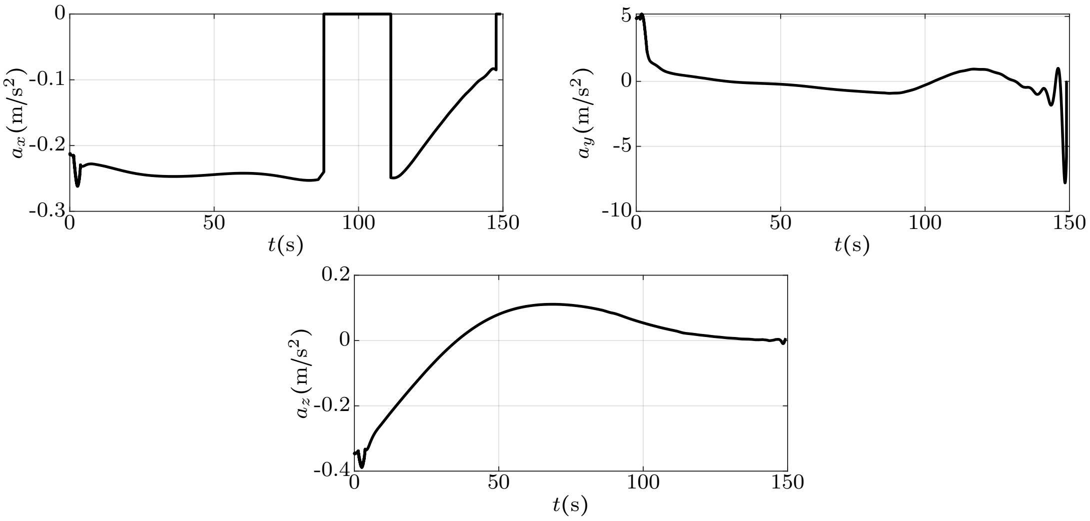

Figure 8.31: Helicopter accelerations to controller for target with sinusoidal heading

The translational accelerations are plotted in Fig. 8.31. The forward and vertical accelerations approach zero towards the end of the trajectory. However large control action is observed in the lateral acceleration plot close to the rendezvous point, which can be attributed to the guidance scheme's inability to track large target maneuvers close to the rendezvous point.

8.3.4 Case D: Target With Multisinusoidal Heading Rate

Finally, case D simulates a target whose heading rate is the sum of sinusoids of varying amplitudes and frequencies as $\dot{\chi}_t = \sum_{i=1}^{15} A_i \sin(\omega_i t + \Phi_i)$, where $A \in [1.5, 12.5]^\circ/\mathrm{s}$, $\omega \in [0.1, 1.5]\mathrm{rad/s}$, and $\Phi \in [-3, 3]\mathrm{rad}$. The lower frequency components are assigned higher amplitudes whereas the higher frequency components are assigned lower amplitudes. The speed of the target is held constant at $20\,\mathrm{m/s}$. The ground positions and altitude profiles are plotted in Fig. 8.32. Again, in both scenarios, the guidance laws are found to

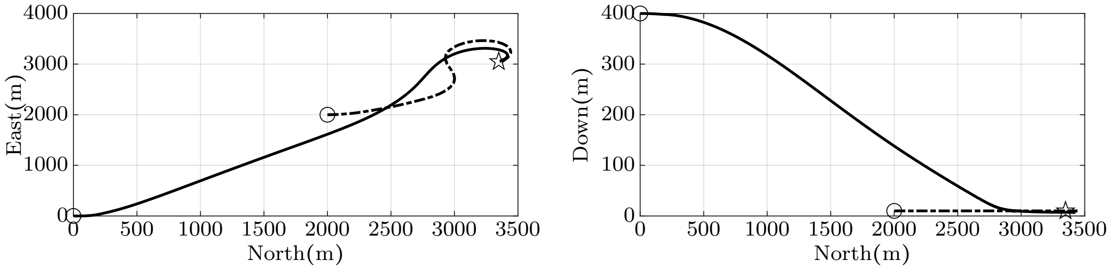

Figure 8.32: 3D positions for multisinusoidal heading rate target, ○ Initial Position, ☆ Rendezvous Position, ——Helicopter, -·- Target

achieve a successful rendezvous in both the horizontal and vertical planes. The evolution of the flight paths is also found to be smooth.

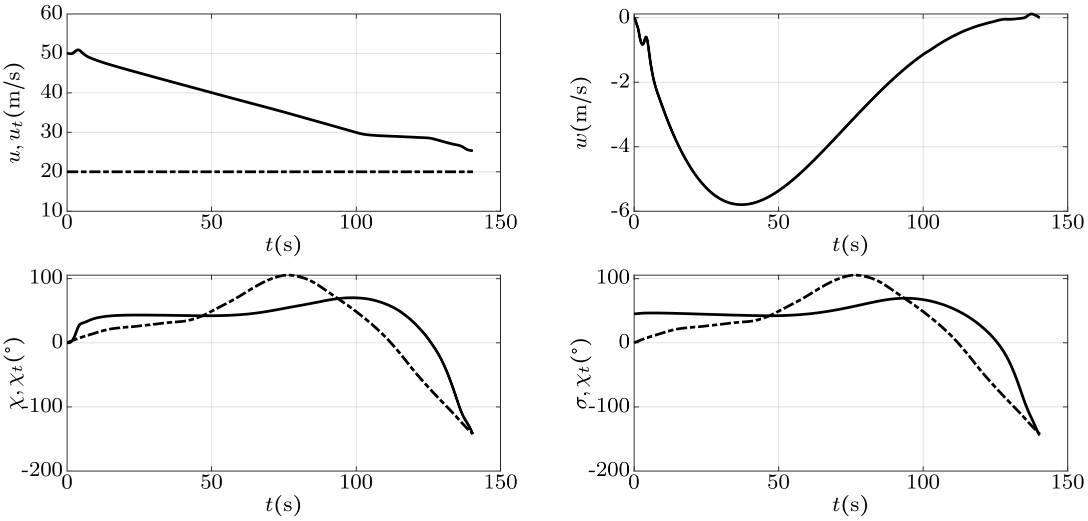

Figure 8.33: State variables for multisinusoidal heading rate target, ——Helicopter, -·- Target

The velocity vector and the kinematics are plotted in Fig. 8.33. The horizontal velocity plot indicates deceleration profiles which are less smooth than for the previous cases. This behavior stems from a variable t_{go} due to the unpredictable target maneuvers. Yet, the helicopter's final velocity is close to the target velocity in both scenarios. The

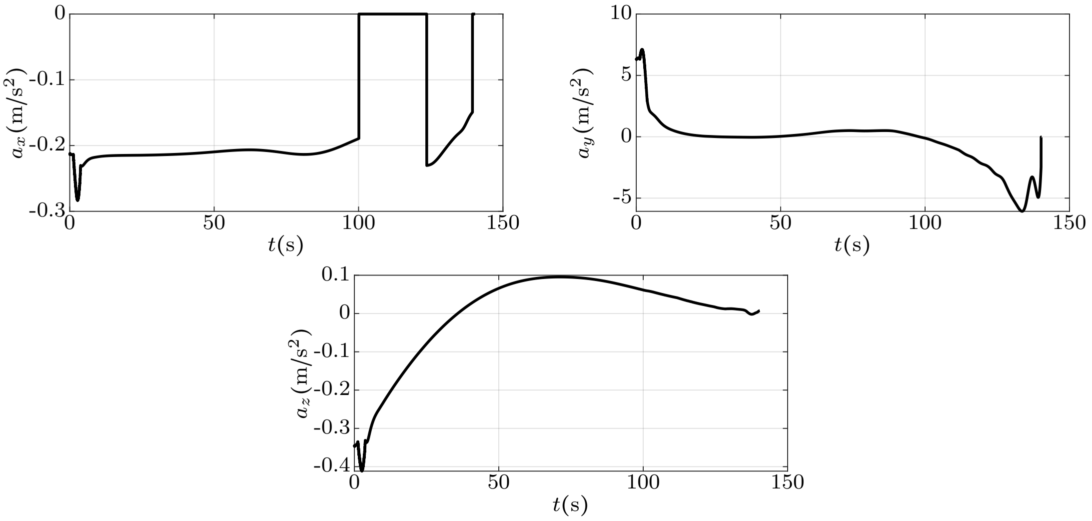

Figure 8.34: Helicopter accelerations to controller for multisinusoidal heading rate target

vertical velocities in both scenarios are smooth, and they approach zero well before the rendezvous point. The track angle and horizontal line of sight plots indicate that despite the uncertain target behavior, the helicopter is able to achieve successful rendezvous in the horizontal plane.

The translational accelerations are plotted in Fig. 8.34. The forward and vertical accelerations approach zero towards the end of the trajectory. However, non-smooth lateral acceleration profiles can be observed in both scenarios demanding non-zero control action close to the rendezvous point. Nevertheless, all three accelerations are well within their respective saturation bounds.

8.4 Shipboard Approach in High Intensity Turbulence

To demonstrate a realistic application of the rendezvous guidance laws coupled with the robust flight controller, an automatic, unpiloted approach to a moving shipboard in high intensity turbulence is chosen. This scenario allows to assess the 3D trajectory generation and tracking performance, as well as the overall robustness to turbulence in the forward flight and low-speed regimes. The helicopter-ship engagement geometry is identical to the geometry depicted previously in Sec. 7, Fig. 7.1. A ship of constant speed 10 m/s, constant course of 120°, and initial position of $(2000, 2000, 10)$m is the designated target for approach and rendezvous. The helicopter is located at $(0, 0, 400)$m, oriented along North, and in trimmed forward flight at 60 m/s. High-intensity turbulence is simulated using the CETI model (Sec. 4.3, [99]). The objective is to perform a 3D approach from the rearward direction of the ship's motion and to achieve relative hover over the landing deck.

To simplify guidance tasks, the flight phases are separated between initial approach performed in the forward flight regime, and the final approach performed in the low-speed/hover regime. In the initial approach phase, the helicopter is commanded to decelerate to 23 m/s, attain 40 m altitude, and the acquire the ship's heading. In this phase, the roll attitude commands a track angle change and the yaw rate commands turn coordination. Next, in the final approach phase, the helicopter is commanded to reach within a radius of 5 m around the ship's deck, 10 m altitude, and the acquire the ship's ground speed and heading. In this phase, the roll attitude commands lateral velocity and the yaw rate commands heading.

Fig. 8.35 shows the evolution of the horizontal and vertical paths of the ship, resulting in a successful rendezvous with the ship.

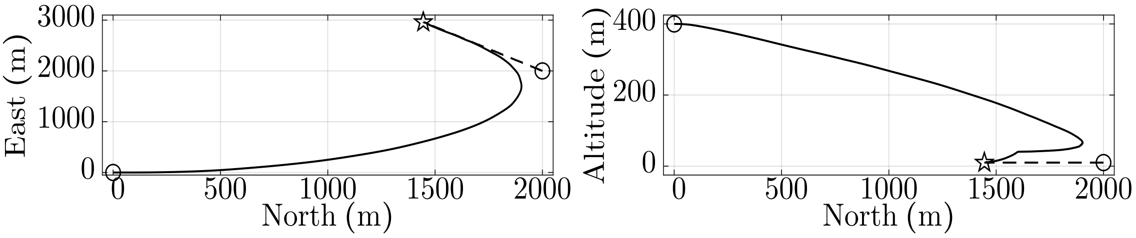

Figure 8.35: Flight paths in shipboard approach (——helicopter, - - -ship, ○ initial, ☆ final)

Fig. 8.36 plots the helicopter's states. The forward velocity (V_h) decreases gradually despite gusts affecting the pitch attitude (θ) and the pitch rate (q), and equals the ship's ground speed at rendezvous. Likewise, the helicopter ground track (χ) gradually converges upon the ship's course despite gusts affecting the roll attitude (ϕ) and the roll rate (p), and is held constant thereafter until rendezvous. A vertical speed of $-8\,\mathrm{m/s}$ for the descent is commanded during approach. Sideslip (β) remains within ±10° during arrival, but reaches upto 15° in the approach phase to compensate for the cross-track errors in this phase. The final angular rates and the final vertical speed approach zero, suggesting that the helicopter is trimmed and attains stable hover relative to the shipboard. Finally, Fig. 8.37 depicts the control inputs generated by the SMC during the entire maneuver. The pedal control approaches its upper limit during turn coordination for ground track angle control, but does not saturate. All other control

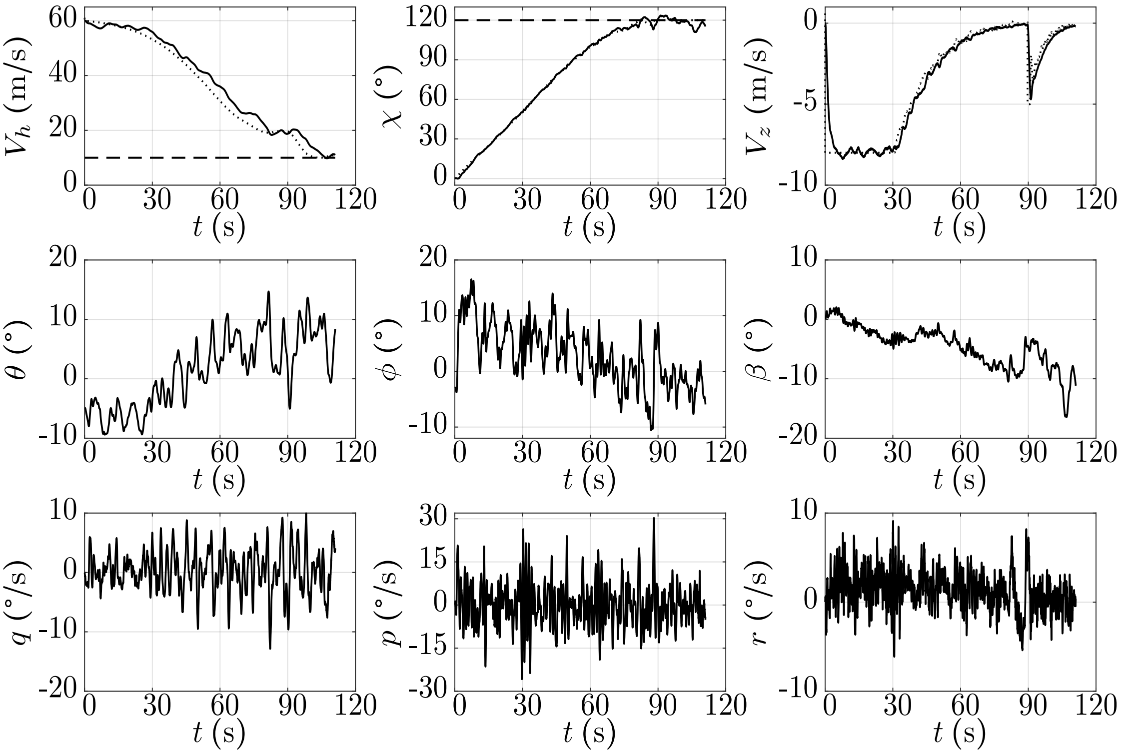

Figure 8.36: State variables in shipboard approach (····· command, —— helicopter, - - - ship)

inputs remain well within their operating margins of [0 – 100]%. In summary, the effects of turbulence and interaxis coupling are not found to adversely affect 3D trajectory tracking performance in forward flight and hover/low-speed both. Furthermore, the transition from the forward flight to low-speed mode is smooth.

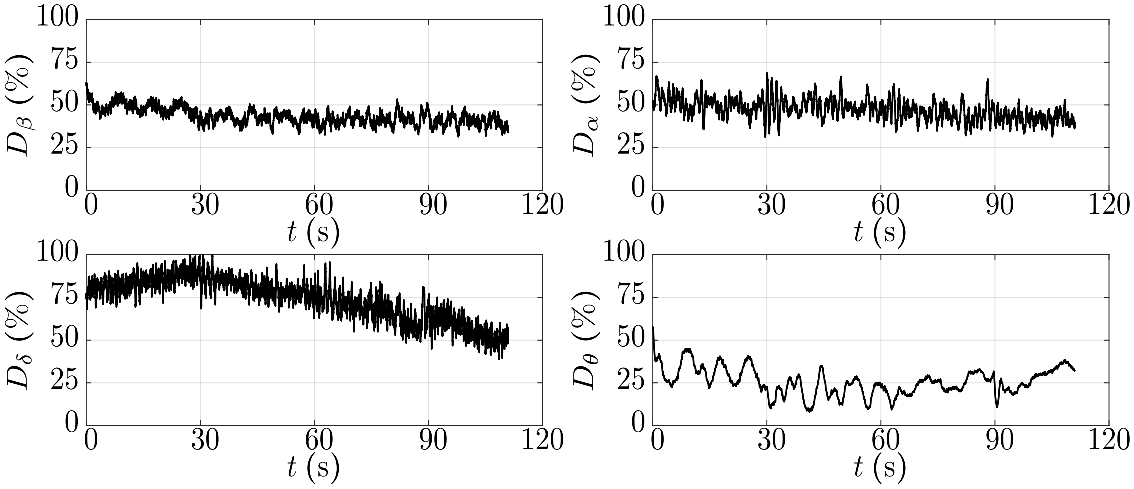

Figure 8.37: Control inputs during shipboard approach

9 Conclusions

This thesis has put forth three novel ideas with regard to helicopter guidance and control. First, the thesis proposed a sliding mode-based robust flight control design for enhancing helicopter handling qualities up to Level 1, and for enabling robust trajectory following. Second, the thesis demonstrated the application of the state-dependent Riccati equation technique to solve an online trajectory generation problem between waypoints with velocity vector constraints. Finally, the thesis extended the state-dependent Riccati equation approach for a scenario of rendezvous with a slow maneuvering target.

The key findings, advantages, and shortcomings of the work performed in this thesis are now summarized in the following points:

1. The proposed sliding mode flight controller satisfies the required on-axis behavior and tracking performance, as well as robustness to interaxis coupling and exogenous disturbances in a highly nonlinear and coupled system. In this sense, the need for explicit axes decoupling necessitated by some contemporary control techniques was obviated. The flight controller was implemented in a dual-loop architecture and the overall closed-loop system was proved to be stable. The helicopter with SMC controller achieved Level 1 HQs in terms of attitude quickness and interaxis coupling criteria, and it satisfied adequate performances in the slalom, acceleration/deceleration and bob-up/bob-down MTEs. Stability was also maintained in large amplitude attitudes that required high angular rates. The chattering effect, which is characteristic of the classical SMC technique, was effectively mitigated

using the boundary layer concept. The inclusion of optional PCH layers for reference command adaptation was shown to reduce overshoot and to mitigate actuator saturations in the slalom maneuver. Furthermore, a comparative assessment of the SMC flight controller was performed with an EMF controller synthesized from the literature. The SMC controller showed advantages particularly in performance against the interaxis coupling criteria. Some of the benefits of the sliding mode controller can be summarized as follows:

a) It has a low dependency on system models, which can potentially reduce costs and efforts in practical flight control development.

b) It satisfies the required closed-loop performance specification in the form of the required axial response-types specified as transfer functions.

c) It provides a mathematical basis for stability in the presence of the uncertainties, insofar as the upper bounds of the uncertainties can be estimated, and the uncertainties can be overcome by control action.

d) The closed-form solution is obtained as simple, high gain PID-like feedback structure (within the boundary layer) and does not impose any additional computational effort. The closed-form controller being deterministic, it is also well-suited to satisfy many of the operational performance standards and certification requirements applicable to airborne platforms.

Despite these strengths, the proposed flight controller has the following limitations:

a) The PCH layers were found to slightly reduce agility and proper tuning was required to avoid degrading the overall handling qualities. This behavior occurs because the PCH layers introduce additional dynamics in the closed-loop, which, although stable in nature, increase the command tracking delays.

b) The SMC controller was designed using a 6DOF rigid-body dynamic model, which assumes quasi-steady rotor dynamics. This means that steady-state effects of the rotor modes are directly absorbed into the stability and control derivatives of the rigid body model. Although the resulting controller did not lead to instability in the rotor dynamics (particularly in the lead-lag states which are lowly damped), the higher frequency rotor dynamics could not be explicitly and directly accounted for in the control law synthesis.

c) The sliding mode gains were chosen based on the worst case scenario that represent upper bounds of the uncertainties. It is known that for helicopter flight control, high gains on the angular rate feedback tend to amplify the high frequency modes, and may also lead to instability.

d) Finally, the SMC controller does not explicitly account for constraints on the control inputs and on the state variables, an aspect that may be required to assure flight envelope protection.

2. With regard to the SDRE-based waypoint guidance, the principle of axis decoupling was applied to reduce the dimensionality and thereby ease the computational complexity of the state tracking problem. Three independent, nonlinear regulator problems were solved analytically to obtain closed-form control laws for translational accelerations. The limiting horizontal and vertical distances for convergence to the terminal velocity vector constraints were analyzed, and it was shown that the trajectory generation problem converges for all cases where the distance to the next waypoint is greater than the minimum distance. The minimum distance was shown to be a function of the helicopter's performance thresholds. The feasibility of generating trajectories online was demonstrated in a closed-loop by coupling it with the sliding mode controller and a comprehensive full-scale helicopter simulation model. The simulation results using a two-waypoint scenario as well as a sequence of 3D waypoints with different altitude and velocity constraints showed smooth evolutions of the flight path, and the state and control trajectories. Due to

its low computational cost, the proposed approach can potentially simplify guidance command generation in manned and unmanned rotary wing platforms for tactical and maritime missions. However, a major drawback of the proposed approach is that the constraints on the state and control variables, such as flight envelope protection, are not addressed in the guidance law synthesis.

3. The proposed rendezvous guidance scheme was formulated using the actual target information for generating the required translational accelerations. The translational accelerations were also obtained as deterministic, closed-form solutions. This obviates the need for pre-computed reference trajectories. The feasibility of the proposed rendezvous guidance scheme was demonstrated by coupling it with the sliding mode controller and a comprehensive full-scale helicopter simulation model. A 2D target motion was simulated as a constant speed and constant heading. Additional cases were evaluated to determine its robustness for different target maneuvers: constant heading rate, sinusoidal heading rate, and multi-sinusoidal heading rate. In all cases, the rendezvous guidance laws coupled to the sliding mode controller were able to accurately track the required accelerations and achieve rendezvous with the target. Although the rendezvous guidance laws were robust to variable target lateral maneuvers, their performance was found to degrade for larger target maneuvers. In particular, the performance was found to worse if the target has large maneuvers when the helicopter is in proximity to the target location. The lack of state and control constraints is also a drawback of the proposed rendezvous guidance.

10 Recommendations for Future Work

This chapter proposes some recommendations for extending the present work in order not only to to introduce newer features, but also to overcome some drawbacks that have been identified, as well as measures to improve its practical suitability.

1. While the sliding mode control technique is known to be robust to uncertainties, demonstrating its robustness to sensor and actuator faults can improve its practical suitability for the helicopter flight control problem. For this purpose, the reader is referred to previous works on sliding mode-based fault tolerant schemes [42, 43], which can be a good starting point for fault tolerant helicopter flight control.
2. The present sliding mode control used fixed sliding gains based on the uncertainty estimates. As mentioned earlier, this choice is designed for the worst case scenario. However, high gains are not required when the uncertainties are small, such as in calm wind conditions, or when accurate system models are available *a priori*. For this purpose, adaptation-based approaches for tuning the sliding mode gains based on the actual uncertainty bounds may prove useful and alleviate some of the drawbacks observed in the present approach. Such adaptive gain tuning would also obviate the need for the pseudo-control hedging layers in the closed-loop structure. A recent work [105] has introduced new methodologies for adaptive sliding mode control, which provides a strong mathematical basis for the development of an adaptation sliding mode helicopter flight control.

3. The high frequency chattering effect of the present sliding mode control approach is perhaps the most undesirable of all, especially when dealing with mechanical systems. Although the boundary layer approach pursued in this thesis showed good results, it leads to a pseudo-sliding mode control, in which the inherent robustness properties of sliding mode control stand degraded. Notably, the closed-loop does not become completely insensitive to uncertainty and an ideal sliding motion no longer takes place inside the boundary layer. It has been shown in the literature [106] that resorting to the so-called higher-order sliding mode control approach not only mitigates chattering while retaining all robustness properties, but also permits its application to systems whose relative degree with respect to the sliding variable is greater than one. It is therefore recommended to pursue helicopter flight control based on the higher-order sliding mode control approach.

4. With regard to the trajectory generation guidance laws, further extensions may be envisaged by explicitly including state and control limits in the synthesis of the guidance laws. This feature will allow the trajectories to avoid sensed obstacles, no-fly zones, and also ensure that the trajectories lie within the helicopter's flight envelope.

5. The present dissertation has provided a basis to demonstrate the efficacy and mathematical framework for nonlinear control and guidance algorithms. Avionics software development and integration in accordance with the minimum operational performance standards remains an important aspect that was clearly beyond the scope of this work. For any subsequent implementation on airborne platforms, it will be necessary to pursue further development and demonstrate compliance with applicable certification specifications (for instance, Ref. [8]).

Bibliography

[1] G. D. Padfield, *Helicopter Flight Dynamics*, 1st ed. John Wiley & Sons, Ltd, 2007.

[2] G. E. Cooper and R. P. Harper Jr, "The Use of Pilot Rating in the Evaluation of Aircraft Handling Qualities," NATO Advisory Group for Aerospace Research and Development, Neuilly-Sur-Seine, France, Tech. Rep., 1969.

[3] P. H. Lehmann, M. Jones, and M. Höfinger, "Impact of Turbulence and Degraded Visual Environment on Pilot Workload," *CEAS Aeronautical Journal*, vol. 8, no. 3, pp. 413–428, 2017. doi: 10.1007/s13272-017-0246-3

[4] B. J. Baskett, "Aeronautical Design Standard - Performance Specification - Handling Qualities Requirements for Military Rotorcraft," US Army Aviation and Missile Command, Redstone Arsenal, Alabama, USA, Tech. Rep. ADS-33E-PRF, 2000.

[5] W. L. Garrard, E. Low, and S. Prouty, "Design of Attitude and Rate Command Systems for Helicopters Using Eigenstructure Assignment," *Journal of Guidance, Control, and Dynamics*, vol. 12, no. 6, pp. 783–791, 1989. doi: 10.2514/3.20482

[6] P. G. Hamel and J. Kaletka, "Advances in Rotorcraft System Identification," *Progress in Aerospace Sciences*, vol. 33, no. 3-4, pp. 259–284, 1997. doi: 10.1016/S0376-0421(96)00005-X

[7] R. T. N. Chen, J. V. Lebacqz, E. W. Aiken, and M. B. Tischler, "Helicopter Mathematical Models and Control Law Development for Handling Qualities Research," *NASA/Army Rotorcraft Technology: Material and Structures, Propulsion and Drive Systems, Flight Dynamics and Control, and Acoustics*, vol. 2, pp. 837–899, 1988.

[8] Anon., "Certification Specifications and Acceptable Means of Compliance for Large Rotorcraft," European Aviation Safety Agency, Tech. Rep. CS–29, Amendment 7, 2019.

[9] R. H. Hoh and I. L. Ashkenas, "Development of VTOL Flying Qualities Criteria for Low Speed and Hover," Naval Air Development Center, Warminster, Pennsylvania, USA, Tech. Rep. NADC-77052-30, 1979.

[10] G. L. Soneson, J. F. Horn, and A. Zheng, "Simulation Testing of Advanced Response Types for Ship-based Rotorcraft," *Journal of the American Helicopter Society*, vol. 61, no. 3, pp. 1–13, 2016. doi: 10.4050/JAHS.61.032011

[11] P. Perfect, M. Jump, and M. D. White, "Handling Qualities Requirements for Future Personal Aerial Vehicles," *Journal of Guidance, Control, and Dynamics*, vol. 38, no. 12, pp. 2386–2398, 2015. doi: 10.2514/1.G001073

[12] F. Kendoul, "Survey of Advances in Guidance, Navigation, and Control of Unmanned Rotorcraft Systems," *Journal of Field Robotics*, vol. 29, no. 2, pp. 315–378, 2012. doi: 10.1002/rob.20414

[13] M. Whalley and J. Howitt, "Optimization of Partial Authority Automatic Flight Control Systems for Hover/Low-speed Maneuvering in Degraded Visual Environments," *Journal of the American Helicopter Society*, vol. 47, no. 2, pp. 79–89, 2002. doi: 10.4050/JAHS.47.79

[14] K. T. Christensen, K. G. Campbell, C. D. Griffith, C. M. Ivler, M. B. Tischler, and J. W. Harding, "Flight Control Development for the ARH-70 Armed Reconnaissance Helicopter Program," in *American Helicopter Society 63rd Annual Forum*, Virginia Beach, Virginia, USA, 2007.

[15] M. B. Tischler, C. L. Blanken, K. K. Cheung, M. S. S. Sean, V. Sahasrabudhe, and A. Faynberg, "Modernized Control Laws for UH-60 BLACK HAWK Optimization and Flight-Test Results," *Journal of Guidance, Control, and Dynamics*, vol. 28, no. 5, pp. 964–978, 2005. doi: 10.2514/1.8021

[16] B. T. Fujizawa, M. B. Tischler, C. R. Ott, and C. L. Blanken, "UH-60 Partial Authority Modernized Control Laws for Improved Handling Qualities in the Degraded Visual Environment," in *American Helicopter Society 70th Annual Forum*, Montréal, Québec, Canada, 2014.

[17] T. Clarke, J. Ensor, and S. J. Griffin, "Desirable Eigenstructure for Good Short-term Helicopter Handling Qualities: The Attitude Command Response Case," *Proceedings of the Institution of Mechanical Engineers, Part G: Journal of Aerospace Engineering*, vol. 217, no. 1, pp. 43–56, 2003. doi: 10.1243/095441003763031824

[18] S. Srinathkumar, "Rotorcraft Precision Hover Control in Atmospheric Turbulence via Eigenstructure Assignment," *Journal of the American Helicopter Society*, vol. 64, no. 1, pp. 1–12, 2019. doi: 10.4050/JAHS.64.012005

[19] J. Liceaga-Castro, C. Verde, J. O'Reilly, and W. E. Leithead, "Helicopter Flight Control Using Individual Channel Design," *IEE Proceedings-Control Theory and Applications*, vol. 142, no. 1, pp. 58–72, 1995. doi: 10.1049/ip-cta:19951575

[20] M. Vijaya Kumar, P. Sampath, S. Suresh, S. N. Omkar, and R. Ganguli, "Neural Network Based Feedback Error Controller for Helicopter," *Aircraft En-*

gineering and Aerospace Technology, vol. 83, no. 5, pp. 283–295, 2011. doi: 10.1108/00022661111159898

[21] P. Simplício, M. Pavel, E. Van Kampen, and Q. Chu, "An Acceleration Measurements-based Approach for Helicopter Nonlinear Flight Control Using Incremental Nonlinear Dynamic Inversion," *Control Engineering Practice*, vol. 21, no. 8, pp. 1065–1077, 2013. doi: 10.1016/j.conengprac.2013.03.009

[22] M. D. Pavel, P. Shanthakumaran, Q. Chu, O. Stroosma, M. Wolfe, and H. Cazemier, "Incremental Nonlinear Dynamic Inversion for the Apache AH-64 Helicopter Control," *Journal of the American Helicopter Society*, vol. 65, no. 2, pp. 1–16, 2020. doi: 10.4050/JAHS.65.022006

[23] T. D. Ngo and C. Sultan, "Model Predictive Control for Helicopter Shipboard Operations in the Ship Airwakes," *Journal of Guidance, Control, and Dynamics*, vol. 38, no. 12, pp. 574–589, 2015. doi: 10.2514/1.G001243

[24] W. B. Greer and C. Sultan, "Shrinking Horizon Model Predictive Control Method for Helicopter–Ship Touchdown," *Journal of Guidance, Control, and Dynamics*, vol. 43, no. 5, pp. 884–900, 2020. doi: 10.2514/1.G004374

[25] I. Postlethwaite, A. Smerlas, D. J. Walker, A. W. Gubbels, S. W. Baillie, M. E. Strange, and J. Howitt, "H_∞ Control of the NRC Bell 205 Fly-by-Wire Helicopter," *Journal of the American Helicopter Society*, vol. 44, no. 4, pp. 276–284, 1999. doi: 10.4050/JAHS.44.276

[26] A. J. Smerlas, D. J. Walker, I. Postlethwaite, M. E. Strange, J. Howitt, and A. W. Gubbels, "Evaluating H_∞ Controllers on the NRC Bell 205 Fly-by-wire Helicopter," *Control Engineering Practice*, vol. 9, no. 1, pp. 1–10, 2001. doi: 10.1016/S0967-0661(00)00088-5

[27] E. Prempain and I. Postlethwaite, “Static H_∞ Loop Shaping Control of a Fly-by-wire Helicopter,” *Automatica*, vol. 41, no. 9, pp. 1517–1528, 2005. doi: 10.1016/j.automatica.2005.04.001

[28] S. Geluardi, J. Venrooij, M. Olivari, H. H. Bülthoff, and L. Pollini, “Transforming Civil Helicopters into Personal Aerial Vehicles: Modeling, Control, and Validation,” *Journal of Guidance, Control, and Dynamics*, vol. 40, no. 10, pp. 2481–2495, 2017. doi: 10.2514/1.G002605

[29] Z. Mirfakhraie and W. L. Garrard, “Design of a Helicopter Control System to Meet Handling Quality Specifications Using H_∞ Techniques,” in *Proceedings of the First IEEE Regional Conference on Aerospace Control Systems.* Westlake Village, CA, USA: IEEE, May 1993, pp. 299–303. doi: 10.1109/AEROCS.1993.720946

[30] M. C. Turner, D. J. Walker, and A. G. Alford, “Design and Ground-based Simulation of an H_∞ Limited Authority Flight Control System for the Westland Lynx Helicopter,” *Aerospace Science and Technology*, vol. 5, no. 3, pp. 221–234, 2001. doi: 10.1016/S1270-9638(01)01093-8

[31] D. Lee and J. F. Horn, “Simulation of Pilot Workload for a Helicopter Operating in a Turbulent Ship Airwake,” *Proceedings of the Institution of Mechanical Engineers, Part G: Journal of Aerospace Engineering*, vol. 219, no. 5, pp. 445–458, 2005.

[32] J. F. Horn, D. O. Bridges, and D. Lee, “Flight Control Design for Alleviation of Pilot Workload During Helicopter Shipboard Operations,” in *American Helicopter Society 62nd Annual Forum*, Phoenix, AZ, USA, May 2006.

[33] J. Howitt, M. E. Strange, G. J. W. Dudgeon, , and M. S. Whalley, “Flight Control Development for the ARH-70 Armed Reconnaissance Helicopter Program,” in *American Helicopter Society 54th Annual Forum*, Washington, D.C., USA, May 1998.

[34] S. Baillie, J. M. Morgan, D. Mitchell, and R. Hoh, "The Use of Limited Authority Response Types to Improve Helicopter Handling Qualities During Flight in Degraded Visual Environments," *Journal of the American Helicopter Society*, vol. 42, no. 1, pp. 89–95, 1997. doi: 10.4050/JAHS.42.89

[35] M. A. Manness, J. J. Gribble, and D. J. Murray-Smith, "Multivariable Methods for Helicopter Flight Control Law Design: A Review," in *European Rotorcraft Forum*, Glasgow, UK, September 1990.

[36] J. Hu and H. Gu, "Survey on Flight Control Technology for Large-Scale Helicopter," *International Journal of Aerospace Engineering*, vol. 2017, 2017.

[37] D. G. Mitchell and R. H. Hoh, "Development of Time Response Criteria for Rotorcraft at Hover and Low Speed," in *12th Atmospheric Flight Mechanics Conference*, Snowmass, CO, USA, August 1985. doi: https://doi.org/10.2514/6.1985-1790

[38] C. Edwards and S. Spurgeon, *Sliding Mode Control: Theory and Applications.* CRC Press, 1998.

[39] S. R. Kumar, S. Rao, and D. Ghose, "Nonsingular Terminal Sliding Mode Guidance with Impact Angle Constraints," *Journal of Guidance, Control, and Dynamics*, vol. 37, no. 4, pp. 1114–1130, 2014. doi: 10.2514/1.62737

[40] Y. Shtessel, C. Hall, and M. Jackson, "Reusable Launch Vehicle Control in Multiple-Time-Scale Sliding Modes," *Journal of Guidance, Control, and Dynamics*, vol. 23, no. 6, pp. 1013–1020, 2000. doi: 10.2514/2.4669

[41] S. R. Wells and R. A. Hess, "Multi-Input/Multi-Output Sliding Mode Control for a Tailless Fighter Aircraft," *Journal of Guidance, Control, and Dynamics*, vol. 26, no. 3, pp. 463–473, 2003. doi: 10.2514/2.5084

[42] Y. Shtessel, J. Buffington, and S. Banda, "Multiple Timescale Flight Control Using Reconfigurable Sliding Modes," *Journal of Guidance, Control, and Dynamics*, vol. 22, no. 6, pp. 873–883, 1999. doi: 10.2514/2.4465

[43] R. A. Hess and S. R. Wells, "Sliding Mode Control Applied to Reconfigurable Flight Control Design," *Journal of Guidance, Control, and Dynamics*, vol. 26, no. 3, pp. 452–462, 2003. doi: 10.2514/2.5083

[44] A. J. Fossard, "Helicopter Control Law Based on Sliding Mode with Model Following," *International Journal of Control*, vol. 57, no. 5, pp. 1221–1235, 1993. doi: 10.1080/00207179308934442

[45] S. Spurgeon, C. Edwards, and N. P. Foster, "Robust Model Reference Control Using a Sliding Mode Controller/Observer Scheme with Application to a Helicopter Problem," in *IEEE International Workshop on Variable Structure Systems.* Tokyo, Japan: IEEE, 1996. doi: 10.1109/VSS.1996.578542

[46] D. McGeoch, E. McGookin, and S. Houston, "MIMO Sliding Mode Attitude Command Flight Control System For a Helicopter," in *AIAA Guidance, Navigation, and Control Conference and Exhibit*, San Francisco, California, 2005. doi: 10.2514/6.2005-6350

[47] E. Medagoda and P. Gibbens, "Synthetic-Waypoint Guidance Algorithm for Following a Desired Flight Trajectory," *Journal of Guidance, Control, and Dynamics*, vol. 33, no. 2, pp. 601–606, 2010. doi: 10.2514/1.46204

[48] C. Goerzen, Z. Kong, and B. Mettler, "A Survey of Motion Planning Algorithms from the Perspective of Autonomous UAV Guidance," *Journal of Intelligent and Robotic Systems*, vol. 57, no. 1, pp. 65–100, 2009. doi: 10.1007/s10846-009-9383-1

[49] G. Hoffmann, S. Waslander, and C. Tomlin, "Quadrotor Helicopter Trajectory Tracking Control," in *AIAA Guidance, Navigation and Control Conference.* Hon-

olulu, HI, USA: American Institute of Aeronautics and Astronautics, August 2008, pp. AIAA 2008–7410. doi: 10.2514/6.2008-7410

[50] E. P. Anderson, R. W. Beard, and T. W. McLain, “Real-Time Dynamic Trajectory Smoothing for Unmanned Air Vehicles,” *IEEE Transactions on Control Systems Technology*, vol. 13, no. 3, pp. 471–477, 2005.

[51] S. Choudhury and S. Scherer, “The Dynamics Projection Filter (DPF) – Real-time Nonlinear Trajectory Optimization using Projection Operators,” in *IEEE International Conference on Robotics and Automation.* Seattle, WA, USA: IEEE, May 2015, pp. 644–649. doi: 10.1109/ICRA.2015.7139247

[52] M. Beul and S. Behnke, “Analytical Time-optimal Trajectory Generation and Control for Multirotors,” in *IEEE International Conference on Unmanned Aircraft Systems.* Arlington, VA, USA: IEEE, July 2016, pp. 87–96. doi: 10.1109/ICUAS.2016.7502532

[53] D. Mellinger and V. Kumar, “Minimum Snap Trajectory Generation and Control for Quadrotors,” in *IEEE International Conference on Robotics and Automation.* Shanghai, China: IEEE, May 2011, pp. 2520–2525. doi: 10.1109/ICRA.2011.5980409

[54] A. Bry, C. Richter, A. Bachrach, and N. Roy, “Aggressive Flight of Fixed-wing and Quadrotor Aircraft in Dense Indoor Environments,” *The International Journal of Robotics Research*, vol. 34, no. 7, pp. 969–1002, 2015. doi: 10.1177/0278364914558129

[55] T. Lapp and L. Singh, “Model Predictive Control Based Trajectory Optimization for Nap-Of-The-Earth (NOE) Flight Including Obstacle Avoidance,” in *Proceedings of the American Control Conference.* Boston, MA, USA: IEEE, June 2004, pp. 891–896. doi: 10.23919/ACC.2004.1383719

[56] H. J. Kim, D. H. Shim, and S. Sastry, “Nonlinear Model Predictive Tracking Control for Rotorcraft- Based Unmanned Aerial Vehicles,” in *Proceedings of the American Control Conference.* Anchorage, AK, USA: IEEE, May 2002, pp. 3576–3581. doi: 10.1109/ACC.2002.1024483

[57] R. C. Shekhar, M. Kearney, and I. Shames, “Robust Model Predictive Control of Unmanned Aerial Vehicles Using Waysets,” *Journal of Guidance, Control, and Dynamics*, vol. 38, no. 10, pp. 1898–1907, 2015. doi: 10.2514/1.G000787

[58] M. Neunert, C. De Crousaz, F. Furrer, M. Kamel, F. Farshidian, R. Siegwart, and J. Buchli, “Fast Nonlinear Model Predictive Control for Unified Trajectory Optimization and Trackings,” in *IEEE International Conference on Robotics and Automation.* Stockholm, Sweden: IEEE, June 2016, pp. 1398–1404. doi: 10.1109/ICRA.2016.7487274

[59] C. L. Bottasso, D. Leonello, and B. Savini, “Path Planning for Autonomous Vehicles by Trajectory Smoothing Using Motion Primitives,” *IEEE Transactions on Control Systems Technology*, vol. 16, no. 6, pp. 1152–1168, 2008.

[60] M. Brezak and I. Petrovic, “Real-Time Approximation of Clothoids with Bounded Error for Path Planning Applications,” *IEEE Transactions on Robotics*, vol. 30, no. 2, pp. 507–515, 2014. doi: 10.1109/TRO.2013.2283928

[61] D. Jung and P. Tsiotras, “On-line Path Generation for Unmanned Aerial Vehicles using B-spline Path Templates,” *Journal of Guidance, Control, and Dynamics*, vol. 36, no. 6, pp. 1642–1653, 2013. doi: 10.2514/1.60780

[62] S. B. Mehdi, R. Choe, V. Cichella, and N. Hovakimyan, “Collision Avoidance Through Path Replanning Using Bézier Curves,” in *AIAA Guidance, Navigation and Control Conference.* Kissimmee, FL, USA: American Institute of Aeronautics and Astronautics, January 2015, pp. AIAA 2015–0598. doi: 10.2514/6.2015-0598

[63] S. Upadhyay and A. Ratnoo, "Smooth Path Planning for Unmanned Aerial Vehicles with Airspace Restrictions," *Journal of Guidance, Control, and Dynamics*, vol. 40, no. 7, pp. 1596–1612, 2017. doi: 10.2514/1.G002400

[64] A. R. Babaei and M. Mortazavi, "Three-Dimensional Curvature-Constrained Trajectory Planning Based on In-Flight Waypoints," *Journal of Aircraft*, vol. 47, no. 4, pp. 1391–1398, 2010. doi: 10.2514/1.47711

[65] S. Di Cairano, H. Park, and I. Kolmanovsky, "Model Predictive Control Approach for Guidance of Spacecraft Rendezvous and Proximity Maneuvering," *International Journal of Robust and Nonlinear Control*, vol. 22, no. 12, pp. 1398–1427, 2012.

[66] L. S. Breger and J. P. How, "Safe Trajectories for Autonomous Rendezvous of Spacecraft," *Journal of Guidance, Control, and Dynamics*, vol. 31, no. 5, pp. 1478–1489, 2008. doi: 10.2514/1.29590

[67] M. Hawkins, Y. Guo, and B. Wie, "Spacecraft Guidance Algorithms for Asteroid Intercept and Rendezvous Missions," *International Journal of Aeronautical and Space Sciences*, vol. 13, no. 2, pp. 154–169, 2012. doi: 10.5139/IJASS.2012.13.2.154

[68] C.-K. Ryoo, H. Cho, and M.-J. Tahk, "Optimal Guidance Laws with Terminal Impact Angle Constraint," *Journal of Guidance, Control, and Dynamics*, vol. 28, no. 4, pp. 724–732, 2005. doi: 10.2514/1.8392

[69] H. Oh, S. Kim, H.-S. Shin, B. A. White, A. Tsourdos, and C. A. Rabbath, "Rendezvous and Standoff Target Tracking Guidance Using Differential Geometry," *Journal of Intelligent & Robotic Systems*, vol. 69, no. 1-4, pp. 389–405, 2013. doi: 10.1007/s10846-012-9751-0

[70] N. Regina and M. Zanzi, "UAV Guidance Law for Ground-based Target Trajectory Tracking and Loitering," in *IEEE Aerospace Conference.* Big Sky, Montana, USA: IEEE, 2011. doi: 10.1109/AERO.2011.5747522

[71] T. Yamasaki and S. N. Balakrishnan, "Sliding Mode-based Pure Pursuit Guidance for Unmanned Aerial Vehicle Rendezvous and Chase with a Cooperative Aircraft," *Proceedings of the Institution of Mechanical Engineers, Part G: Journal of Aerospace Engineering*, vol. 224, no. 10, pp. 1057–1067, 2010. doi: 10.1243/09544100JAERO768

[72] A. Ratnoo, "Variable Deviated Pursuit for Rendezvous Guidance," *Journal of Guidance, Control, and Dynamics*, vol. 38, no. 4, pp. 787–792, 2015.

[73] A. L. Smith, "Proportional Navigation with Adaptive Terminal Guidance for Aircraft Rendezvous," *Journal of Guidance, Control, and Dynamics*, vol. 31, no. 6, pp. 1832–1836, 2008. doi: 10.2514/1.33535

[74] A. Tsukerman, M. Weiss, T. Shima, D. Löbl, and F. Holzapfel, "Optimal Rendezvous Guidance Laws with Application to Civil Autonomous Aerial Refueling," *Journal of Guidance, Control, and Dynamics*, vol. 41, no. 5, pp. 1167–1174, 2018. doi: 10.2514/1.G003154

[75] M. Voskuijl, G. D. Padfield, D. J. Walker, B. J. Manimala, and A. W. Gubbels, "Simulation of Automatic Helicopter Deck Landings Using Nature Inspired Flight Control," *Aeronautical Journal*, vol. 114, no. 1151, pp. 25–34, 2010.

[76] D. C. Bradley, M. Downes, and R. B. Lumsden, "The Development and Flight Test Demonstration of an Integrated Automatic Recovery System to Reduce the Operational Limitations of Embarked Helicopters at Night and in Bad Weather," in *American Helicopter Society 51st Annual Forum*, 1995.

[77] J. F. Horn, J. Yang, C. He, D. Lee, and J. K. Tritschler, “Autonomous Ship Approach and Landing using Dynamic Inversion Control with Deck Motion Prediction,” in *41st European Rotorcraft Forum*, Munich, Germany, 2015.

[78] N. A. Shneydor, *Missile Guidance and Pursuit: Kinematics, Dynamics and Control.* Elsevier, 1998.

[79] V. Utkin, “Variable Structure Systems With Sliding Modes,” *IEEE Transactions on Automatic control*, vol. 22, no. 2, pp. 212–222, 1977. doi: 10.1109/TAC.1977.1101446

[80] Y. Shtessel, C. Edwards, L. Fridman, and A. Levant, *Sliding Mode Control and Observation.* Birkhäuser Publishing, New York, NY, USA, 2014.

[81] J. Y. Hung, W. Gao, and J. C. Hung, “Variable Structure Control: A Survey,” *IEEE Transactions on Industrial Electronics*, vol. 40, no. 1, pp. 2–22, 1993. doi: 10.1109/41.184817

[82] J. R. Cloutier and D. T. Stansbery, “The Capabilities and Art of State-Dependent Riccati Equation-Based Design,” in *Proceedings of the American Control Conference.* Anchorage, AK, USA: IEEE, May 2002, pp. 86–91. doi: 10.1109/ACC.2002.1024785

[83] J. R. Cloutier, “State-Dependent Riccati Equation Techniques: An Overview,” in *Proceedings of the American Control Conference.* Albuquerque, New Mexico, USA: IEEE, June 1997, pp. 932–936. doi: 10.1109/ACC.1997.609663

[84] T. Çimen, “Survey of State-Dependent Riccati Equation in Nonlinear Optimal Feedback Control Synthesis,” *Journal of Guidance, Control, and Dynamics*, vol. 35, no. 4, pp. 1025–1047, 2012. doi: 10.2514/1.55821

[85] A. Bogdanov and E. A. Wan, "State-dependent Riccati Equation Control for Small Autonomous Helicopters," *Journal of Guidance, Control, and Dynamics*, vol. 30, no. 1, pp. 47–60, 2007. doi: 10.2514/1.21910

[86] D. T. Stansbery and J. R. Cloutier, "Position and Attitude Control of a Spacecraft Using the State-dependent Riccati Equation Technique," in *Proceedings of the American Control Conference*, Chicago, IL, USA, June 2000. doi: 10.1109/ACC.2000.879525

[87] A. Ratnoo and D. Ghose, "State-Dependent Riccati-Equation-Based Guidance Law for Impact-Angle-Constrained Trajectories," *Journal of Guidance, Control, and Dynamics*, vol. 32, no. 1, pp. 320–326, 2009. doi: 10.2514/1.37876

[88] R. A. Freeman and P. V. Kokotovic, "Optimal Nonlinear Controllers for Feedback Linearizable Systems," in *Proceedings of the American Control Conference.* Seattle, WA, USA: IEEE, June 1995, pp. 2722–2726. doi: 10.1109/ACC.1995.532343

[89] A. E. Bryson and Y. C. Ho, *Applied Optimal Control: Optimization, Estimation and Control.* Washington, DC, USA: Hemisphere Publishing Corporation, 1975.

[90] J. R. Cloutier, C. N. D'Souza, and C. P. Mracek, "Nonlinear Regulation and Nonlinear H_∞ Control via the State-dependent Riccati Equation Technique– Part 2, Examples," in *Proceedings of the First International Conference on Nonlinear Problems in Aviation and Aerospace.* Daytona Beach, FL, USA: Embry-Riddle Aeronautical Univ. Press Daytona Beach, FL, May 1996, pp. 117–130.

[91] E. N. Johnson and A. J. Calise, "Pseudo-control Hedging: A New Method for Adaptive Control," in *Advances in Navigation, Guidance, and Control Technology Workshop*, Redstone Arsenal, Alabama, USA, 2000.

[92] E. Johnson and S. Kannan, “Adaptive Flight Control for an Autonomous Unmanned Helicopter,” in *AIAA Guidance, Navigation, and Control Conference and Exhibit*, Monterey, California, 2002. doi: 10.2514/6.2002-4439

[93] D. Braun, K. Kampa, and D. Schimke, “Mission Oriented Investigation of Handling Qualities Through Simulation,” in *17th European Rotorcraft Forum*, Berlin, Germany, 1991.

[94] M. Dietz, C. Maucher, and D. Schimke, “Addressing Today’s Aeromechanic Questions by Industrial Answers,” in *American Helicopter Society Specialists’ Conference on Aeromechanics*, San Francisco, California, 2010.

[95] W. Johnson, “A History of Rotorcraft Comprehensive Analyses,” in *American Helicopter Society 69th Annual Forum*, Phoenix, Arizona, USA, 2013.

[96] C. J. Ockier, “Flight Evaluation of the New Handling Qualities Criteria Using the BO 105,” *Journal of the American Helicopter Society*, vol. 41, no. 1, pp. 67–76, 1996. doi: 10.4050/JAHS.41.67

[97] C. J. Ockier and V. Gollnick, “ADS-33 Flight Testing - Lessons Learned,” in *AGARD Conference Proceedings 592 - Advances in Rotorcraft Technology*, Ottawa, Canada, May 1996.

[98] J. A. Lusardi, M. B. Tischler, C. L. Blanken, and S. J. Labows, “Empirically Derived Helicopter Response Model and Control System Requirements for Flight in Turbulence,” *Journal of the American Helicopter Society*, vol. 49, no. 3, pp. 340–349, 2004. doi: 10.4050/JAHS.49.340

[99] S. Seher-Weiss and W. Von Gruenhagen, “Development of EC 135 Turbulence Models via System Identification,” *Aerospace Science and Technology*, vol. 23, no. 1, pp. 43–52, 2012. doi: 10.1016/j.ast.2011.09.008

[100] F. Viertler and M. Hajek, "Requirements and Design Challenges in Rotorcraft Flight Simulations for Research Applications," in *AIAA Modeling and Simulation Technologies Conference*, Kissimmee, Florida, USA, 2015. doi: 10.2514/6.2015-1808

[101] R. T. N. Chen and J. A. Jeske, "Kinematic Properties of the Helicopter in Coordinated Turns," *NASA Technical Paper 1773*, 1981.

[102] J. W. Harding, S. J. Moody, G. J. Jeram, H. Mansur, and M. B. Tischler, "Development of Modern Control Laws for the AH-64D in Hover/Low Speed Flight," in *American Helicopter Society 62nd Annual Forum*, Phoenix, AZ, USA, 2006.

[103] S. Vaddi, P. K. Menon, and E. J. Ohlmeyer, "Numerical State-dependent Riccati Equation Approach for Missile Integrated Guidance Control," *Journal of Guidance, Control, and Dynamics*, vol. 32, no. 2, pp. 699–703, 2009. doi: 10.2514/1.34291

[104] A. M. Shkel and V. Lumelsky, "Classification of the Dubins Set," *Robotics and Autonomous Systems*, vol. 34, no. 4, pp. 179–202, 2001. doi: 10.1016/S0921-8890(00)00127-5

[105] F. Plestan, Y. Shtessel, V. Bregeault, and A. Poznyak, "New Methodologies for Adaptive Sliding Mode Control," *International journal of control*, vol. 83, no. 9, pp. 1907–1919, 2010.

[106] A. Levant, "Sliding Order and Sliding Accuracy in Sliding Mode Control," *International Journal of Control*, vol. 58, no. 6, pp. 1247–1263, 1993.

This page intentionally left blank.

A Appendix A

A.1 Structure of System and Control Matrices

The matrices referred to in Chapter 5 are expanded below. Here, $\mathrm{s}_{(\cdot)}$, $\mathrm{c}_{(\cdot)}$, $\mathrm{t}_{(\cdot)}$ represent sine, cosine, and tangent respectively; $Z_{(\cdot)}$, $L_{(\cdot)}$, $M_{(\cdot)}$, $N_{(\cdot)}$ represent partial derivatives of normal force, roll, pitch, and yaw moments respectively.

The full linear system model used in the synthesis of the EMF control laws is represented by:

$$\mathbf{A} = \left[\begin{array}{cc|cccc} 0 & 0 & 0 & 1 & \mathrm{s}_\phi \mathrm{t}_\theta & \mathrm{c}_\phi \mathrm{t}_\theta \\ 0 & 0 & 0 & 0 & \mathrm{c}_\phi & -\mathrm{s}_\phi \\ \hline 0 & 0 & Z_w & Z_p & Z_q & Z_r \\ 0 & 0 & L_w & L_p & L_q & L_r \\ 0 & 0 & M_w & M_p & M_q & M_r \\ 0 & 0 & N_w & N_p & N_q & N_r \end{array}\right], \qquad \mathbf{B} = \left[\begin{array}{cccc} 0 & 0 & 0 & 0 \\ 0 & 0 & 0 & 0 \\ \hline Z_\theta & Z_\alpha & Z_\beta & Z_\delta \\ L_\theta & L_\alpha & L_\beta & L_\delta \\ M_\theta & M_\alpha & M_\beta & M_\delta \\ N_\theta & N_\alpha & N_\beta & N_\delta \end{array}\right]$$

The sparse linear model used in the synthesis of the SMC attitude control laws is represented by:

$$\mathbf{A} = \left[\begin{array}{cc|cccc} 0 & 0 & 0 & 1 & \mathrm{s}_\phi \mathrm{t}_\theta & \mathrm{c}_\phi \mathrm{t}_\theta \\ 0 & 0 & 0 & 0 & \mathrm{c}_\phi & -\mathrm{s}_\phi \\ \hline 0 & 0 & Z_w & 0 & 0 & 0 \\ 0 & 0 & 0 & L_p & 0 & 0 \\ 0 & 0 & 0 & 0 & M_q & 0 \\ 0 & 0 & 0 & 0 & 0 & N_r \end{array}\right], \quad \mathbf{B} = \left[\begin{array}{cccc} 0 & 0 & 0 & 0 \\ 0 & 0 & 0 & 0 \\ \hline Z_\theta & 0 & 0 & 0 \\ 0 & L_\alpha & 0 & 0 \\ 0 & 0 & M_\beta & 0 \\ 0 & 0 & 0 & N_\delta \end{array}\right]$$

The output matrix for both controllers is represented by:

$$\mathbf{C} = \left[\begin{array}{cc|cccc} 1 & 0 & 0 & 0 & 0 & 0 \\ 0 & 1 & 0 & 0 & 0 & 0 \\ 0 & 0 & 1 & 0 & 0 & 0 \\ 0 & 0 & 0 & 0 & 0 & 1 \end{array}\right]$$

The augmented system matrices for the SMC controller are represented by:

$$\tilde{\mathbf{A}} = \left[\begin{array}{cc|c} \mathbf{0}_{4\times4} & \mathbf{C}_1 & \mathbf{C}_2 \\ \mathbf{0}_{2\times4} & \mathbf{A}_{11} & \mathbf{A}_{12} \\ \hline \mathbf{0}_{4\times4} & \mathbf{A}_{21} & \mathbf{A}_{22} \end{array}\right], \quad \tilde{\mathbf{B}} = \begin{bmatrix} \mathbf{0}_{6\times4} \\ \mathbf{B}_2 \end{bmatrix}, \quad \tilde{\mathbf{T}} = \begin{bmatrix} \mathbf{I}_{4\times4} \\ \mathbf{0}_{6\times4} \end{bmatrix}, \quad \tilde{\mathbf{f}} = \begin{bmatrix} \mathbf{0}_{6\times1} \\ \mathbf{B}_2\boldsymbol{\Gamma} \end{bmatrix}$$

The SMC gain matrices are represented by:

$$\mathbf{S}_1 = \begin{bmatrix} 0 & 0 & \lambda_w & 0 & 0 & 0 \\ 0 & 0 & 0 & \lambda_r & 0 & 0 \\ \omega_\phi^2 & 0 & 0 & 0 & 2\zeta_\phi\omega_\phi & 0 \\ 0 & \omega_\theta^2 & 0 & 0 & 0 & 2\zeta_\theta\omega_\theta \end{bmatrix}, \quad \mathbf{S}_2 = \begin{bmatrix} 1 & 0 & 0 & 0 \\ 0 & 0 & 0 & 1 \\ 0 & 1 & \mathrm{s}_\phi \mathrm{t}_\theta & \mathrm{c}_\phi \mathrm{t}_\theta \\ 0 & 0 & \mathrm{c}_\phi & -\mathrm{s}_\phi \end{bmatrix}$$

A.2 BO105 Linear Model

The system and control matrices of the linearized system in Eqn. 4.9 and in Appendix A.1 are expanded below.

Hover

$$\mathbf{A}^* = \begin{bmatrix} 0 & 0 & 0 & 0 & 0 & 1.0000 & -0.0058 & 0.0784 \\ 0 & 0 & 0 & 0 & 0 & 0 & 0.9973 & 0.0734 \\ 0 & -0.1706 & -0.0269 & -0.0112 & 0.0130 & -0.0013 & 0.0159 & -0.0004 \\ 0.1702 & 0.0010 & 0.0190 & -0.0672 & -0.0083 & -0.0154 & 0.0008 & -0.0002 \\ 0.0125 & -0.0134 & 0.0233 & -0.0002 & -0.2754 & -0.0005 & -0.0014 & 0.0085 \\ 0 & 0 & 9.6100 & -14.2400 & 0.1285 & -9.5330 & 2.1290 & -0.7146 \\ 0 & 0 & 3.2970 & 2.9340 & -2.8510 & -0.1193 & -3.2580 & -0.0396 \\ 0 & 0 & 1.6880 & -1.5440 & 0.0209 & -1.6420 & 0.4045 & -0.3294 \end{bmatrix}$$

$$\mathbf{B}^* = \begin{bmatrix} 0 & 0 & 0 & 0 \\ 0 & 0 & 0 & 0 \\ 0.0857 & -0.1681 & 0.0075 & -0.0000 \\ 0.0009 & -0.0159 & 0.1956 & 0.0359 \\ -1.0130 & -0.0113 & 0.0036 & 0.0001 \\ 2.0940 & -14.4451 & 75.1196 & -0.4211 \\ -3.1080 & 22.7306 & 2.4491 & -0.1022 \\ 13.2500 & -2.9615 & 12.0676 & -5.2350 \end{bmatrix}$$

Low-speed, 20 m/s

$$\mathbf{A}^{*} = \begin{bmatrix} 0 & 0 & 0 & 0 & 0 & 1.0000 & -0.0021 & 0.0796 \\ 0 & 0 & 0 & 0 & 0 & 0 & 0.9996 & 0.0267 \\ 0 & -0.1706 & -0.0241 & -0.0056 & 0.0245 & 0.0008 & -0.0083 & -0.0010 \\ 0.1706 & 0.0004 & 0.0069 & -0.0794 & 0.0016 & 0.0120 & 0.0025 & -0.3470 \\ 0.0046 & -0.0136 & -0.0866 & -0.0124 & -0.4540 & 0.0134 & 0.3494 & 0.0085 \\ 0 & 0 & -2.9120 & -11.2100 & 7.9430 & -8.6120 & 2.8520 & -0.7062 \\ 0 & 0 & 3.0930 & 1.4180 & -0.5912 & -0.7654 & -3.5970 & -0.0704 \\ 0 & 0 & -3.1960 & -0.4223 & -0.1211 & -1.6410 & 0.8938 & -0.5083 \end{bmatrix}$$

$$\mathbf{B}^{*} = \begin{bmatrix} 0 & 0 & 0 & 0 \\ 0 & 0 & 0 & 0 \\ 0.0596 & -0.1513 & -0.0169 & -0.0056 \\ -0.0145 & -0.0200 & 0.1780 & 0.0212 \\ -1.0150 & -0.1220 & 0.0126 & -0.0005 \\ 4.4070 & -13.1207 & 69.9613 & -0.2477 \\ 2.0950 & 21.0346 & 4.6937 & -0.0113 \\ 9.8130 & -3.9019 & 10.9844 & -3.0860 \end{bmatrix}$$

Forward flight, $40\,\mathrm{m/s}$

$$\mathbf{A}^* = \begin{bmatrix} 0 & 0 & 0 & 0 & 0 & 1.0000 & -0.0007 & 0.0316 \\ 0 & 0 & 0 & 0 & 0 & 0 & 0.9998 & 0.0208 \\ 0 & -0.1711 & -0.0384 & -0.0030 & 0.0131 & -0.0001 & -0.0038 & -0.0004 \\ 0.1710 & 0.0001 & 0.0059 & -0.1162 & -0.0131 & 0.0081 & 0.0012 & -0.6950 \\ 0.0036 & -0.0054 & 0.0131 & -0.0085 & -0.5711 & 0.0140 & 0.6966 & 0.0088 \\ 0 & 0 & -2.9020 & -10.4400 & 3.6570 & -7.5750 & 2.3210 & -0.4796 \\ 0 & 0 & 2.4250 & 0.5813 & 0.0982 & -0.5913 & -3.3910 & -0.0880 \\ 0 & 0 & -2.5800 & 0.0393 & -1.1710 & -1.3890 & 1.0190 & -0.6843 \end{bmatrix}$$

$$\mathbf{B}^* = \begin{bmatrix} 0 & 0 & 0 & 0 \\ 0 & 0 & 0 & 0 \\ 0.0135 & -0.1823 & -0.0204 & -0.0169 \\ -0.0178 & -0.0400 & 0.1562 & 0.0395 \\ -1.1930 & -0.3137 & 0.0195 & -0.0006 \\ 3.3560 & -11.7840 & 67.6947 & -0.4641 \\ 8.1560 & 23.7585 & 4.9963 & 0.1814 \\ 6.3260 & -3.0240 & 11.7131 & -5.7560 \end{bmatrix}$$

This page intentionally left blank.

B Appendix B: Full Derivation and Analysis of Cascaded Two-Loop Dynamics

B.1 Attitude and Rate Command Control

Consider the full-order 6DOF rigid-body linearized multivariable uncertain system:

$$\dot{\mathbf{x}}(t) = \mathbf{A}\mathbf{x}(t) + \mathbf{B}\mathbf{u}(t) + \mathbf{f}(\mathbf{x}, \mathbf{u}, t) \tag{B.1}$$

$$\mathbf{y}(t) = \mathbf{C}\mathbf{x}(t) \tag{B.2}$$

where $\mathbf{A} \in \mathbb{R}^{n \times n}$, $\mathbf{B} \in \mathbb{R}^{m \times n}$, $\mathbf{C} \in \mathbb{R}^{p \times n}$, $n \geq m$. The system of Eqns. (B.1)–(B.2) is identical to Eqn. (5.10), except that the longitudinal and lateral speed states are not dropped.

For the helicopter dynamics, $\mathbf{x} \equiv [\phi \; \theta \; u \; v \; w \; p \; q \; r]^\top$, $\mathbf{u} \equiv [D_\theta \; D_\beta \; D_\alpha \; D_\delta]^\top$, $\mathbf{y} \equiv [\phi \; \theta \; w \; r]^\top$ giving $n = 8$, $m = 4$, and $p = 4$. The states and controls are as defined in the nomenclature section. $\mathbf{y}$ is a subset of the state vector that must robustly track a command signal $\mathbf{r} \equiv [\phi_c \; \theta_c \; w_c \; r_c]^\top$. Note that for the purpose of controller synthesis, full state feedback is assumed. The unknown function $\mathbf{f} : \mathbb{R}^8 \times \mathbb{R}^4 \times \mathbb{R}^+ \to \mathbb{R}^8$ collects unknown but matched and bounded uncertainties, which implies that it can be expressed as $\mathbf{f}(\mathbf{x}, \mathbf{u}, t) = \mathbf{B}\Gamma$, where $\|\Gamma\| \leq L$.

The system and control matrices in Eqn. (B.1) containing the partial derivatives and the output matrix in Eqn. (B.2) take the form:

$$\mathbf{A} = \left[\begin{array}{cc|cccccc} 0 & 0 & 0 & 0 & 0 & 1 & 0 & 0 \\ 0 & 0 & 0 & 0 & 0 & 0 & 1 & 0 \\ \hline 0 & -g & X_u & X_v & X_w & X_p & X_q & X_r \\ g & 0 & Y_u & Y_v & Y_w & Y_p & Y_q & Y_r \\ 0 & 0 & Z_u & Z_v & Z_w & Z_p & Z_q & Z_r \\ 0 & 0 & L_u & L_v & L_w & L_p & L_q & L_r \\ 0 & 0 & M_u & M_v & M_w & M_p & M_q & M_r \\ 0 & 0 & N_u & N_v & N_w & N_p & N_q & N_r \end{array}\right], \quad \mathbf{B} = \left[\begin{array}{cccc} 0 & 0 & 0 & 0 \\ 0 & 0 & 0 & 0 \\ \hline X_\theta & X_\alpha & X_\beta & X_\delta \\ Y_\theta & Y_\alpha & Y_\beta & Y_\delta \\ Z_\theta & Z_\alpha & Z_\beta & Z_\delta \\ L_\theta & L_\alpha & L_\beta & L_\delta \\ M_\theta & M_\alpha & M_\beta & M_\delta \\ N_\theta & N_\alpha & N_\beta & N_\delta \end{array}\right], \tag{B.3}$$

$$\mathbf{C} = \begin{bmatrix} 1 & 0 & 0 & 0 & 0 & 0 & 0 & 0 \\ 0 & 1 & 0 & 0 & 0 & 0 & 0 & 0 \\ 0 & 0 & 0 & 0 & 1 & 0 & 0 & 0 \\ 0 & 0 & 0 & 0 & 0 & 0 & 0 & 1 \end{bmatrix}. \tag{B.4}$$

To allow asymptotic tracking of the command vector by the output vector, the tracking error is defined as $\mathbf{x}_e(t) = \int_0^t (\mathbf{y}(t) - \mathbf{r}(t))dt$. An augmented state vector is defined as $\bar{\mathbf{x}} \equiv [\mathbf{x}_e \ \mathbf{x}]^\top$ and the augmented system and control matrices are defined as:

$$\bar{\mathbf{A}} = \begin{bmatrix} \mathbf{0} & \mathbf{C} \\ \mathbf{0} & \mathbf{A} \end{bmatrix}, \quad \bar{\mathbf{B}} = \begin{bmatrix} \mathbf{0} \\ \mathbf{B} \end{bmatrix}. \tag{B.5}$$

where $\bar{\mathbf{A}} \in \mathbb{R}^{12\times 12}$ and $\bar{\mathbf{B}} \in \mathbb{R}^{12\times 4}$.

There exists an orthogonal transformation matrix $\mathbf{T}_r$ satisfying

$$\mathbf{T}_r\bar{\mathbf{B}} = \begin{bmatrix} \mathbf{0} \\ \mathbf{B}_2 \end{bmatrix}, \tag{B.6}$$

where $\mathbf{B}_2 \in \mathbb{R}^{4\times 4}$. The matrix $\mathbf{T}_r$ can be computed via QR decomposition.

The transformed state vector is:

$$\tilde{\mathbf{x}} = \mathbf{T}_r\bar{\mathbf{x}} \tag{B.7}$$

This allows the original system $\bar{\mathbf{x}} \equiv [\mathbf{x}_e\ \mathbf{x}]^\top$ to be represented as $\tilde{\mathbf{x}} \equiv [\mathbf{x}_1\ \mathbf{x}_2]^\top$, where $\mathbf{x}_1 \in \mathbb{R}^8$ represents the indirectly actuated states states, and $\mathbf{x}_2 \in \mathbb{R}^4$ represents the states on which the control vector acts (directly actuated states). $\mathbf{T}_r$ also permits the inverse transformation from $\tilde{\mathbf{x}}$ into the original coordinates $\bar{\mathbf{x}}$ without loss of numerical accuracy. For further details, see Ref. [38, Sec. A.2.5].

The system dynamics from Eqn. (B.1) in the transformed coordinates can be written as:

$$\begin{bmatrix} \dot{\mathbf{x}}_1 \\ \dot{\mathbf{x}}_2 \end{bmatrix} = \begin{bmatrix} \tilde{\mathbf{A}}_{11} & \tilde{\mathbf{A}}_{12} \\ \tilde{\mathbf{A}}_{21} & \tilde{\mathbf{A}}_{22} \end{bmatrix} \begin{bmatrix} \mathbf{x}_1 \\ \mathbf{x}_2 \end{bmatrix} + \begin{bmatrix} \mathbf{0} \\ \mathbf{B}_2 \end{bmatrix} - \begin{bmatrix} \mathbf{T}_1 \\ \mathbf{0} \end{bmatrix} \mathbf{r} + \begin{bmatrix} \mathbf{0} \\ \mathbf{f} \end{bmatrix} \tag{B.8}$$

where $\tilde{\mathbf{A}}_{11} \in \mathbb{R}^{8\times 8}$, $\tilde{\mathbf{A}}_{12} \in \mathbb{R}^{8\times 4}$, $\tilde{\mathbf{A}}_{21} \in \mathbb{R}^{4\times 8}$, $\tilde{\mathbf{A}}_{22} \in \mathbb{R}^{4\times 4}$, $\mathbf{B}_2 \in \mathbb{R}^{4\times 4}$, and $\mathbf{T}_1 \in \mathbb{R}^{8\times 4}$, and $\mathbf{B}_2$ is in row echelon form.

The system in Eqn.(B.8) can be written in compact form as:

$$\dot{\tilde{\mathbf{x}}} = \tilde{\mathbf{A}}\tilde{\mathbf{x}} + \tilde{\mathbf{B}}\mathbf{u} - \tilde{\mathbf{T}}\mathbf{r} + \tilde{\mathbf{f}} \tag{B.9}$$

and the time dependence is dropped for brevity.

The sliding variable from Eqn. (5.15) is ordered differently and written as:

$$\boldsymbol{\sigma} = \begin{bmatrix} \dot{\phi} + 2\zeta_\phi\omega_\phi\phi + \omega_\phi^2 \int_0^t (\phi - \phi_c) d\tau \\ \dot{\theta} + 2\zeta_\theta\omega_\theta\theta + \omega_\theta^2 \int_0^t (\theta - \theta_c) d\tau \\ w + \lambda_w \int_0^t (w - w_c) d\tau \\ r + \lambda_r \int_0^t (r - r_c) d\tau \end{bmatrix} \tag{B.10}$$

Assuming $\dot{\phi} \approx p$ and $\dot{\theta} \approx q$, $\boldsymbol{\sigma}$ can be written in the original coordinates as:

$$\boldsymbol{\sigma} = \mathbf{S}\bar{\mathbf{x}}, \tag{B.11}$$

where

$$\mathbf{S} = \begin{bmatrix} \omega_\phi^2 & 0 & 0 & 0 & 2\zeta_\phi\omega_\phi & 0 & 0 & 0 & 0 & 1 & 0 & 0 \\ 0 & \omega_\theta^2 & 0 & 0 & 0 & 2\zeta_\theta\omega_\theta & 0 & 0 & 0 & 0 & 1 & 0 \\ 0 & 0 & \lambda_w & 0 & 0 & 0 & 0 & 0 & 1 & 0 & 0 & 0 \\ 0 & 0 & 0 & \lambda_r & 0 & 0 & 0 & 0 & 0 & 0 & 0 & 1 \end{bmatrix} \tag{B.12}$$

In the transformed coordinates, $\mathbf{S}$ can be written as:

$$\tilde{\mathbf{S}} = [\mathbf{S}_1 \ \mathbf{S}_2]^\top = \mathbf{S}\mathbf{T}_r^\top \tag{B.13}$$

where $\mathbf{S}_1 \in \mathbb{R}^{4\times 8}$ and $\mathbf{S}_2 \in \mathbb{R}^{4\times 4}$. Also note that

$$\det(\tilde{\mathbf{S}}\tilde{\mathbf{B}}) = \det(\mathbf{S}_2\mathbf{B}_2) = \det(\mathbf{S}_2)\det(\mathbf{B}_2) \tag{B.14}$$

$\tilde{\mathbf{S}}\tilde{\mathbf{B}}$ is nonsingular if $\tilde{\mathbf{S}}_2$ is invertible, since $\det(\mathbf{B}_2) \neq 0$.

From Eqn. (B.11), the sliding variable in the transformed coordinates is:

$$\boldsymbol{\sigma} = \mathbf{S}_1\mathbf{x}_1 + \mathbf{S}_2\mathbf{x}_2 = \tilde{\mathbf{S}}\tilde{\mathbf{x}}. \tag{B.15}$$

The first derivative of Eqn. (B.15) gives:

$$\dot{\boldsymbol{\sigma}} = \mathbf{S}_1\dot{\mathbf{x}}_1 + \mathbf{S}_2\dot{\mathbf{x}}_2 = \tilde{\mathbf{S}}\dot{\tilde{\mathbf{x}}}. \tag{B.16}$$

Substituting $\dot{\tilde{\mathbf{x}}}$ from Eqn. (B.9) gives:

$$\dot{\boldsymbol{\sigma}} = \tilde{\mathbf{S}}\tilde{\mathbf{A}}\tilde{\mathbf{x}} + \tilde{\mathbf{S}}\tilde{\mathbf{B}}\mathbf{u} - \tilde{\mathbf{S}}\tilde{\mathbf{T}}\mathbf{r} + \tilde{\mathbf{S}}\tilde{\mathbf{f}}. \tag{B.17}$$

To enforce $\dot{\boldsymbol{\sigma}} < 0$, consider the ideal sliding mode control law (analogous to Eqn. (5.18) but without continuous approximation for the discontinuous control term):

$$\mathbf{u} = -(\tilde{\mathbf{S}}\tilde{\mathbf{B}})^{-1}\left((\tilde{\mathbf{S}}\tilde{\mathbf{A}} - \boldsymbol{\Phi}_1\tilde{\mathbf{S}})\tilde{\mathbf{x}} + \tilde{\mathbf{S}}\tilde{\mathbf{T}}\mathbf{r} - \boldsymbol{\rho}\,\frac{\mathbf{P}_1\tilde{\mathbf{S}}\tilde{\mathbf{x}}}{\|\mathbf{P}_1\tilde{\mathbf{S}}\tilde{\mathbf{x}}\|}\right), \tag{B.18}$$

where $\mathbf{P}_1$ is a positive definite matrix satisfying the Lyapunov equation $\mathbf{P}_1\boldsymbol{\Phi}_1 + \boldsymbol{\Phi}_1^{\mathrm{T}}\mathbf{P}_1 = -\mathbf{I}$.

Insert the control law in Eqn. (B.18) into Eqn. (B.17) followed by algebraic manipulations to obtain:

$$\dot{\boldsymbol{\sigma}} = \boldsymbol{\Phi}_1\boldsymbol{\sigma} - \boldsymbol{\rho}\,\frac{\mathbf{P}_1\tilde{\mathbf{S}}\tilde{\mathbf{x}}}{\|\mathbf{P}_1\tilde{\mathbf{S}}\tilde{\mathbf{x}}\|} + \tilde{\mathbf{S}}\tilde{\mathbf{f}} = \boldsymbol{\Phi}_1\boldsymbol{\sigma} - \boldsymbol{\rho}\,\frac{\mathbf{P}_1\boldsymbol{\sigma}}{\|\mathbf{P}_1\boldsymbol{\sigma}\|} + \tilde{\mathbf{S}}\tilde{\mathbf{f}}. \tag{B.19}$$

The presence of $\boldsymbol{\Phi}_1$ in Eqn. (B.19) gives global asymptotic stability about $\boldsymbol{\sigma} = \mathbf{0}$ for the nominal system without the disturbance term $(\tilde{\mathbf{S}}\tilde{\mathbf{f}})$ and with the linear component of the control law only, i.e. $\dot{\boldsymbol{\sigma}} = \boldsymbol{\Phi}_1\boldsymbol{\sigma}$, where $\boldsymbol{\Phi}_1$ is stable, i.e. $\mathrm{Re(eig)}(\boldsymbol{\Phi}_1) < 0$. Note that $\mathbf{P}_1$ exists if and only if $\boldsymbol{\Phi}_1$ is stable [80, Theorem D.3].

To show global finite-time stability about $\boldsymbol{\sigma} = \mathbf{0}$, consider the Lyapunov function candidate $V = \boldsymbol{\sigma}^{\mathrm{T}}\mathbf{P}_1\boldsymbol{\sigma} > 0$, which satisfies $V(0) = 0, V_{(\boldsymbol{\sigma}\to\infty)} \to \infty$. Its time derivative is given by:

$$\dot{V} = \dot{\boldsymbol{\sigma}}^{\top}\mathbf{P}_1\boldsymbol{\sigma} + \boldsymbol{\sigma}^{\top}\mathbf{P}_1\dot{\boldsymbol{\sigma}} \tag{B.20}$$

Substitute for $\dot{\boldsymbol{\sigma}}$ from Eqn. (B.19) to obtain:

$$\dot{V} = \left(\boldsymbol{\Phi}_1\boldsymbol{\sigma} - \boldsymbol{\rho}\,\frac{\mathbf{P}_1\boldsymbol{\sigma}}{\|\mathbf{P}_1\boldsymbol{\sigma}\|} + \tilde{\mathbf{S}}\tilde{\mathbf{f}}\right)^{\top}\mathbf{P}_1\boldsymbol{\sigma} + \boldsymbol{\sigma}^{\top}\mathbf{P}_1\left(\boldsymbol{\Phi}_1\boldsymbol{\sigma} - \boldsymbol{\rho}\,\frac{\mathbf{P}_1\boldsymbol{\sigma}}{\|\mathbf{P}_1\boldsymbol{\sigma}\|} + \tilde{\mathbf{S}}\tilde{\mathbf{f}}\right) \tag{B.21}$$

which upon simplification gives:

$$\dot{V} = \boldsymbol{\sigma}^{\top}(\mathbf{P}_1\boldsymbol{\Phi}_1 + \boldsymbol{\Phi}_1^{\top}\mathbf{P}_1)\boldsymbol{\sigma} - 2\boldsymbol{\rho}\frac{\boldsymbol{\sigma}^{\top}\mathbf{P}_1^2\boldsymbol{\sigma}}{\|\mathbf{P}_1\boldsymbol{\sigma}\|} + 2\boldsymbol{\sigma}^{\top}\mathbf{P}_1\tilde{\mathbf{S}}\tilde{\mathbf{f}} \tag{B.22}$$

$$\dot{V} = -\boldsymbol{\sigma}^{\top}\boldsymbol{\sigma} - 2\boldsymbol{\rho}\|\mathbf{P}_1\boldsymbol{\sigma}\| + 2\boldsymbol{\sigma}^{\top}\mathbf{P}_1\tilde{\mathbf{S}}\tilde{\mathbf{f}} \tag{B.23}$$

Equation (B.23) can be written as an inequality:

$$\dot{V} \leq -\|\boldsymbol{\sigma}\|^2 - 2\boldsymbol{\rho}\|\mathbf{P}_1\boldsymbol{\sigma}\| + 2\|\mathbf{P}_1\boldsymbol{\sigma}\|\,\|\tilde{\mathbf{S}}\tilde{\mathbf{f}}\| \tag{B.24}$$

$$\dot{V} \leq -2\|\mathbf{P}_1\boldsymbol{\sigma}\|(\boldsymbol{\rho} - \|\tilde{\mathbf{S}}\tilde{\mathbf{f}}\|) \tag{B.25}$$

If the sliding mode gain vector is set as $\boldsymbol{\rho} > \|\tilde{\mathbf{S}}\tilde{\mathbf{f}}\| + \gamma$ for some $\gamma > 0$ then $\dot{V} < 0$ is ensured except if $\boldsymbol{\sigma} = \mathbf{0}$. For this choice of the sliding mode gain, global asymptotic stability about $\boldsymbol{\sigma} = \mathbf{0}$ is ensured.

Using $\boldsymbol{\rho} > \|\tilde{\mathbf{S}}\tilde{\mathbf{f}}\| + \gamma$, Eqn. (B.25) becomes:

$$\dot{V} < -2\gamma\|\mathbf{P}_1\boldsymbol{\sigma}\| \tag{B.26}$$

Using [38, p.53], the reaching time for $\boldsymbol{\sigma} = \mathbf{0}$ can be shown by first writing $\|\mathbf{P}_1\boldsymbol{\sigma}\|^2 = (\sqrt{\mathbf{P}_1}\boldsymbol{\sigma})^{\top}\mathbf{P}_1(\sqrt{\mathbf{P}_1}\boldsymbol{\sigma}) \geqslant \lambda_{\min}(\mathbf{P}_1)\|\mathbf{P}_1\boldsymbol{\sigma}\|^2 = \Lambda_{\min}(\mathbf{P}_1)V$ and then writing Eqn. (B.26) as:

$$\dot{V} < -2\gamma\sqrt{\Lambda_{\min}(\mathbf{P}_1)V} \tag{B.27}$$

where $\Lambda_{\min}(\mathbf{P}_1)$ represents the minimum eigenvalue of $\mathbf{P}_1$. Integrating Eqn. (B.27) in the time interval $t = 0$ at initial value V_0 to $t = t_r$ with $V = 0$, the estimate of t_r is obtained as:

$$t_r < \frac{1}{\gamma}\sqrt{\frac{V_0}{\Lambda_{\min}(\mathbf{P}_1)}}. \tag{B.28}$$

Thus, sliding mode $\boldsymbol{\sigma} = \mathbf{0}$ occurs at $t = t_r$ which implies that $\boldsymbol{\sigma} = \mathbf{S}_1\mathbf{x}_1 + \mathbf{S}_2\mathbf{x}_2 = 0$ and thus $\mathbf{x}_1$ and $\mathbf{x}_2$ can be expressed algebraically as:

$$\mathbf{x}_2 = -\mathbf{S}_2^{-1}\mathbf{S}_1\mathbf{x}_1, \tag{B.29}$$

since $\mathbf{S}_2$ is square and invertible. From Eqn. (B.8), the system dynamics when sliding mode occurs can be expressed as:

$$\begin{aligned} \dot{\mathbf{x}}_1 &= (\tilde{\mathbf{A}}_{11} - \tilde{\mathbf{A}}_{12}\mathbf{S}_2^{-1}\mathbf{S}_1)\mathbf{x}_1 - \mathbf{T}_1\mathbf{r} && \text{(B.30)} \\ \dot{\mathbf{x}}_2 &= -\mathbf{S}_2^{-1}\mathbf{S}_1(\tilde{\mathbf{A}}_{11} - \tilde{\mathbf{A}}_{12}\mathbf{S}_2^{-1}\mathbf{S}_1)\mathbf{x}_1 + \mathbf{S}_2^{-1}\mathbf{S}_1\mathbf{T}_1\mathbf{r} && \text{(B.31)} \end{aligned}$$

The closed-loop system upon $\boldsymbol{\sigma} = \mathbf{0}$ is totally insensitive to the disturbance $\mathbf{f}$ and $\tilde{\mathbf{A}}_{\text{cl}} = (\tilde{\mathbf{A}}_{11} - \tilde{\mathbf{A}}_{12}\mathbf{S}_2^{-1}\mathbf{S}_1)$ has stable eigenvalues.

B.2 Translational Rate Command Control

Identical to Sec. 5.4, the uncertain inertial translational dynamics are written as:

$$\dot{\mathbf{z}}(t) = \mathbf{F}\mathbf{z}(t) + \mathbf{G}\mathbf{r}_1(t) + \mathbf{d}(\mathbf{z}, \mathbf{r}_1, t) \tag{B.32}$$

where

$$\mathbf{F} = \mathbf{0}_{2\times2}, \quad \mathbf{G} = \begin{bmatrix} g/(V\cos\theta) & 0 \\ g\tan\theta\tan\phi & -g \end{bmatrix} \approx \begin{bmatrix} g/V & 0 \\ 0 & -g \end{bmatrix} \tag{B.33}$$

and $\mathbf{z} \equiv [\chi \; V_h]^\top$, $\mathbf{r}_1 \equiv [\phi \; \theta]^\top$. The state vector $\mathbf{z}$ is required to asymptotically track the command signal $\mathbf{q} \equiv [\chi_c \; V_{h,c}]^\top$. Note that Sec. 5.4 considered an output signal $\mathbf{w}$ identical to the state vector $\mathbf{z}$. However, in the present analysis, $\mathbf{w}$ will be used to denote the output also for conciseness. The tracking error is defined as $\mathbf{z}_e = \int_0^t (\mathbf{z} - \mathbf{q})$ and an augmented state vector is defined as $\tilde{\mathbf{z}} \equiv [\mathbf{z}_e \; \mathbf{z}]^\mathrm{T}$. The augmented system dynamics are expressed as:

$$\begin{aligned} \dot{\tilde{\mathbf{z}}} &= \tilde{\mathbf{F}}\tilde{\mathbf{z}} + \tilde{\mathbf{G}}\mathbf{r}_1 - \tilde{\mathbf{T}}_o\mathbf{q} + \tilde{\mathbf{d}} \\ \text{where} \quad \tilde{\mathbf{F}} &= \begin{bmatrix} \mathbf{0} & \mathbf{I}_2 \\ \mathbf{0} & \mathbf{0} \end{bmatrix}, \; \tilde{\mathbf{G}} = \begin{bmatrix} \mathbf{0} \\ \mathbf{G} \end{bmatrix}, \; \tilde{\mathbf{T}}_o = \begin{bmatrix} \mathbf{I}_2 \\ \mathbf{0} \end{bmatrix}, \text{and } \; \tilde{\mathbf{d}} = \begin{bmatrix} \mathbf{0} \\ \mathbf{d} \end{bmatrix} \end{aligned} \tag{B.34}$$

The sliding variable is defined as:

$$\boldsymbol{\mu} = \begin{bmatrix} (\chi - \chi_c) + \lambda_\chi \int_0^t (\chi - \chi_c) d\tau \\ (V_h - V_{h,c}) + \lambda_h \int_0^t (V_h - V_{h,c}) d\tau \end{bmatrix} \tag{B.35}$$

and expressed in terms of the augmented state vector as:

$$\mathcal{R} = \{(\mathbf{z}_e, \mathbf{z}) : \boldsymbol{\mu} = \mathbf{R}_1\mathbf{z}_e + \mathbf{R}_2\mathbf{z} - \mathbf{R}_3\mathbf{q} = \mathbf{0}\} \tag{B.36}$$

$$\text{where} \quad \mathbf{R}_1 = \begin{bmatrix} \lambda_\chi & 0 \\ 0 & \lambda_h \end{bmatrix}, \; \mathbf{R}_2 = \mathbf{I}_2, \; \mathbf{R}_3 = \mathbf{I}_2. \tag{B.37}$$

The first derivative of Eqn. (B.35) gives:

$$\dot{\boldsymbol{\mu}} = \mathbf{R}_1\dot{\mathbf{z}}_e + \mathbf{R}_2\dot{\mathbf{z}} - \mathbf{R}_3\dot{\mathbf{q}} = \mathbf{R}\dot{\tilde{\mathbf{z}}} - \mathbf{R}_3\dot{\mathbf{q}}, \tag{B.38}$$

where $\mathbf{R} = [\mathbf{R}_1 \; \mathbf{R}_2]$. Substitute from Eqn. (B.34) to obtain:

$$\dot{\boldsymbol{\mu}} = \mathbf{R}\tilde{\mathbf{F}}\tilde{\mathbf{z}} + \mathbf{R}\tilde{\mathbf{G}}\mathbf{r}_1 - \mathbf{R}\tilde{\mathbf{T}}_o\mathbf{q} + \mathbf{R}\tilde{\mathbf{d}} - \mathbf{R}_3\dot{\mathbf{q}} \tag{B.39}$$

For negative definiteness of $\dot{\boldsymbol{\mu}}$, consider the ideal sliding mode control law:

$$\mathbf{r}_1 = -(\mathbf{R}\tilde{\mathbf{G}})^{-1}\left(\mathbf{R}\tilde{\mathbf{F}}\tilde{\mathbf{z}} - \boldsymbol{\Phi}_2\mathbf{R}\tilde{\mathbf{z}} + \boldsymbol{\Phi}_2\mathbf{R}_3\mathbf{q} - \mathbf{R}\tilde{\mathbf{T}}_o\mathbf{q} - \mathbf{R}_3\dot{\mathbf{q}} + \rho_o\frac{\mathbf{P}_2\boldsymbol{\mu}}{\|\mathbf{P}_2\boldsymbol{\mu}\|}\right) \tag{B.40}$$

where $\mathbf{P}_2$ is a positive definite matrix satisfying the Lyapunov equation $\mathbf{P}_2\boldsymbol{\Phi}_2 + \boldsymbol{\Phi}_2^{\top}\mathbf{P}_2 = -\mathbf{I}$. Substitute Eqn. (B.40) into Eqn. (B.39) to obtain:

$$\dot{\boldsymbol{\mu}} = \boldsymbol{\Phi}_2\boldsymbol{\mu} - \rho_o\frac{\mathbf{P}_2\boldsymbol{\mu}}{\|\mathbf{P}_2\boldsymbol{\mu}\|} + \mathbf{R}\tilde{\mathbf{d}} \tag{B.41}$$

To show global finite-time stability about $\boldsymbol{\mu} = \mathbf{0}$, consider the Lyapunov function candidate $V = \boldsymbol{\mu}^{\mathrm{T}}\mathbf{P}_2\boldsymbol{\mu} > 0$, which satisfies $V(0) = 0, V_{(\boldsymbol{\mu}\to\infty)} \to \infty$. Its time derivative is given by:

$$\dot{V} = \dot{\boldsymbol{\mu}}^{\top}\mathbf{P}_2\boldsymbol{\mu} + \boldsymbol{\mu}^{\top}\mathbf{P}_2\dot{\boldsymbol{\mu}} \tag{B.42}$$

Substitute for $\dot{\boldsymbol{\mu}}$ from Eqn. (B.41) to obtain:

$$\dot{V} = \left(\boldsymbol{\Phi}_2\boldsymbol{\mu} - \rho_o\frac{\mathbf{P}_2\boldsymbol{\mu}}{\|\mathbf{P}_2\boldsymbol{\mu}\|} + \mathbf{R}\tilde{\mathbf{d}}\right)^{\top}\mathbf{P}_2\boldsymbol{\mu} + \boldsymbol{\mu}^{\top}\mathbf{P}_2\left(\boldsymbol{\Phi}_2\boldsymbol{\mu} - \rho_o\frac{\mathbf{P}_2\boldsymbol{\mu}}{\|\mathbf{P}_2\boldsymbol{\mu}\|} + \mathbf{R}\tilde{\mathbf{d}}\right) \tag{B.43}$$

which upon simplification gives:

$$\dot{V} = \boldsymbol{\mu}^{\top}(\mathbf{P}_2\boldsymbol{\Phi}_2 + \boldsymbol{\Phi}_2^{\top}\mathbf{P}_2)\boldsymbol{\mu} - 2\rho_o\frac{\boldsymbol{\mu}^{\top}\mathbf{P}_2^2\boldsymbol{\mu}}{\|\mathbf{P}_2\boldsymbol{\mu}\|} + 2\boldsymbol{\mu}^{\top}\mathbf{P}_2\mathbf{R}\tilde{\mathbf{d}} \tag{B.44}$$

$$\dot{V} = -\boldsymbol{\mu}^{\top}\boldsymbol{\mu} - 2\rho_o\|\mathbf{P}_2\boldsymbol{\mu}\| + 2\boldsymbol{\mu}^{\top}\mathbf{P}_2\mathbf{R}\tilde{\mathbf{d}} \tag{B.45}$$

Equation (B.45) can be written as an inequality:

$$\dot{V} \leq -\|\boldsymbol{\mu}\|^2 - 2\rho_o\|\mathbf{P}_2\boldsymbol{\mu}\| + 2\|\mathbf{P}_2\boldsymbol{\mu}\|\,\|\mathbf{R}\tilde{\mathbf{d}}\| \tag{B.46}$$

$$\dot{V} \leq -2\|\mathbf{P}_2\boldsymbol{\mu}\|(\rho_o - \|\mathbf{R}\tilde{\mathbf{d}}\|) \tag{B.47}$$

If the outer loop sliding mode gain vector is set as $\boldsymbol{\rho}_o > \|\mathbf{R}\tilde{\mathbf{d}}\| + \gamma_o$ for some $\gamma_o > 0$ then $\dot{V} < 0$ is ensured except if $\boldsymbol{\mu} = \mathbf{0}$. For this choice of the sliding mode gain, global asymptotic stability about $\boldsymbol{\mu} = \mathbf{0}$ is ensured.

Remark: Eqn. (B.39) is valid only if the outer loop control command $\mathbf{r}_1$ is ideally tracked by the inner loop so that the inner loop output is identical to the outer loop control, i.e. $\mathbf{y}_1 = [\phi\ \theta]^\top = \mathbf{r}_1$. However, the inner loop will track the outer loop command signal $\mathbf{r}_1$ with some non-zero error and the two-loop stability in this case is discussed in the following section.

B.3 Two-Loop Coupled System Dynamics and Stability Analysis

The two-loop stability analysis follows the backstepping approach discussed in Ref. [40]. To account for imperfect outer loop command command tracking in the inner loop, $\dot{\boldsymbol{\mu}}$ must consider $\mathbf{y}_1 = \mathbf{r}_1 + \dot{\mathbf{x}}_{e1}$, where $\mathbf{y}_1 = [\phi\ \theta]^\top$, $\mathbf{r}_1 = [\phi\ \theta]^\top$, and $\dot{\mathbf{x}}_{e1} = [(\phi - \phi_c)\ (\theta - \theta_c)]^\top$. Thus, Eqn. (B.39) must be rewritten as:

$$\dot{\boldsymbol{\mu}} = \mathbf{R}\tilde{\mathbf{F}}\tilde{\mathbf{z}} + \mathbf{R}\tilde{\mathbf{G}}\mathbf{y}_1 - \mathbf{R}\tilde{\mathbf{T}}_o\mathbf{q} + \mathbf{R}\tilde{\mathbf{d}} - \mathbf{R}_3\dot{\mathbf{q}} \tag{B.48}$$

$\dot{\mathbf{x}}_{e1}$ can be written in terms of the transformed inner loop system coordinates as $\dot{\mathbf{x}}_{e1} = \mathbf{M}\mathbf{T}_r^{-1}\dot{\tilde{\mathbf{x}}}$, where $\mathbf{M} = [\mathbf{I}_2\ \mathbf{0}_{2\times10}]$ selects the states $(\phi - \phi_c)$ and $(\theta - \theta_c)$ from the original state vector. Recall from Eqn. (B.7) that the inner loop state transformation is $\tilde{\mathbf{x}} = \mathbf{T}_r^{-1}\bar{\mathbf{x}}$ where $\bar{\mathbf{x}} = [\mathbf{x}_e\ \mathbf{x}]^\top$ are the original inner loop system coordinates. Thus Eqn. (B.48) can be written as:

$$\dot{\boldsymbol{\mu}} = \mathbf{R}\tilde{\mathbf{F}}\tilde{\mathbf{z}} + \mathbf{R}\tilde{\mathbf{G}}\mathbf{r}_1 + \mathbf{R}\tilde{\mathbf{G}}\mathbf{M}\mathbf{T}_r^{-1}\dot{\tilde{\mathbf{x}}} - \mathbf{R}\tilde{\mathbf{T}}_o\mathbf{q} + \mathbf{R}\tilde{\mathbf{d}} - \mathbf{R}_3\dot{\mathbf{q}} \tag{B.49}$$

Inserting Eqn. (B.40) into Eqn. (B.49) gives:

$$\dot{\boldsymbol{\mu}} = \boldsymbol{\Phi}_2\boldsymbol{\mu} - \rho_o\frac{\mathbf{P}_2\boldsymbol{\mu}}{\|\mathbf{P}_2\boldsymbol{\mu}\|} + \mathbf{R}\tilde{\mathbf{d}} + \mathbf{R}\tilde{\mathbf{G}}\mathbf{M}\mathbf{T}_r^{-1}\dot{\tilde{\mathbf{x}}} \tag{B.50}$$

From Eqns. (B.30)–(B.31), the inner loop transformed system dynamics upon the sliding surface can be expressed as:

$$\begin{bmatrix}\dot{\mathbf{x}}_1\\ \dot{\mathbf{x}}_2\end{bmatrix} = \begin{bmatrix}(\tilde{\mathbf{A}}_{11}-\tilde{\mathbf{A}}_{12}\mathbf{S}_2^{-1}\mathbf{S}_1) & 0\\ -\mathbf{S}_2^{-1}\mathbf{S}_1(\tilde{\mathbf{A}}_{11}-\tilde{\mathbf{A}}_{12}\mathbf{S}_2^{-1}\mathbf{S}_1) & 0\end{bmatrix}\begin{bmatrix}\mathbf{x}_1\\ \mathbf{x}_2\end{bmatrix} \tag{B.51}$$

$$-\begin{bmatrix}\mathbf{T}_1\\ -\mathbf{S}_2^{-1}\mathbf{S}_1\mathbf{T}_1\end{bmatrix}\mathbf{r} \tag{B.52}$$

$$\text{In compact form: } \dot{\tilde{\mathbf{x}}} = \breve{\mathbf{A}}\tilde{\mathbf{x}} - \breve{\mathbf{T}}\mathbf{r} \tag{B.53}$$

Substituting Eqn. (B.53) in Eqn. (B.50) gives:

$$\dot{\boldsymbol{\mu}} = \boldsymbol{\Phi}_2\boldsymbol{\mu} - \rho_o\frac{\mathbf{P}_2\boldsymbol{\mu}}{\|\mathbf{P}_2\boldsymbol{\mu}\|} + \mathbf{R}\tilde{\mathbf{d}} + \mathbf{R}\tilde{\mathbf{G}}\mathbf{M}\mathbf{T}_r^{-1}\breve{\mathbf{A}}\tilde{\mathbf{x}} - \mathbf{R}\tilde{\mathbf{G}}\mathbf{M}\mathbf{T}_r^{-1}\breve{\mathbf{T}}\mathbf{r} \tag{B.54}$$

Also, using Eqn. (B.36) and $\dot{\mathbf{z}}_e = \mathbf{z} - \mathbf{q}$, one obtains:

$$\mathbf{z} = \mathbf{R}_2^{-1}(\boldsymbol{\mu} - \mathbf{R}_1\mathbf{z}_e + \mathbf{R}_3\mathbf{q}) \tag{B.55}$$

$$\dot{\mathbf{z}}_e = \mathbf{R}_2^{-1}\boldsymbol{\mu} - \mathbf{R}_2^{-1}\mathbf{R}_1\mathbf{z}_e + (\mathbf{R}_2^{-1}\mathbf{R}_3 - \mathbf{I})\mathbf{q} \tag{B.56}$$

B.3.1 Discontinuous Inner Loop, Continuous Outer Loop

The first analysis assumes that the inner loop dynamics are implemented by the discontinuous control as given in Eqn. (B.18), which ensures $\boldsymbol{\sigma} = 0$ in finite time given by Eqn. (B.28). Therefore, the two-loop dynamics can be represented by the outer loop tracking error $\mathbf{z}_e$, the outer loop sliding variable $\boldsymbol{\mu}$, and the inner loop augmented state vector $\tilde{\mathbf{x}}$.

If the outer loop control is implemented by a continuous control approximation of the form:

$$\mathbf{r}_1 = \begin{cases} -(\mathbf{R}\tilde{\mathbf{G}})^{-1}\left(\mathbf{R}\tilde{\mathbf{F}}\tilde{\mathbf{z}} - \boldsymbol{\Phi}_2\mathbf{R}\tilde{\mathbf{z}} + \boldsymbol{\Phi}_2\mathbf{R}_3\mathbf{q} - \mathbf{R}\tilde{\mathbf{T}}_o\mathbf{q} - \mathbf{R}_3\dot{\mathbf{q}} + \rho_o\frac{\mathbf{P}_2\boldsymbol{\mu}}{\epsilon_o}\right) & \ldots \text{if } \|\mathbf{P}_2\boldsymbol{\mu}\| \leqslant \epsilon_o \\ -(\mathbf{R}\tilde{\mathbf{G}})^{-1}\left(\mathbf{R}\tilde{\mathbf{F}}\tilde{\mathbf{z}} - \boldsymbol{\Phi}_2\mathbf{R}\tilde{\mathbf{z}} + \boldsymbol{\Phi}_2\mathbf{R}_3\mathbf{q} - \mathbf{R}\tilde{\mathbf{T}}_o\mathbf{q} - \mathbf{R}_3\dot{\mathbf{q}} + \rho_o\frac{\mathbf{P}_2\boldsymbol{\mu}}{\|\mathbf{P}_2\boldsymbol{\mu}\|}\right) & \ldots \text{if } \|\mathbf{P}_2\boldsymbol{\mu}\| > \epsilon_o \end{cases} \tag{B.57}$$

where the discontinuous unit vector has been replaced by a high-gain linear term inside a boundary layer of size ϵ_o, then the outer loop sliding dynamics are represented by:

$$\dot{\boldsymbol{\mu}} = \begin{cases} \left(\boldsymbol{\Phi}_2 - \rho_o\frac{\mathbf{P}_2}{\epsilon_o}\right)\boldsymbol{\mu} + \mathbf{R}\tilde{\mathbf{d}} + \mathbf{R}\tilde{\mathbf{G}}\mathbf{M}\mathbf{T}_r^{-1}\dot{\tilde{\mathbf{x}}} & \ldots \text{if } \|\mathbf{P}_2\boldsymbol{\mu}\| \leqslant \epsilon_o \\ \boldsymbol{\Phi}_2\boldsymbol{\mu} - \rho_o\frac{\mathbf{P}_2\boldsymbol{\mu}}{\|\mathbf{P}_2\boldsymbol{\mu}\|} + \mathbf{R}\tilde{\mathbf{d}} + \mathbf{R}\tilde{\mathbf{G}}\mathbf{M}\mathbf{T}_r^{-1}\dot{\tilde{\mathbf{x}}} & \ldots \text{if } \|\mathbf{P}_2\boldsymbol{\mu}\| > \epsilon_o \end{cases} \tag{B.58}$$

Substituting for $\dot{\tilde{\mathbf{x}}}$ from Eqn. (B.53) in Eqn. (B.58), we obtain::

$$\dot{\boldsymbol{\mu}} = \begin{cases} \left(\boldsymbol{\Phi}_2 - \rho_o\frac{\mathbf{P}_2}{\epsilon_o}\right)\boldsymbol{\mu} + \mathbf{R}\tilde{\mathbf{d}} + \mathbf{R}\tilde{\mathbf{G}}\mathbf{M}\mathbf{T}_r^{-1}\breve{\mathbf{A}}\tilde{\mathbf{x}} - \mathbf{R}\tilde{\mathbf{G}}\mathbf{M}\mathbf{T}_r^{-1}\breve{\mathbf{T}}\mathbf{r} & \ldots \text{if } \|\mathbf{P}_2\boldsymbol{\mu}\| \leqslant \epsilon_o \\ \boldsymbol{\Phi}_2\boldsymbol{\mu} - \rho_o\frac{\mathbf{P}_2\boldsymbol{\mu}}{\|\mathbf{P}_2\boldsymbol{\mu}\|} + \mathbf{R}\tilde{\mathbf{d}} + \mathbf{R}\tilde{\mathbf{G}}\mathbf{M}\mathbf{T}_r^{-1}\breve{\mathbf{A}}\tilde{\mathbf{x}} - \mathbf{R}\tilde{\mathbf{G}}\mathbf{M}\mathbf{T}_r^{-1}\breve{\mathbf{T}}\mathbf{r} & \ldots \text{if } \|\mathbf{P}_2\boldsymbol{\mu}\| > \epsilon_o \end{cases} \tag{B.59}$$

Notice that Eqns. (B.53), (B.59), and (B.56) represent the two-loop coupled system dynamics. Assuming that the outer loop sliding dynamics operates inside the boundary layer, i.e. for the case $\|\mathbf{P}_2\boldsymbol{\mu}\| \leqslant \epsilon_o$, the two-loop coupled system in state space form can be written as:

$$\begin{bmatrix} \dot{\mathbf{z}}_e \\ \dot{\boldsymbol{\mu}} \\ \dot{\tilde{\mathbf{x}}} \end{bmatrix} = \begin{bmatrix} -\mathbf{R}_2^{-1}\mathbf{R}_1 & \mathbf{R}_2^{-1} & 0 \\ 0 & \boldsymbol{\Phi}_2 - \rho_o\mathbf{P}_2/\epsilon_o & \mathbf{R}\tilde{\mathbf{G}}\mathbf{M}\mathbf{T}_r^{-1}\breve{\mathbf{A}} \\ 0 & 0 & \breve{\mathbf{A}} \end{bmatrix} \begin{bmatrix} \mathbf{z}_e \\ \boldsymbol{\mu} \\ \tilde{\mathbf{x}} \end{bmatrix} - \begin{bmatrix} 0 \\ \mathbf{R}\tilde{\mathbf{G}}\mathbf{M}\mathbf{T}_r^{-1}\breve{\mathbf{T}} \\ \breve{\mathbf{T}} \end{bmatrix}\mathbf{r} + \begin{bmatrix} \mathbf{R}_2^{-1}\mathbf{R}_3 - \mathbf{I} \\ 0 \\ 0 \end{bmatrix}\mathbf{q} + \begin{bmatrix} 0 \\ \mathbf{R}\tilde{\mathbf{d}} \\ 0 \end{bmatrix} \tag{B.60}$$

The two-loop coupled system dynamics Eqn. (B.60) has a globally asymptotically stable equilibrium about $\{\mathbf{z}_e, \boldsymbol{\mu}, \tilde{\mathbf{x}}\}^\top = \mathbf{0}$ if the eigenvalues of the system matrix are stable. Inserting the values of matrices $\mathbf{R}_1 = \mathrm{diag}(0.2, 0.2)$, $\mathbf{R}_2 = \mathbf{R}_3 = \mathbf{I}_2$, $\mathbf{G} \approx [-9.8\ 0;\ 0\ 9.8]$, $\mathbf{M} = [\mathbf{I}_2\ \mathbf{0}_{2\times 10}]$, $\boldsymbol{\Phi}_2 = -0.5\mathbf{I}_2$, which gives $\mathbf{P}_2 = \mathbf{I}_2$, $\boldsymbol{\rho}_o = 0.5$, $\epsilon_o = 0.2$, $\mathbf{T}_r$ from Eqn. (B.6), $\tilde{\mathbf{S}}, \mathbf{S}_1, \mathbf{S}_2$ from Eqn. (B.13), then the following eigenvalues are obtained: $[-0.2,\ -0.2,\ -3,\ -3,\ 0,\ 0,\ 0,\ 0,\ -4,\ -1.7550 + 1.5478i,\ -1.7550 - 1.5478i,\ -2.1012 + 1.0238i,\ -2.1012 - 1.0238i,\ -0.9500,\ -0.0085,\ -0.0239]$. The first four eigenvalues correspond to the states $\mathbf{z}_e$ and $\boldsymbol{\mu}$. The four zero eigenvalues are associated to the four $\mathbf{x}_2$ states, due to their linear algebraic relation to the states $\mathbf{x}_1$. The last eight eigenvalues are associated with the states $\mathbf{x}_1$, which also represent the desired closed-loop eigenvalues of the inner loop.

B.3.2 Continuous Inner Loop, Continuous Outer Loop

In contrast to Appendix Sec. B.3.1, the second analysis considers that the inner loop is also implemented by a continuous approximation of the discontinuous control. Thus, Eqn. (B.18) is modified to the following form:

$$\mathbf{u} = \begin{cases} -(\tilde{\mathbf{S}}\tilde{\mathbf{B}})^{-1}\Big((\tilde{\mathbf{S}}\tilde{\mathbf{A}} - \boldsymbol{\Phi}_1\tilde{\mathbf{S}})\tilde{\mathbf{x}} + \tilde{\mathbf{S}}\tilde{\mathbf{T}}\mathbf{r} - \boldsymbol{\rho}\,\frac{\mathbf{P}_1\boldsymbol{\sigma}}{\epsilon}\Big) & \ldots \text{if } \|\mathbf{P}_1\boldsymbol{\sigma}\| \leqslant \epsilon \\ -(\tilde{\mathbf{S}}\tilde{\mathbf{B}})^{-1}\Big((\tilde{\mathbf{S}}\tilde{\mathbf{A}} - \boldsymbol{\Phi}_1\tilde{\mathbf{S}})\tilde{\mathbf{x}} + \tilde{\mathbf{S}}\tilde{\mathbf{T}}\mathbf{r} - \boldsymbol{\rho}\,\frac{\mathbf{P}_1\boldsymbol{\sigma}}{\|\mathbf{P}_1\boldsymbol{\sigma}\|}\Big) & \ldots \text{if } \|\mathbf{P}_1\boldsymbol{\sigma}\| > \epsilon \end{cases} \qquad \text{(B.61)}$$

The inner loop sliding variable dynamics can be modified from Eqn. (B.19) to the following:

$$\dot{\boldsymbol{\sigma}} = \begin{cases} \boldsymbol{\Phi}_1\boldsymbol{\sigma} - \boldsymbol{\rho}\,\frac{\mathbf{P}_1\boldsymbol{\sigma}}{\epsilon} + \tilde{\mathbf{S}}\tilde{\mathbf{f}} & \ldots \text{if } \|\mathbf{P}_1\boldsymbol{\sigma}\| \leqslant \epsilon \\ \boldsymbol{\Phi}_1\boldsymbol{\sigma} - \boldsymbol{\rho}\,\frac{\mathbf{P}_1\boldsymbol{\sigma}}{\|\mathbf{P}_1\boldsymbol{\sigma}\|} + \tilde{\mathbf{S}}\tilde{\mathbf{f}} & \ldots \text{if } \|\mathbf{P}_1\boldsymbol{\sigma}\| > \epsilon \end{cases} \qquad \text{(B.62)}$$

For these inner loop sliding dynamics, the Lyapunov analysis of Eqn. (B.25) is modified to the following cases:

$$\dot{V} \leqslant \begin{cases} -2\|\mathbf{P}_1\boldsymbol{\sigma}\|(\boldsymbol{\rho}\|\mathbf{P}_1\boldsymbol{\sigma}\|/\epsilon - \|\mathbf{S}\tilde{\mathbf{f}}\|) & \text{if } \|\mathbf{P}_1\boldsymbol{\sigma}\| \leqslant \epsilon \\ -2\|\mathbf{P}_1\boldsymbol{\sigma}\|(\boldsymbol{\rho} - \|\mathbf{S}\tilde{\mathbf{f}}\|) & \text{if } \|\mathbf{P}_1\boldsymbol{\sigma}\| > \epsilon \end{cases} \tag{B.63}$$

Setting sliding mode gain greater than the uncertainty bound, inequalities (B.63) imply that $\boldsymbol{\sigma} < \epsilon$ in finite time, but $\boldsymbol{\sigma} \neq \mathbf{0}$. Therefore, using Eqn. (B.15), Eqn. (B.29) is modified to:

$$\boldsymbol{\sigma} = \mathbf{S}_1\mathbf{x}_1 + \mathbf{S}_2\mathbf{x}_2 \tag{B.64}$$

$$\mathbf{x}_2 = \mathbf{S}_2^{-1}\boldsymbol{\sigma} - \mathbf{S}_2^{-1}\mathbf{S}_1\mathbf{x}_1 \tag{B.65}$$

Then, inserting Eqn. (B.65) into Eqn. (B.8), Eqns. (B.30)–(B.31) are modified to include the effect of nonzero $\boldsymbol{\sigma}$ and we obtain:

$$\dot{\mathbf{x}}_1 = (\tilde{\mathbf{A}}_{11} - \tilde{\mathbf{A}}_{12}\mathbf{S}_2^{-1}\mathbf{S}_1)\mathbf{x}_1 + \tilde{\mathbf{A}}_{12}\mathbf{S}_2^{-1}\boldsymbol{\sigma} - \mathbf{T}_1\mathbf{r} \tag{B.66}$$

$$\dot{\mathbf{x}}_2 = \mathbf{S}_2^{-1}\dot{\boldsymbol{\sigma}} - \mathbf{S}_2^{-1}\mathbf{S}_1(\tilde{\mathbf{A}}_{11} - \tilde{\mathbf{A}}_{12}\mathbf{S}_2^{-1}\mathbf{S}_1)\mathbf{x}_1 - \mathbf{S}_2^{-1}\mathbf{S}_1\tilde{\mathbf{A}}_{12}\mathbf{S}_2^{-1}\boldsymbol{\sigma} + \mathbf{S}_2^{-1}\mathbf{S}_1\mathbf{T}_1\mathbf{r} \tag{B.67}$$

$$\begin{bmatrix} \dot{\mathbf{x}}_1 \\ \dot{\mathbf{x}}_2 \end{bmatrix} = \begin{bmatrix} (\tilde{\mathbf{A}}_{11} - \tilde{\mathbf{A}}_{12}\mathbf{S}_2^{-1}\mathbf{S}_1) & 0 \\ -\mathbf{S}_2^{-1}\mathbf{S}_1(\tilde{\mathbf{A}}_{11} - \tilde{\mathbf{A}}_{12}\mathbf{S}_2^{-1}\mathbf{S}_1) & 0 \end{bmatrix} \begin{bmatrix} \mathbf{x}_1 \\ \mathbf{x}_2 \end{bmatrix} + \begin{bmatrix} \tilde{\mathbf{A}}_{12}\mathbf{S}_2^{-1} \\ -\mathbf{S}_2^{-1}\mathbf{S}_1\tilde{\mathbf{A}}_{12}\mathbf{S}_2^{-1} \end{bmatrix}\boldsymbol{\sigma} - \begin{bmatrix} \mathbf{T}_1 \\ -\mathbf{S}_2^{-1}\mathbf{S}_1\mathbf{T}_1 \end{bmatrix}\mathbf{r} + \begin{bmatrix} \mathbf{0} \\ \mathbf{S}_2^{-1} \end{bmatrix}\dot{\boldsymbol{\sigma}} \tag{B.68}$$

$$\text{In compact form: } \dot{\tilde{\mathbf{x}}} = \breve{\mathbf{A}}\tilde{\mathbf{x}} + \breve{\mathbf{D}}\boldsymbol{\sigma} - \breve{\mathbf{T}}\mathbf{r} + \breve{\mathbf{S}}\dot{\boldsymbol{\sigma}} \tag{B.69}$$

$$\text{Using Eqn. (B.16): } \dot{\tilde{\mathbf{x}}} = \breve{\mathbf{A}}\tilde{\mathbf{x}} + \breve{\mathbf{D}}\boldsymbol{\sigma} - \breve{\mathbf{T}}\mathbf{r} + \breve{\mathbf{S}}\tilde{\mathbf{S}}\dot{\tilde{\mathbf{x}}} \tag{B.70}$$

$$\text{which gives: } \dot{\tilde{\mathbf{x}}} = (\mathbf{I} - \breve{\mathbf{S}}\tilde{\mathbf{S}})^{-1}(\breve{\mathbf{A}}\tilde{\mathbf{x}} + \breve{\mathbf{D}}\boldsymbol{\sigma} - \breve{\mathbf{T}}\mathbf{r}) \tag{B.71}$$

The modified inner loop system dynamics given in Eqn. (B.53) have an influence on the outer loop sliding dynamics through Eqn. (B.50). Thus, the outer loop sliding dynamics (inside the boundary layer) can be written from Eqn. (B.50) as:

$$\begin{aligned}\dot{\boldsymbol{\mu}} &= \left(\boldsymbol{\Phi}_2 - \rho_o\frac{\mathbf{P}_2}{\epsilon_o}\right)\boldsymbol{\mu} + \mathbf{R}\tilde{\mathbf{d}} + \mathbf{R}\tilde{\mathbf{G}}\mathbf{M}\mathbf{T}_r^{-1}(\mathbf{I}-\breve{\mathbf{S}}\tilde{\mathbf{S}})^{-1}\breve{\mathbf{A}}\tilde{\mathbf{x}} \\ &\quad + \mathbf{R}\tilde{\mathbf{G}}\mathbf{M}\mathbf{T}_r^{-1}(\mathbf{I}-\breve{\mathbf{S}}\tilde{\mathbf{S}})^{-1}\breve{\mathbf{D}}\boldsymbol{\sigma} - \mathbf{R}\tilde{\mathbf{G}}\mathbf{M}\mathbf{T}_r^{-1}(\mathbf{I}-\breve{\mathbf{S}}\tilde{\mathbf{S}})^{-1}\breve{\mathbf{T}}\mathbf{r} \qquad \text{(B.72)}\end{aligned}$$

Thus, the two loop system dynamics of Eqn. (B.60) must be extended to include the inner loop sliding variable $\boldsymbol{\sigma}$. The two-loop dynamics are obtained as:

$$\begin{bmatrix}\dot{\mathbf{z}}_e \\ \dot{\boldsymbol{\mu}} \\ \dot{\tilde{\mathbf{x}}} \\ \dot{\boldsymbol{\sigma}}\end{bmatrix} = \begin{bmatrix} -\mathbf{R}_2^{-1}\mathbf{R}_1 & \mathbf{R}_2^{-1} & 0 & 0 \\ 0 & \boldsymbol{\Phi}_2 - \rho_o\mathbf{P}_2/\epsilon_o & \mathbf{R}\tilde{\mathbf{G}}\mathbf{M}\mathbf{T}_r^{-1}(\mathbf{I}-\breve{\mathbf{S}}\tilde{\mathbf{S}})^{-1}\breve{\mathbf{A}} & \mathbf{R}\tilde{\mathbf{G}}\mathbf{M}\mathbf{T}_r^{-1}(\mathbf{I}-\breve{\mathbf{S}}\tilde{\mathbf{S}})^{-1}\breve{\mathbf{D}} \\ 0 & 0 & (\mathbf{I}-\breve{\mathbf{S}}\tilde{\mathbf{S}})^{-1}\breve{\mathbf{A}} & (\mathbf{I}-\breve{\mathbf{S}}\tilde{\mathbf{S}})^{-1}\breve{\mathbf{D}} \\ 0 & 0 & 0 & \boldsymbol{\Phi}_1 - \boldsymbol{\rho}\mathbf{P}_1/\epsilon \end{bmatrix}\begin{bmatrix}\mathbf{z}_e \\ \boldsymbol{\mu} \\ \tilde{\mathbf{x}} \\ \boldsymbol{\sigma}\end{bmatrix}$$

$$- \begin{bmatrix} 0 \\ \mathbf{R}\tilde{\mathbf{G}}\mathbf{M}\mathbf{T}_r^{-1}(\mathbf{I}-\breve{\mathbf{S}}\tilde{\mathbf{S}})^{-1}\breve{\mathbf{T}} \\ (\mathbf{I}-\breve{\mathbf{S}}\tilde{\mathbf{S}})^{-1}\breve{\mathbf{T}} \\ 0 \end{bmatrix}\mathbf{r} + \begin{bmatrix}\mathbf{R}_2^{-1}\mathbf{R}_3 - \mathbf{I} \\ 0 \\ 0 \\ 0\end{bmatrix}\mathbf{q} + \begin{bmatrix} 0 \\ \mathbf{R}\tilde{\mathbf{d}} \\ 0 \\ \tilde{\mathbf{S}}\tilde{\mathbf{f}}\end{bmatrix} \qquad \text{(B.73)}$$

The two-loop coupled system dynamics Eqn. (B.73) has a globally asymptotically stable equilibrium about $\{\mathbf{z}_e, \boldsymbol{\mu}, \tilde{\mathbf{x}}, \boldsymbol{\sigma}\}^\top = \mathbf{0}$ if the eigenvalues of the system matrix are stable. In addition to the previously defined values, inserting $\mathbf{P}_1 = \mathbf{I}_2$, $\boldsymbol{\rho} = 0.5$, $\epsilon = 0.2$ into the two-loop coupled system matrix, the following eigenvalues are obtained: $[-0.2,\ -0.2,\ -3,\ -3,\ 0,\ 0,\ 0,\ 0,\ -4,\ -1.7550 + 1.5478i,\ -1.7550 - 1.5478i,\ -2.1012 + 1.0238i,\ -2.1012 - 1.0238i,\ -0.9500,\ -0.0085,\ -0.0239,\ -3,\ -3,\ -3,\ -3]$. The four additional stable eigenvalues are associated with the inner loop sliding variable $\boldsymbol{\sigma}$. Thus, it can be seen that despite the continuous control laws both in the inner and outer loop, the overall two-loop coupled dynamics is rendered globally asymptotically stable.

This page intentionally left blank.

C Author Biography

Omkar Halbe was born in Mumbai on May 19, 1986. He completed his primary and secondary education at Swami Vivekanand High School, Chembur, Mumbai in 2004. He credits his parents and school teachers for nurturing an early interest in physics and mathematics. In 2004, he joined the Bachelor of Technology program in electronics engineering at the Veermata Jijabai Technological Institute (formerly Victoria Jubilee Technical Institute) and obtained his degree in 2008. Aside from the regular curriculum during his bachelor's program, he pursued industry internships that gave him a first-hand experience in automation and control, and also helped him decide on his future course of studies. He was also awarded the JN Tata Scholarship for undergraduate academic excellence in the year 2004-2005.

He then joined the master of engineering program at Cornell University, where he took advanced courses in systems engineering, optimization, feedback control, and robotics. His master's project was an interdisciplinary one aimed at improving the fuel efficiency of truck-trailer refrigeration units. Applying multidisciplinary optimization in an industrial setting, the team was able to model, quantify and validate significant thermal benefits using minimal and low-cost technical improvements. For this work, the team was awarded the best master's project and poster presentation award at the Cornell Engineering Research Conference, 2009. Besides this, Omkar was also awarded the Cornell-Heidelberg Exchange Fellowship in the Spring of 2009.

Subsequently, he joined the Indian Institute of Science, Bangalore as project staff on reentry guidance and control for a reusable launch vehicle technology demonstrator. Here, he worked on new and computationally efficient guidance laws and coupled them to an adaptive flight control scheme to demonstrate robust and autonomous atmospheric reentry of an unpowered, winged launch vehicle until its designated recovery point on earth. The results of this work were presented at premier aerospace conferences and published in archival journals.

Following a brief stint at Eaton Corp as automotive powertrain controls engineer, he joined Airbus Group in 2011. Between 2011 and 2012, he worked with Airbus Defence and Space (formerly EADS Cassidian) in Elancourt, France as systems engineer for command, control, and surveillance for land and maritime security. In 2013, he moved to Airbus Helicopters (formerly Eurocopter) in Donauwörth, Germany, where he got fascinated by helicopters and VTOL aircraft. He worked as avionics systems engineer for the development of cockpit-integrated digital moving map with navigation, traffic, and terrain/obstacle collision overlays in the HELIONIX suite. This function was eventually certified on all Airbus helicopter platforms. In 2017, he moved to industrial research and technology, working in rotorcraft air traffic management (ATM) as part of the Single European Sky ATM Research (SESAR) program. He led the flight testing activities at Airbus Helicopters for demonstrating and validating navigation and human performance during very steep and curved helicopter approach procedures, with the aim of increasing safety and improving all-weather access. He is currently involved in research and technology projects for future rotorcraft, namely enhanced perception, situation awareness, sensors, and computing for greater piloting autonomy.